A Study on Acoustic Impedance Microscopy for Biological and Medical Applications

(生物·医療応用のための音響インピーダンス顕微鏡に関する研究)

July, 2015

DOCTOR OF ENGINEERING

AGUS INDRA GUNAWAN

TOYOHASHI UNIVERSITY OF TECHNOLOGY

平成 27 年 7 月 8 日

Department Electrical and Electronic Information Eng. 学専攻	Student ID Number 学籍番号	第 129202 号	Supervisors 指導教員	Naohiro Hozumi Yoji Sakurai Masayuki Nagao
Applicant's name 氏名	Agus Indra Gunawan			

Abstract

論文内容の要旨　(博士)

Title of Thesis 博士学位論文名	A Study on Acoustic Impedance Microscopy for Biological and Medical Applications (生物·医療応用のための音響インピーダンス顕微鏡に関する研究)

(Approx. 800 words)

(要旨　1,200 字程度)

This study deals with a new type of biological acoustic microscopy to indicate acoustic impedance of biological soft tissues and cells. The system is a scanning acoustic microscope (SAM) that can obtain two-dimensional (2D) image of acoustic property by scanning the region of interest.

Acoustic impedance microscopy has been proposed since several years ago. A soft biological tissue is placed on a polymer substrate and an ultrasound beam in the frequency range of 30 - 100 MHz focused onto the interface is transmitted through the substrate. The reflection intensity is normalized by that from the reference material placed in the same condition as the target and interpreted into the cross-sectional characteristic acoustic impedance of the target. Mechanical scan with a microscale precision makes it possible to produce 2D acoustic impedance image. This research is mainly aimed to realize a precise calibration for interpreting the response signal into the absolute value of acoustic impedance.

In the conventional observation system, an acoustic transducer with a small angle of focusing was employed. In such a case, all beam components could be assumed to be perpendicular to the interface (vertical incidence) when the reflection was interpreted into acoustic impedance. The interpretation used to be done by considering simple simultaneous equations. However, as the beam was poorly focused, the spatial resolution (in the lateral direction) was not sufficient.

Herewith, we proposed improvement method for the conventional system. A transducer with a large focus angle of focusing (22° in half aperture angle) was used instead of the previous transducer. Fourier analysis was employed to analyze and decompose the beam components. Acoustic intensity was calculated by considering sound field distribution. Based on this calculation, we establish a

calibration curve, which precisely converts acoustic intensity into acoustic impedance. To verify the calibration curve, saline solutions with several contents of which acoustic impedance were known were observed by the same system. The measurement results were then plotted on the same chart as the analytical result. There was a good agreement between calculation and measurement results. As an experimental work, we observe cerebellar tissue of a rat. The layers of the cerebellar tissue were clearly observed with the absolute value of characteristic acoustic impedance which can be correlated with the elastic property.

In the second part of the study, we tried to access a cultured cell. Several adjustment and analysis were done, because some stuff in the previous system were no longer compatible. Since the target was much smaller than tissue scale, a sapphire lens transducer with a frequency range spreading from 200-400 MHz was used. A new calibration curve for cell size observation was established by considering all acoustic propagation in the lens, coupling medium and substrate. The measurements of several saline solutions were performed for verification. A good agreement was seen between calculation and measurement results. As an experimental work, we observed cultured glia and investigated the difference in the effect of anticancer drug onto glia and glioma cells.

In the third part of the study, utilizing the above system, we tried to access the internal structure of a cultured cell. It was realized by focusing the acoustic beam onto the cell and receive the reflection from the substrate placed behind the cell. As an experimental work, we observed cultured glia and glioma cells. We compared the observation results of cell in terms of acoustic impedance and internal structure.   It was shown that this mode of observation can see internal structure of the cell including the nucleus. Whereas the acoustic impedance mode can mainly see the cross-sectional (interfacial) property of the target. In addition, we also investigate the structure of smeared hepatoma cells.

Through these three parts of this study, two advantages have been clarified. Observation can be finished in a very short time because this observation may skip staining process, which is usually required in the case of optical observation. Since the observation can be performed introducing no contaminant and invasion to the biological system, it is highly advantageous for medical and biological applications.

Contents

List of Figures

x

List of Tables

Chapter 1

Introduction

Chapter 1 will review the background of this research, especially for biological and medical application. Based on the clinical need, we need to explore the possibilities of this technique to discriminate healthy and tumorous tissue. Several techniques to detect tumorous tissue were compared. The history of ultrasound was also provided in this chapter. At the end of this chapter, motivation and research objective, contribution and thesis organization are described.

1.1   Background

There are applications of ultrasound in many fields. In Japan, researchers began to explore capabilities of ultrasound for medical diagnostic. In the particular case of biological microscopy, in 1991 Saijo *et al.* has successfully developed transmission and reflection mode of scanning acoustic microscope [12]. Because of its simplicity, reflection mode is followed by researchers up to now. Based on this technique, acoustic intensity, speed of sound, attenuation and thickness of target might be measured. By improving this technique, viscous-elastic properties of biological target can be obtained, gives a chance to distinguish healthy and cancerous cells.

By definition, cancer is an uncontrolled cell that is growing in a part of human body. Since it is an abnormal cell, cancer alters a healthy organ becoming a dysfunction organ. This behavior can be categorized as a disease. However, not all cancers are lethal diseases. It depends on which part the cancer is growing up in the human body. If cancer strikes the essential element of the body, it is getting more lethal of cancer type.

Since several decades ago, cancer was raising up for the cause of human death. Based on the report [1] as shown in Fig. 1.1, it was estimated that there were about 12.7 million new cancer cases and 7.6 million cancer deaths in 2008 worldwide. This number is predicted to increase up to 50% in 2020 by International Agency for Research on Cancer - World Health Organization (IARC - WHO). Cancer could attack men and women. Several types of cancer such as lung cancer, prostate cancer usually strike men, and for a woman the highest rate is breast cancer and the second was lung cancer.

There are several ways to prevent from cancer attacking. Key risk factors for cancer that can be avoided [13] are:

    a. tobacco use - responsible for 1.8 million cancer deaths per year (60% of these deaths occur in low- and
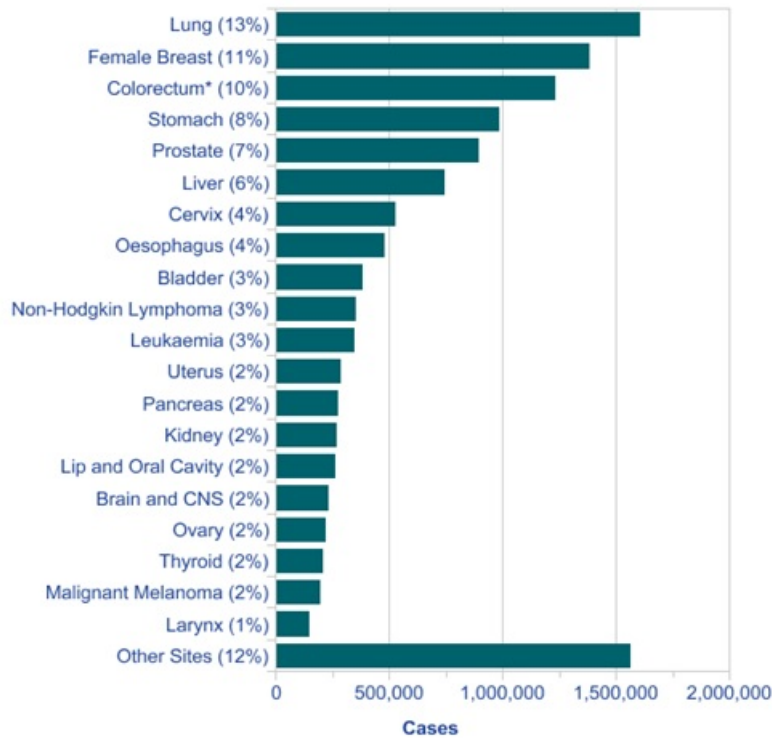
Figure 1.1: The 20 most commonly diagnosed cancers: 2008 estimates. [1]

middle-income countries);

b. being overweight, obese or physically inactive - together responsible for 274 000 cancer deaths per year;

c. harmful alcohol use - responsible for 351 000 cancer deaths per year;

d. sexually transmitted human papillomavirus (HPV) infection - responsible for 235 000 cancer deaths per year; and,

e. occupational carcinogens - responsible for at least 152 000 cancer deaths per year.

Even though the cancer looks deadly, cancer can be cured. Earlier detection can give a chance for successfully treatment. Several diagnostic tests for cancer are available in the market.

a. X-ray is one of radioactive wave, which it can be used to portray the human body. The ray needs high energy to be able to show part of the body, such as crack of bone, lung, breast, liver, etc. By having these advantages, the x-ray can be used to detect cancer. Several methods such as mammography, CT-scan, etc. use x-ray technology for cancer detection.

b. Computerized Tomography (CT-scan) or Computerized Axial Tomography (CAT-scan) can detect the existence of cancer inside the human body using x-ray technology. This technology took several scanning from different angels, give several cross-section pictures of the body being observed. Using this method, part of cancer, position and size of cancer can be detected more precise than using standard x-ray screening and give a clearer image.[14]

c. Another technique to detect cancer existence is so called Magnetic Resonance Imaging (MRI) diagnostic. This technique uses electromagnetic wave to identify the suspicious part of the body. MRI mechanism is different to the CT-scan. By single scanning, several slice of pictures can be generated from many different angels. MRI has several advantages compared to that CT-scan since it is not exposure to the x-ray radiation and gives a more accurate result.[14]

d. A relative new technology namely PET (Positron Emission Tomography) has a difference from MRI and CT. PET can show how organs work, how tissues are working as they look like not just an image. In addition, it can find out the stage of a cancer, to detect whether an organ is cancer or not, to detect the spreading of cancer to another part of body, to decide the best treatment for your cancer, and even to show how well cancer drug treatment is working. That is why, PET scanners are very expensive.[14]

Those technologies are used for detecting the existence of cancer. If cancer exists inside the body, the next step is the treatment. Either therapy or even cancer should be removed up by performing surgery can be used for cancer treatment. In the case of surgery, the surgeon dissects the body of the patient, remove the suspicious area of cancer. During or before finishing the surgery, the surgeon wants to make sure whether there is no cancer cell remain in the body of the patient. For this purpose, rapid cell observation is needed as surgeon wants to finish surgery as soon as possible.

Several techniques can be used to observe cancerous cell. PET as a superior measurement tool can perform observation. However, they need to inject tracer drug inside the body and to wait for an hour to ensure the body of the patient has already absorbed the tracer drug. Furthermore, it is very difficult to bring the patient who was dissected to have a screening under PET observation. Also, PET observation is very expensive. Another observation tool for cell observation is an optical microscope. The 2-dimensional image will be provided with excellent resolution as a result of observation. Patient tissue was taken and placed in a certain space for chemical fixation (staining). However, the staining process needs one to several hours before observation is being taken. It's mean it is too long to finish observation.

In this research, we proposed acoustic impedance microscope to observe biological tissue and cell structure. This technique needs only one up to several minutes to finish observation. Tissue may be placed on the substrate and observed under the microscope. As the result, 2-dimensional image will be provided.

Image resolution from acoustic microscope is still lower than the result from optical microscope. However, acoustic microscope may generate clear image which is sufficient for surgeon to make an observation by using high frequency of ultrasound [4, 15].

1.2 State of The Art

A mechanical collision generates particle vibrations inside corresponding material. The vibration will generate longitudinal wave. When the vibration of particles moves along the medium (i.e., air) and is detected by human, thus it is called as audible sound. Normal people can detect the frequency of the sound in between 20 – 20 kHz. The sound that is generated above the human hearing range is called ultrasound (ultrasonic). Even though ultrasound has a higher frequency than audible sound, they are not separated in term of its physical properties. Figure 1.2 shows sound spectrum and its application.
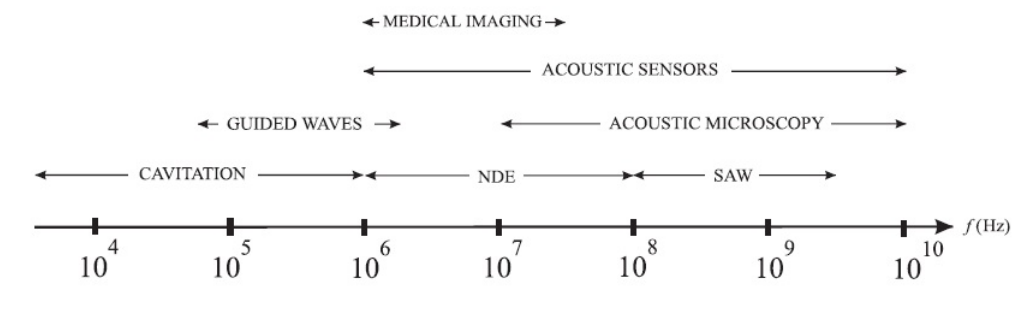
Figure 1.2: Frequency ranges for various ultrasonic applications. [2]

1.2.1 History of Ultrasound

At the beginning, this technology is used for submarine needs. Since the human has a limitation to watch and to determine the distance from the obstacle underneath the sea, they need an ultrasonic aid to overcome the limitation. A radar system is built based on ultrasonic technique to detect the existence of obstacle or creature in front of ship. In its development, this technology is used as a means of detecting the enemy's submarine ship in the First World War (WW1). In 1916 and 1917, Paul Langevin and Chilowsky filed two US patents disclosing the first ultrasonic submarine detector using an electrostatic method (singing condenser) and thin quartz crystals [16]. The amount of time taken by the signal to travel to the enemy submarine and echo back to the ship on which the device was mounted, was used to calculate the distance under water. There is a question, why visible light was not used to detect an obstacle in front of the ship. Both of visible light and sound are waves. However, several differences are presence on both waves.

One of the advantages of ultrasonic is it can penetrate well to opaque materials, where visible light radiation cannot penetrate it. In addition, slow speed gives a possibility to record the echo signal for further analyzing.

In addition to underwater application, ultrasound can be applied in several fields related to human daily life. It was started by measurement of speed of sound in the air, which is measured first time by Marin

4

Note	Optic wave	Acoustic wave
Type	Electromagnetic wave	Mechanical wave
Polarization	Can be polarized	Can not be polarized
Medium	No needs	Needs
Speed (air)	Very high and tent to constant	Low and change dependent on medium
Transmission mode	Transversal	Longitudinal
Transmitting medium	The denser the medium, the slower the speed	The denser the medium, the greater the speed

Table 1.1: The difference between optic and acoustic wave.

Mersenne utilizing reflection wave (echo-pulse) in 1640. Utilizing existing technology at that time, the determination of speed of sound exhibited that the error was under 10% [17]. Experiment regarding the speed of sound then was improved and continued by others researchers. In 1660, Robert Boyle did the measurement with a different way. The mathematic scientist Isaac Newton invented and stated that sound as a pressure wave transmitted through neighboring medium particles. The development of mathematic science is helpful to support sound observation until 19th century, when Georg Simon applied harmonic analysis that is developed by Joseph Fourier.

Ahead of the Second World War, von Pohlmann *et al.*, introduced the use of ultrasound therapy [18]. Gohr and Wedekin performed diagnostic of ultrasonography; however he only got a little success, in 1940 [19]. Then Dussik did first attempts to use ultrasound transmission in medical diagnostics ("hyper phonography" of the cerebral ventricles). It was conducted in 1942 [20], which was then followed by a diagnosis associated with a disease that attacks the brain in 1948 [21]. In 1942, other researcher, namely Firestone also developed ultrasound application for flaw detection [22] which used reflection mode (pulse echo) [23–25]. Measuring the pulse-echo technology had also been used in submarine ship radar to detect the position of the enemy during the Second World War (WW2). In 1949 Ludwig and Struthers developed a study using echo pulse principle to detect gallstone [26].

The existence of tissue at the interface between two different medium could be detected by ultrasound echo [27, 28] and suspicious cancerous cell also could be distinguished from benign cell on 1950 [29]. In around 1955, the echo pulse technique was displayed as A-Mode and B-Mode measurement [30–33].

For C-Mode, measurement was done by Erdene *et al.* on 1962 [34]. Tissue characterization had been successfully observed using A-mode technique by Schente *et al.* on 1964 [35]. Then for scanning mode on the application of ultrasound was performed by Thurstone *et al.* [36].

1.2.2 Ultrasound Application

Utilizing its advantages, researchers developed ultrasonic application into several field, such as industrial, concrete, food industry, oceanography, medical and biological needs.

In industrial application, ultrasound is used to detect hidden crack, porosity, discontinuity in metal and other composite materials. For this purpose, ultrasound in the range of frequency spreading from 500k – 10MHz is used to detect the flaws [37]. Using the similar technique *i.e.,* the echo pulse observation, cracking, voids and defects in concrete can be detected [38]. Furthermore, newer technique developed by Irie *et al.*, can be used to estimate the amount of corrosion of steel reinforcing bars inside concrete [39]. Ultrasound application in food industry can be applied in food processing, food preservation and extraction. Several processes such as freezing, cutting, drying, tempering, bleaching, sterilization and extraction have been applied efficiently in the food industry. The advantages of using ultrasound for food industry, includes: more efficient mixing and micromixing, faster energy and mass transfer, reduced thermal and concentration gradients, reduced temperature, selective extraction, reduced equipment size, faster response to process extraction control, faster start-up, increased production, and elimination of process steps [40]. This manuscript will describe ultrasound applications for biological and medical (biomedical) needs, especially for ultrasound microscopy application.

1.2.3 Ultrasound for Biomedical Microscopy

Nowadays, there are many ultrasound applications for biomedical need, such as abdominal, cardiac, maternity, gynecological, urological and vascular examination. It is also used for breast examination and tissue observation. In some cases, ultrasound is also used in medical therapy.

Introduction of Scanning Acoustic Microscope (SAM) took place in Stanford at early 1960, when transducer was designed and fabricated to operate in gigahertz of frequency. In the middle of 1950 H. Bommel and K. Dransfeld was able to use deposited piezoelectric films to generate sound microwave. Thus, this is followed by constructing of SAM in the early 1970 [41]. C. Quate and R. Lemons had successfully developed SAM at Stanford University in 1974, using focused ultrasound beam formed by acoustic lens [42] as shown in Fig. 1.3. On that time they used transmission mode of SAM. This mode subsequently was used by several researchers [43–46] until 1988. Due to its technical difficulties, this mode was abandoned.

The other is reflection mode of SAM. In 1991, Saijo *et al.* developed focused SAM, which was able to work in two modes, transmission and reflection mode. The attenuation and speed of sound inside gastric cancer were measured using reflection mode [12] as shown in Fig 1.4 (a). Utilizing the similar system, Saijo *et al.* measured attenuation and speed of sound inside infarcted myocardium [47]. Such kind of system is also developed by other researchers [48–55].
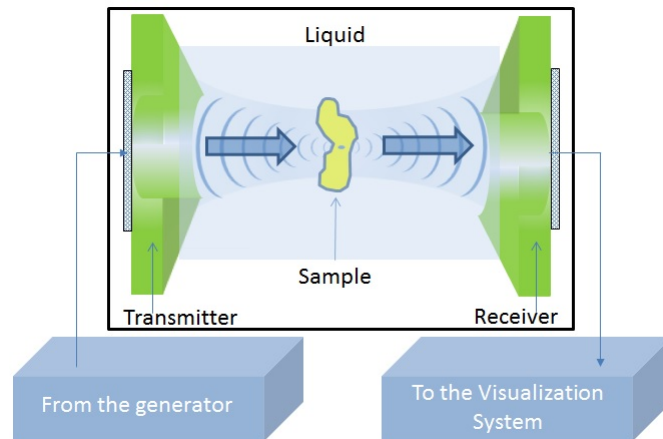
Figure 1.3: Transmission mode of Scanning Acoustic Microscope developed by C. Quate and R. Lemons
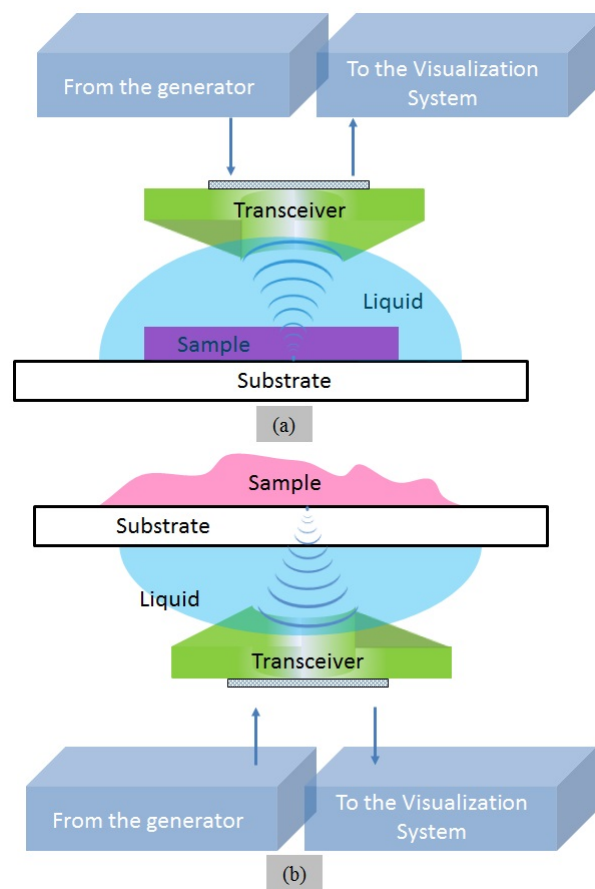
Figure 1.4: Reflection mode of Scanning Acoustic Microscope

7

1.3   Motivation and Research Objective

Most of the system created in the previous section integrate target, transducer and coupling medium into one. Such kind of structure may introduce contaminants to the target since they were gathered into one. Furthermore, coupling medium is not always chosen from the pure water and transducer is not always clean.

In order to obtain free of contaminant, Hozumi *et al.* proposed a new structure of reflection mode of SAM [56]. The target was placed onto sterilized substrate, which is used to separate the target from transducer and coupling medium as shown in Fig. 1.4 (b). A small angle of focused transducer was utilized, and acoustic impedance was calculated by assuming acoustic incident component was perpendicular to the target [56–58]. The result could observe the structure of the target. However, the spatial resolution is too low. An improvement calculation so called geometric-optic was conducted by including oblique incident [3]. However, frequency dependency was not considered in this calculation.

It is shown by the theory of Fourier optics that a focused beam is composed of plane waves with different propagation angles. Pulse wave that is used in the system generates many different frequency components. Based on the drawbacks of the system above, we are motivated to improve both spatial resolution and the accuracy of the calculation.

In actual measurement, large angle of focused transducer is usually used. Therefore, vertical incidence calculation may generate error to interpret acoustic impedance from acoustic intensity. To solve this problem, we proposed a new technique to obtain acoustic impedance microscopy. Oblique incidence that mostly yielded by the shape of the transducer is considered in the calculation. Fourier analysis is also used since the system consists of several frequency components. In this measurement, we also considering all aspects of the system, especially medium properties, because the ultrasound is propagated in multilayer medium. For this purpose, we have successfully calculated acoustic impedance as shown in our previous work [15].

1.4   Thesis Contributions

This thesis contributes to the field of acoustic microscope especially for biological and medical applications. Three different structures of acoustic microscope were presented here. Each structure gives its contribution as described below.

Acoustic impedance microscope for tissue observation:

a.   Fast observation, because it can skip staining and slicing process.

b.   Contaminant free.

c.   Improvement of resolution and accuracy of calculation has been achieved.

d. Calibration curve was successfully established and well verified by saline solutions measurement.

e. Cerebellar tissue of rat was successfully interpreted into acoustic impedance profile.

Acoustic impedance microscope for cell observation:

a. We have successfully improved tissue observation system for cell observation.

b. Calibration curve was established by Fourier analysis.

c. Contaminant free.

d. The motility process of Glia was successfully described.

e. This technique is able to distinguish cancerous and healthy cell.

f. The effect of drug also can be monitored by this system.

Internal structure of cell measurement:

a. We have successfully improved the structure of acoustic impedance observation for accessing internal structure of cell.

b. Nucleus of cell is clearly seen.

c. This technique is able to distinguish cancerous and healthy cell.

1.5   Thesis Organization

This thesis is organized into seven chapters as follows:

Chapter One describes the general introduction and the state of the art of this thesis.

Chapter Two describes the theoretical preparation for this study, consisting of fundamental theory general introduction and parameters used in this study.

Chapter Three describe the system setup for acoustic microscope. The flow of work and essential components are described in more detail.

Chapter Four describes scanning acoustic microscope for tissue observation. In this study, cerebellar tissue of rat is used as a specimen. Frequency of the transducer has a range of $30 - 100$ MHz, with the half angle of focusing is 22°. Calibration curves were developed base on vertical incidence calculation

and Fourier analysis. The calculation result is then verified by several saline solution measurements. As a practical measurement, cerebellar tissue of rat was observed and shown in acoustic impedance as 2D image.

Chapter Five describes numerical analysis of acoustic impedance microscope using lens transducer. This study is focused for cell observation. Frequency of the transducer has a range of 200 – 400 MHz, with the half angle of focusing is 60°. Calibration curve was developed by Fourier analysis. The curve is then verified by several saline solution measurements. As a practical measurement, cultured glia is shown in the motility process. This technique is also used to study the effect of drug for co-cultured Glia and Glioma.

Chapter Six describes the extended function of chapter five. Utilizing the same system as shown in chapter five, we need to modify the target in order to access internal structure of cell. Acoustic impedance measurement was compared to the internal structure measurement. As the result, internal structure measurement gives clearer observation than acoustic impedance measurement.

Chapter Seven describes the conclusion drawn from these studies, possibility for future study and applications. For future applications, we exhibit skin measurement, monitoring of cell differentiation and possibility to support one process of iPSCs development.

Chapter 2

Theoretical Preparation

In this chapter we will review literature corresponds to the technique or methodology applied in this thesis. At the beginning we review basic concept, especially for wave generation and wave propagation. The existence of discontinuous medium will be discussed in more detail, since we use multilayer medium in the system. The last part, sound potential, acoustic impedance, attenuation and resolution produced by transducer are also provided.

2.1 Wave Generation

When a homogeneous solid rod or beam is given by pressure disturbance, a deformation occurs on the solid rod body. Let's us consider the pressure has given only in one axis direction as shown in Fig. 2.1. A free solid beam with a particular density has a length of L. If a force F is applied to the beam's cross sectional of A to the right direction, then additional length of $\triangle$L deforms from initial length of L. The particle density become sparser. However, if F is applied in the opposite direction, the length become shorter by $\triangle$L. Consequently, the particle density became denser than the normal density.
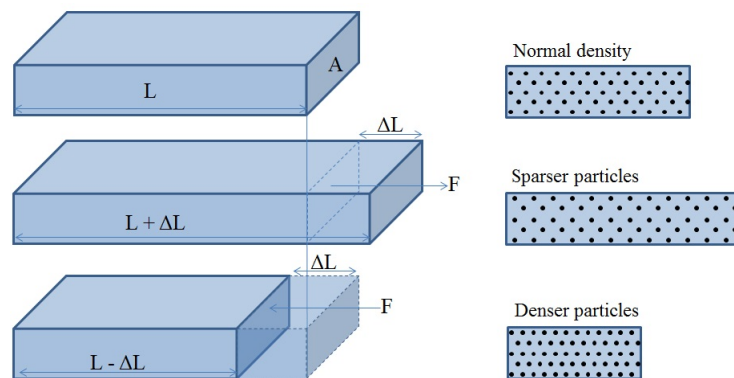
Figure 2.1: Pressure disturbance on a solid beam in one axis direction.

If the disturbance moves periodically and continuously, then the particle density will make a density profile "sparser-normal-denser- normal and so on" inside the solid beam. This oscillating profile may depicted as a wave. The simplest form of a wave is described the figure below.
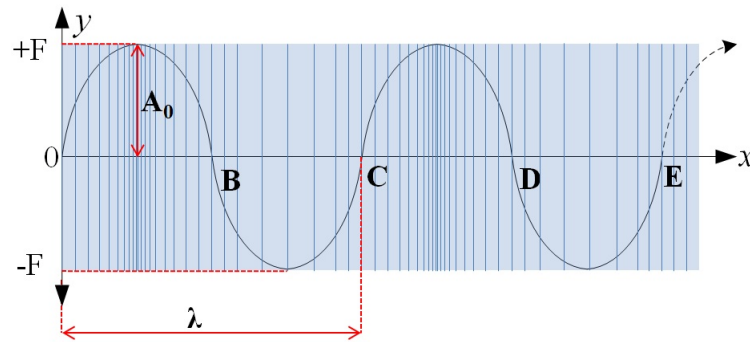
Figure 2.2: Fundamental Wave

Figure 2.2 shows the oscillation of the particle density. The densest is produced by +F, then the particle density gently and gradually sparser until the sparsest is obtained at -F. One full wave occurs if an oscillation from a certain position move until it backs to the previous position. If the disturbance is maintained inside long solid beam, this phenomenon will look like a traveling wave, which moves with a certain speed starting from $0 - B - C - D - E$ and so on. One full wave or often called as wave length (λ) or period (T) is stated from 0 to C or B to D and so on. While a number of full wave in every second is called by frequency (υ) in Hertz. If a wave is able to oscillate 100 times in second, this wave has a frequency of 100 Hertz (Hz). The period for one cycle wave can be describe as

$$T = 1/\upsilon. \tag{2.1}$$

Since the wave has a wave length (λ)and frequency, the distance obtained by the wave in one second is known as a wave speed (c).

$$c = \upsilon.\lambda. \tag{2.2}$$

In the measurement, information regarding intensity or magnitude of the wave is very important. The magnitude (A) at a certain time can be obtained from simple harmonic motion equation,

$$A = A_0.sin(2\pi.\upsilon.t). \tag{2.3}$$

where A_0 is un-attenuated magnitude.

When a wave is traveling, the wave has been affected by time and distance $A(x,t)$.

Let's assume the wave move from x_1 to x_2 in a certain period of t time as shown in Fig. 2.3. The distance x is obtained from $x_2 - x_1$. Thus, the speed of the wave is easily known as $c = x/t$. Now the equation of
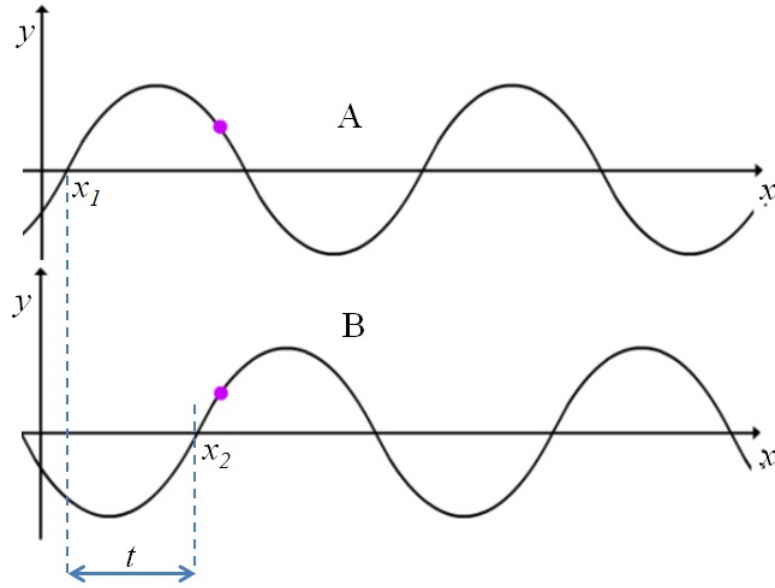
Figure 2.3: A traveling sinusoidal wave

traveling wave can be expressed as

$$A = A_0 . \sin 2\pi (\upsilon . t - \frac{\upsilon}{c} . x) \tag{2.4}$$

Since the frequency and speed are known, then the wave number k can be obtained. Thus, traveling equation can be modified as

$$A = A_0 . \sin(2\pi \upsilon . t - k . x) \tag{2.5}$$

If we refer to the wave equation explained above, we couldn't find the relationship of elastic properties of the medium, in which acoustic wave propagate through it. For this purpose, as a common of wave equation is also presented in the form of partial differential equation. The wave equation below shows one dimensional (1D) wave propagation.

$$\frac{\partial^2 r}{\partial^2 x} = \frac{1}{c^2} \frac{\partial^2 r}{\partial^2 t} \tag{2.6}$$

where c is obtained from square root of young modulus divided by density of the medium. This equation will be solved by using plane wave. The plane wave is presented by a complex formula, shown in equation below.

$$\phi(\overrightarrow{r},t) = \phi_0 \, e^{i(\omega.t - \overrightarrow{k}.\overrightarrow{r})} \tag{2.7}$$

The parameter of r is equal to $\mathbf{x}_{ax} + \mathbf{y}_{ay} + \mathbf{z}_{az}$ means that the plane wave propagate into x, y and z direction. To solve the wave equation for 3 dimensional (3D) wave propagation, we have to use Laplacian operator. A Laplacian operator of a function of $\{F\}$ may be described as

$$\nabla^2\{F\} = \frac{\partial^2}{\partial^2 x}\{F\} + \frac{\partial^2}{\partial^2 y}\{F\} + \frac{\partial^2}{\partial^2 z}\{F\} \tag{2.8}$$

Utilizing Eq. 2.6, now we have 3D wave equation.

$$\nabla^2\phi(\overrightarrow{r},t) = \frac{1}{c^2}\frac{\partial^2}{\partial^2 t}\phi(\overrightarrow{r},t) \tag{2.9}$$

where, the first and second derivation of Eq. 2.7 respect to time and z axis, are

$$\frac{\partial}{\partial t}\phi = i\omega\phi \qquad\qquad \frac{\partial}{\partial z}\phi = ik_z\phi$$

$$\frac{\partial^2}{\partial^2 t}\phi = (i\omega)^2\phi = -\omega^2\phi \qquad\qquad \frac{\partial^2}{\partial^2 z}\phi = -k_z^2\phi$$

The Laplacian of the plane wave is then,

$$\nabla^2\phi = -k^2\phi$$

Substitute the Laplacian of the plane wave and second derivative of plane wave respected to time into Eq. 2.9, then

$$\left[\nabla^2 - \frac{1}{c^2}\frac{\partial^2}{\partial^2 t}\right]\phi = 0 \tag{2.10}$$

$$\left[-k^2 + \frac{\omega^2}{c^2}\right]\phi = 0 \tag{2.11}$$

From the equation above, the solution for wave equation and plane wave is obtained as

$$\omega^2 = c^2 k^2 \tag{2.12}$$

where, this equation is called as "Dispersion Relation".

2.2 Non-sinusoidal Wave

2.2.1 Wave in Time Domain and Frequency Domain

Figure 2.2 illustrates a sinusoidal wave, where y-axis is amplitude of the wave and x-axis is time. For an instance, an electric wave has 1 volt and 4 Hz. In time domain, we can write this wave as

$$A = 1.sin(8\pi.t) \tag{2.13}$$
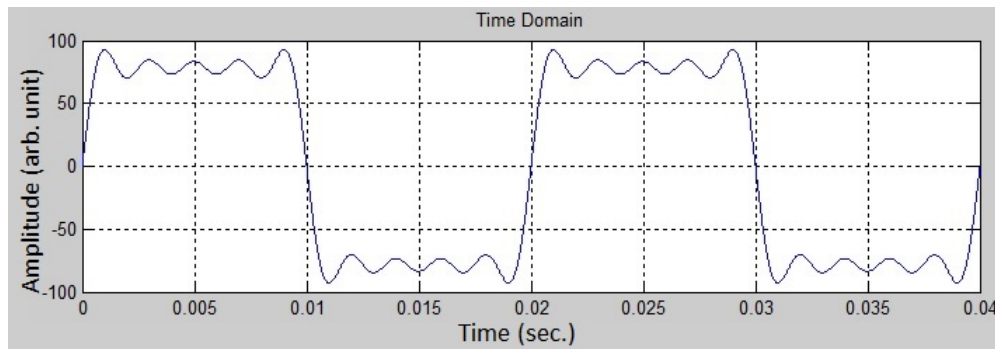
Figure 2.4: A wave summation from several sinusoidal waves.

However, it is very common that the shape of the wave is not always sinusoidal. It may happen, since more than one wave components with different frequency, phase and magnitude are added. This phenomenon will be easier to be known if the shape of the wave in time domain is converted into frequency domain.
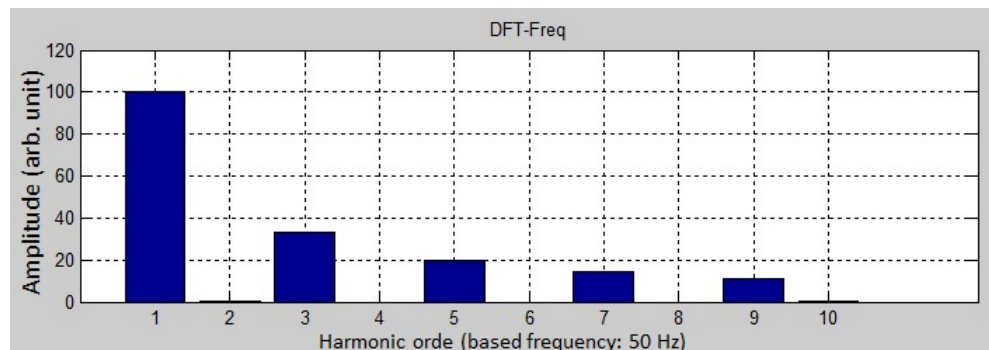
Figure 2.5: Frequency domain at 50, 150, 250, 350 and 450 Hz.

For an instance, a combination of several sine waves with frequencies of 50, 150, 250, 350 and 450 Hz

are added, then a new shape of wave is produced as shown in Fig. 2.4.

The figure above is the wave shape in time domain. It is consists of five waves with different amplitude and different frequency. This figure may be described into its frequency spectrum as shown in the Fig. 2.5.

2.2.2 Fourier Transform

If we refer to the previous sub-chapter, a periodic non-sine wave is determined and shown in time domain. In order to give an easier illustration, thus we may bring into the frequency domain utilizing so called Fourier Transform. As an example, a function $f(x)$ is called periodic if it is defined for all real x and if there is some positive number p such that fulfill $f(x + p) = f(x)$. As an example, the Fig 2.6 shows a periodic wave, which has a period of p.

Let's assume an arbitrary periodic wave shown in the Fig 2.6 has a function of

$$a_0 + a_1 cos(x) + b_1 sin(x) + a_2 cos(x) + b_2 sin(x) + ..., \qquad (2.14)$$

where a_0, a_1, a_2,... b_1, b_2,... are real constants. Such a series is called trigonometric series and the a_n and b_n is called coefficients of the series.
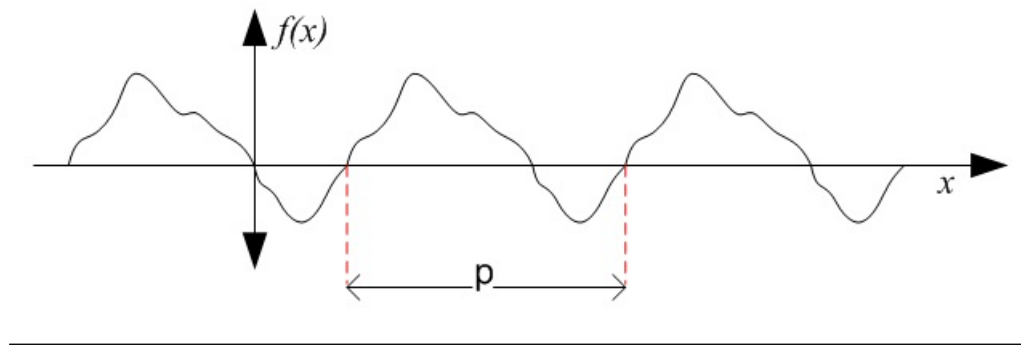
Figure 2.6: An arbitrary periodic wave

We can write the above equation in another notation as

$$f(x) = a_0 + \sum_{n=1}^{N} (a_n cos\, nx + b_n sin\, nx) \qquad (2.15)$$

where, n is the harmonic order.
If the series above is convergent, its sum will be a function of period 2π, where

$$a_0 = \frac{1}{2\pi} \int_{-\pi}^{+\pi} f(x)\,\mathrm{d}x$$

$$a_n = \frac{1}{\pi} \int_{-\pi}^{+\pi} f(x)\cos nx\,\mathrm{d}x$$

$$b_n = \frac{1}{\pi} \int_{-\pi}^{+\pi} f(x)\sin nx\,\mathrm{d}x$$

The frequency spectrum of the wave above can be obtained by defining the Fourier transform of wave function $f(x)$.

$$F(k_x) = \int_{-\infty}^{+\infty} f(x).e^{-j(k_x.x)}\mathrm{d}x. \tag{2.16}$$

In some particular cases, it is also needed to convert frequency spectrum into time domain or real space. For this purpose, we may utilize inverse Fourier transform as shown in the equation below.

$$f(x) = \int_{-\infty}^{+\infty} F(k_x).e^{j(x.k_x)}\mathrm{d}k_x. \tag{2.17}$$

2.3 Boundary Condition at Interface

In this manuscript, we focus the discussion for mechanical wave (acoustic wave). A complete system requires vibration source, medium and receptor to detect the wave. Medium is a substance, which carries the sound energy from a certain point to another point. We make an assumption that the acoustic wave travels through homogeneous medium. Occasionally, a stack of different acoustic properties of homogeneous mediums create multi-layer medium, in which acoustic wave propagates through it. In such a case, an interface (boundary line) between two different mediums is built. An interface built from two mediums is assumed to be perfect interface. In this chapter, we shall describe the effect of a discontinuity in the medium. A reflection and transmission coefficients will be presented as well as the angular dependency.

2.3.1 Snell's Law

When, a wave encounters an interface line, part of its intensity will be reflected, and part of it will be transmitted. The reflected wave (echo) will travel back to the first medium. The transmitted wave will travel into the second medium. If the incident wave comes perpendicular to the interface line (normal incident), the reflected wave will travel in 180° from incident wave direction, and transmitted wave will travel in the same direction of the incident wave. However, if the incident wave comes with some deflection to the interface line, then there are two situations. The reflected wave has equal angle to the incident wave. For the transmitted wave, it must comply Snell's Law, as shown in equation below and Fig. 2.7.

$$\frac{c_1}{sin\ \theta_{pi}} = \frac{c_2}{sin\ \theta_{pt}} \qquad (2.18)$$

where c_1 and c_2 are the speeds of wave inside medium-1 and medium-2, and θ_{pi} and θ_{pt} are the angles of incidence and transmission, respectively.
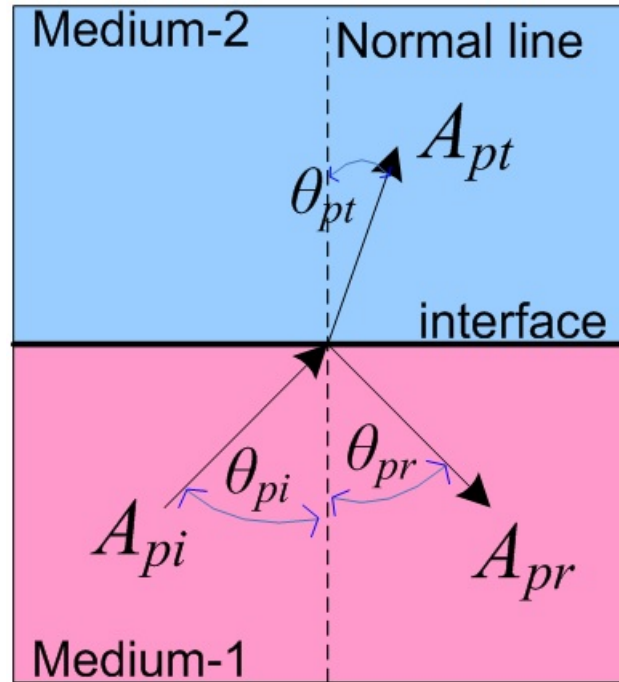
Figure 2.7: Snell's Law

If c_2 is larger than c_1, then sin θ_{pt} is larger than sin θ_{pi}. Consequently θ_{pt} is larger than θ_{pi}. Increasing incident angle θ_{pi}, will be followed by increasing θ_{pt}. If the increment of incident angle is kept on, as a result, θ_{pt} will reach $\pi/2$. At this point, the transmission energy will flow trough the boundary between two mediums (critical angle for incident wave). If we further increase θ_{pi}, then θ_{pt} is larger than $\pi/2$. It implies that there is no transmitted wave, and all energy will be reflected.

2.3.2 Reflection and Transmission Coefficient for Normal Incident

The angular relation between incident, reflected and transmitted waves are known from Snell'a Law. However, the magnitude of reflected and transmitted waves have not been obtained yet. In this subchapter, we will discuss reflection and transmission at normal incident at liquid-liquid interface. Since acoustic wave is a pressure wave, normal incidence will generate only pressure wave. Let's assume acoustic wave that is described in the eq. 2.16 is transmitted from medium-1 into medium-2. Where ϕ_{pi} and A_{pi} are sound

potential and pressure incident wave magnitude, respectively.

$$\phi_{pi} = A_{pi}.e^{j(2\pi.\upsilon.t - k_1.x)} \tag{2.19}$$
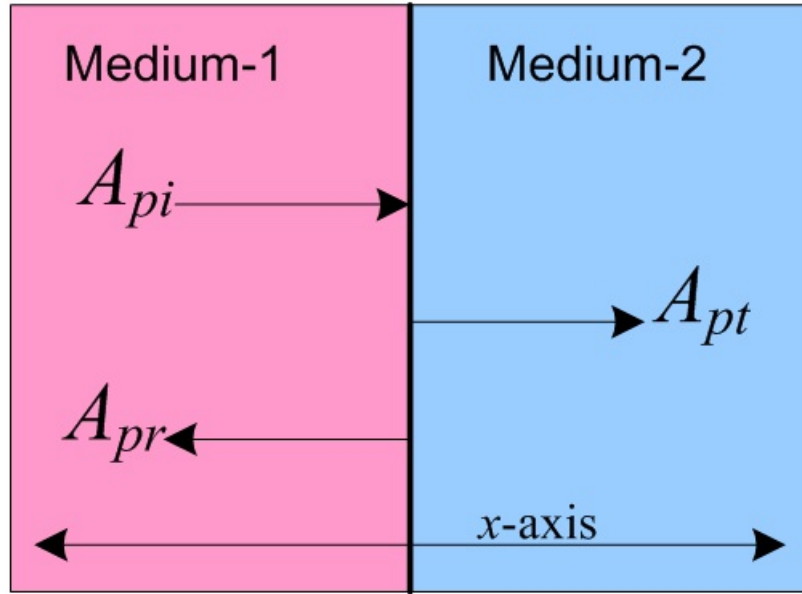
Figure 2.8: Reflection and transmission at normal incidence for planar interface.

When the incident wave is impinging the interface, part of it will be reflected and the other will be transmitted as shown in Fig. 2.8. If the amplitude of incident wave is equal to one, then each reflected and transmitted wave are described in the equation below.

$$\phi_{pr} = A_{pr}.e^{j(2\pi.\upsilon.t + k_1.x)} \tag{2.20}$$

$$\phi_{pt} = A_{pt}.e^{j(2\pi.\upsilon.t - k_2.x)} \tag{2.21}$$

where ϕ_{pr} and ϕ_{pt} are sound potential of reflected and transmitted, and A_{pr} and A_{pt} are reflection and transmission coefficient of pressure wave, respectively.

If the contact of two different mediums is perfectly done, thus there are continuity of pressure and velocity (displacement) at x=0. Then the total energy on the left side is equal to the energy on the right side. Using the definition of acoustic impedance [2], it follows that

$$A_{pr} + 1 = A_{pt} \tag{2.22}$$

$$\frac{1}{Z_1}(1 - A_{pr}) = \frac{A_{pt}}{Z_2} \tag{2.23}$$

where Z_1 and Z_2 are acoustic impedance of medium-1 and medium-2, respectively. Equations 2.22 and 2.23 can be solved to give for pressure reflection and transmission coefficients,

$$A_{pr} = \frac{Z_2 - Z_1}{Z_1 + Z_2} \tag{2.24}$$

$$A_{pt} = \frac{2Z_2}{Z_1 + Z_2} \tag{2.25}$$

2.3.3 Liquid-Liquid Interface

Liquid can change its shape, as it will tailor to the container. Since the bounding of its material is weak, liquid cannot support a static shear stress. Therefore, shear wave in the liquid is very small. For the next description, shear wave will be assumed to be zero, when the wave travels through the liquid. Only pressure wave exists in the liquid material.

When the incident pressure wave is impinging the interface, one part of the wave intensity will be reflected with the reflection angle is same to the incident wave. The other part will be transmitted with the transmission angle follow the Snell's Law calculation. The plane of this paper is composed of x and z axis. Z-axis is in line to the normal line. Y-axis is perpendicular to the plane of the paper. If we assume A_{pi} is equal to one, then we can write those three component waves as:

$$\phi_{pi} = A_{pi}.e^{j(2\pi.\upsilon.t+k_{x1}.x+k_{z1}.z)} \tag{2.26}$$

$$\phi_{pr} = A_{pr}.e^{j(2\pi.\upsilon.t+k_{x1}.x-k_{z1}.z)} \tag{2.27}$$

$$\phi_{pt} = A_{pt}.e^{j(2\pi.\upsilon.t+k_{x2}.x+k_{z2}.z)} \tag{2.28}$$

To meet the boundary condition, pressure potential and normal velocity must be continued at the interface z=0. Pressure potential and normal velocity at the vicinity of interface in medium-1 and medium-2 have to be equal. Refers to [2], reflection and transmission coefficient can be obtained as:

$$A_{pr} = \frac{\frac{\rho_2 c_2}{\cos\theta_2} - \frac{\rho_1 c_1}{\cos\theta_1}}{\frac{\rho_2 c_2}{\cos\theta_2} + \frac{\rho_1 c_1}{\cos\theta_1}} \tag{2.29}$$

$$A_{pt} = \frac{\frac{2\rho_1 c_2}{cos\,\theta_2}}{\frac{\rho_2 c_2}{cos\,\theta_2} + \frac{\rho_1 c_1}{cos\,\theta_1}} \tag{2.30}$$

2.3.4   Solid-Liquid Interface

In the case of liquid-solid interface, pressure distortion and displacement potential at the interface vicinity must be equal. As the previous assumption, shear wave is neglected in liquid, but must be considered in solid. Thus, medium-1 is consists of incidence and reflection pressure wave, and medium-2 consist of transmission pressure and shear waves as shown in Fig. 2.9. The velocity displacement can be written in the liquid and solid as [2]

$$\vec{u} = \overrightarrow{\nabla \phi_p} \tag{2.31}$$

$$\vec{u} = \overrightarrow{\nabla \phi_p} + \overrightarrow{\nabla} \times \overrightarrow{\phi_s} \tag{2.32}$$

While the stress distortion is expressed as

$$\sigma = E(\frac{\partial u_x}{\partial_x} + \frac{\partial u_z}{\partial_z}) + 2G\frac{\partial u_z}{\partial_z} \tag{2.33}$$

where, E and G are compression elastic and shear modulus, respectively.

Assuming an ideal non viscous liquid, three boundary conditions, continuity of normal velocity, continuity of normal stress and zero tangential stress are exist in this layer. In order to determine reflection and transmission coefficient, the results of the stresses and the velocities must be substitute into the boundary conditions.

Three equations coming from the boundary conditions are

$$k_{p1}cos\,\theta_{pi}\phi_i A_{pr} + k_{p2}cos\,\theta_{pt}A_{pt} - k_{s2}sin\,\theta_{st}A_{st} = k_{p1}cos\,\theta_{pi} \tag{2.34}$$

$$k_{p2}^2 sin\,2\theta_{pt}A_{pt} + k_{s2}^2 cos\,2\theta_{st}A_{st} = 0 \tag{2.35}$$

$$\rho_1 A_{pr} + \rho_2 \Big[2\frac{k_{p2}^2}{k_{s2}^2}sin^2\,\theta_{pt} - 1\Big]A_{pt} + \rho_2 sin\,2\theta_{st}A_{st} \tag{2.36}$$

From those equation above, the reflection, transmission pressure and transmission shear coefficient are

21
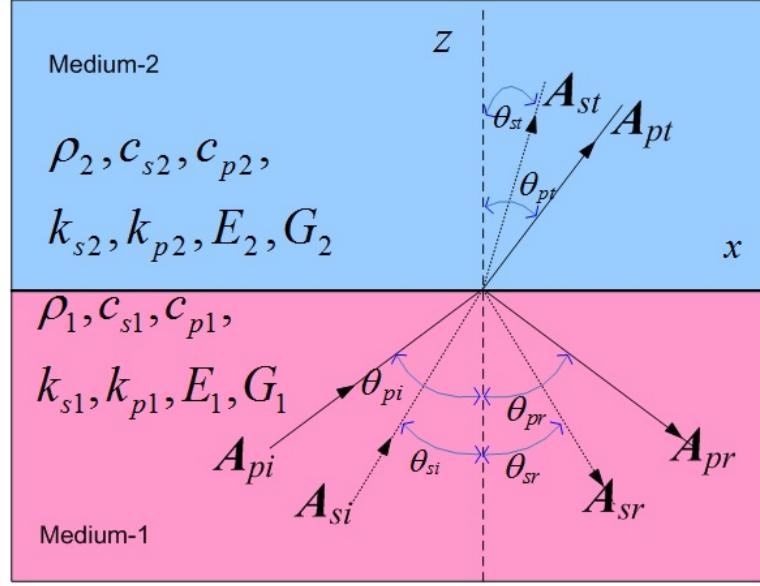
Figure 2.9: Reflection and transmission of oblique incident wave at the interface of two different mediums.

determined [2].

$$A_{pr} = \frac{Z_{2p}cos^2 2\theta_{st} + Z_{2s}sin^2 2\theta_{st} - Z_1}{Z_{2p}cos^2 2\theta_{st} + Z_{2s}sin^2 2\theta_{st} + Z_1} \tag{2.37}$$

$$A_{pt} = (\frac{\rho_1}{\rho_2})\frac{2Z_{2p}cos 2\theta_{st}}{Z_{2p}cos^2 2\theta_{st} + Z_{2s}sin^2 2\theta_{st} + Z_1} \tag{2.38}$$

$$A_{st} = -(\frac{\rho_1}{\rho_2})\frac{2Z_{2s}sin 2\theta_{st}}{Z_{2p}cos^2 2\theta_{st} + Z_{2s}sin^2 2\theta_{st} + Z_1} \tag{2.39}$$

where,

$$Z_1 = \frac{\rho_1 c_1}{cos \theta_{pi}}, \ Z_{2p} = \frac{\rho_2 c_{p2}}{cos \theta_{pt}}, \ Z_{2s} = \frac{\rho_2 c_{s2}}{cos \theta_{st}}.$$

2.3.5 Solid-Solid Interface

In this particular case, medium-1 and medium-2 are solids. As it is already explained in the previous subsection, two boundary conditions are required for solid material. They are velocity potential and stress distortion. The two types of waves, pressure and shear wave are present in both medium-1 and medium-2.

Since shear wave is perpendicular to the wave propagation, there are two types of potential displacements, horizontally (SH) and vertically polarized shear (SV) waves. When SH incident wave presents in the solid-solid interface, it may only generates SH reflection and SH transmission waves. However, if either pressure or SV incident wave presents in solid-solid interface, they generate four types of waves, pressure and SV reflection waves and pressure and SV transmission waves [2, 10], which will be discussed in this section.

If we take a look back to Fiq. 2.9, several parameters are presented there. They are:

A_{si}, A_{pi}: incidence of shear wave and pressure wave,

A_{sr}, A_{pr}: reflection of shear wave and pressure wave,

A_{st}, A_{pt}: transmission of shear wave and pressure wave,

θ_{si}, θ_{pi}: angle of incidence of shear wave and pressure wave,

θ_{sr}, θ_{pr}: angle of reflection of shear wave and pressure wave,

θ_{st}, θ_{pt}: angle of transmission of shear wave and pressure wave,

ρ_1, ρ_2: the density of medium-1 and medium-2,

c_{s1}, c_{s2}: speed of sound of shear wave in medium-1 and medium-2,

c_{p1}, c_{p2}: speed of sound of pressure wave in medium-1 and medium-2,

k_{s1}, k_{s2}: wave number of shear wave in medium-1 and medium-2,

k_{p1}, k_{p2}: wave number of pressure wave in medium-1 and medium-2,

E_1, E_2: compression elastic modulus in medium-1 and medium-2 and

G_1, G_2: shear modulus in medium-a and medium-2.

Where,

$$k_{s1} = \frac{\omega}{c_{s1}}, \qquad\qquad k_{p1} = \frac{\omega}{c_{p1}},$$
$$k_{s2} = \frac{\omega}{c_{s2}}, \qquad\qquad k_{p2} = \frac{\omega}{c_{p2}},$$
$$\frac{E_1 + 2G_1}{\rho_1} = c_{p1}^2, \qquad\qquad \frac{E_2 + 2G_2}{\rho_2} = c_{p2}^2,$$
$$\frac{G_1}{\rho_1} = c_{s1}^2, \qquad\qquad \frac{G_2}{\rho_2} = c_{s2}^2.$$

Thus,

$$G_1 = \rho_1 c_{s1}^2, \qquad\qquad G_2 = \rho_2 c_{s2}^2,$$
$$E_1 = \rho_1 c_{p1}^2 - 2G_1, \qquad\qquad E_2 = \rho_2 c_{p2}^2 - 2G_2.$$

Refers to Eq. 2.26, the displacement of potential of incident wave is equal to $\phi_{pi} = A_{pi}.e^{j(2\pi.v.t + k_{x1}.x - k_{z1}.z)}$, where x and z express the distance along x and z axes, respectively. Since the angle of incidence is known, the distance expressed in x and z may be replaced by either sin or cos of the angle of incidence. The expression of Eq. 2.26 can be then modified as

$$\phi_{pi} = A_{pi}.e^{j(\omega.t+k_{p1}.sin(\theta_{pi})x+k_{p1}.cos(\theta_{pi})z)} \tag{2.40}$$

$$\phi_{si} = A_{si}.e^{j(\omega.t+k_{s1}.sin(\theta_{si})x+k_{s1}.cos(\theta_{si})z)} \tag{2.41}$$

If the number of A_{pi} and A_{si} are assumed to be one, then A_{pr}, A_{pt}, A_{sr} and A_{st} will be reflection and transmission of pressure waves and reflection and transmission of the shear waves, respectively.

$$\phi_{pr} = A_{pr}.e^{j(\omega.t+k_{p1}.sin(\theta_{pr})x-k_{p1}.cos(\theta_{pr})z)} \tag{2.42}$$

$$\phi_{sr} = A_{sr}.e^{j(\omega.t+k_{s1}.sin(\theta_{sr})x-k_{s1}.cos(\theta_{sr})z)} \tag{2.43}$$

$$\phi_{pt} = A_{pt}.e^{j(\omega.t+k_{p2}.sin(\theta_{pt})x+k_{p2}.cos(\theta_{pt})z)} \tag{2.44}$$

$$\phi_{st} = A_{st}.e^{j(\omega.t+k_{s2}.sin(\theta_{st})x+k_{s2}.cos(\theta_{st})z)} \tag{2.45}$$

In order to determine the value of reflection and transmission coefficients, four boundary conditions at the interface between two mediums must be fulfilled. These four boundary conditions are:

a. continuity of particle velocity displacement u_x for $z=0$;

b. continuity of particle velocity displacement u_z for $z=0$;

c. continuity of stress distortion σ of x component for $z=0$;

d. continuity of stress distortion σ of z component for $z=0$;

The particle velocity displacement and stress distortion can be obtained from Eq. 2.32 and Eq. 2.33. From these two equations we shall derived the formula to determine reflection and transmission coefficient. Medium-1 and medium-2 are assumed as uniform material. Since the sound field generated by the transducer is axis-symmetrical to z-axis, we may neglected one of its axis. In this calculation we assumed that there is no displacement in the y axis direction.

The particle velocity displacement u at the interface can be calculated as:

$$\vec{u} = \vec{\nabla\phi_p} + \vec{\nabla} \times \vec{\phi_s}$$

$$\vec{\nabla\phi_p} = \frac{\partial}{\partial_x}\phi_p\,\mathbf{a}_x + \frac{\partial}{\partial_y}\phi_p\,\mathbf{a}_y + \frac{\partial}{\partial_z}\phi_p\,\mathbf{a}_z$$

$$\vec{\nabla\phi_p} = \frac{\partial}{\partial_x}\phi_p\,\mathbf{a}_x + \frac{\partial}{\partial_z}\phi_p\,\mathbf{a}_z$$

where $\frac{\partial}{\partial_y}\phi_p=0$.

$$\vec{\nabla} \times \vec{\phi_s} = \left(\frac{\partial\phi_{sz}}{\partial_y} - \frac{\partial\phi_{sy}}{\partial_z}\right)\mathbf{a}_x + \left(\frac{\partial\phi_{sx}}{\partial_z} - \frac{\partial\phi_{sz}}{\partial_x}\right)\mathbf{a}_y + \left(\frac{\partial\phi_{sy}}{\partial_x} - \frac{\partial\phi_{sx}}{\partial_y}\right)\mathbf{a}_z$$

$$\vec{\nabla} \times \vec{\phi_s} = \left(-\frac{\partial\phi_{sy}}{\partial_z}\right)\mathbf{a}_x + \left(\frac{\partial\phi_{sy}}{\partial_x}\right)\mathbf{a}_z$$

Based on the Eq. 2.32 the particle velocity displacement is calculated and expressed as:

$$\vec{u} = \frac{\partial}{\partial_x}\phi_p\,\mathbf{a}_x + \frac{\partial}{\partial_z}\phi_p\,\mathbf{a}_z + \left(-\frac{\partial\phi_{sy}}{\partial_z}\right)\mathbf{a}_x + \left(\frac{\partial\phi_{sy}}{\partial_x}\right)\mathbf{a}_z \tag{2.46}$$

$$\vec{u} = \left(\frac{\partial}{\partial_x}\phi_p - \frac{\partial}{\partial_z}\phi_{sy}\right)\mathbf{a}_x + \left(\frac{\partial}{\partial_z}\phi_p + \frac{\partial}{\partial_x}\phi_{sy}\right)\mathbf{a}_z \tag{2.47}$$

Now, we try to solve the four boundary conditions for solid-solid interface, as shown in the previous statement. They are:

a. continuity of particle velocity displacement u_x for $z=0$; The particle velocity displacement at the vicinity interface of medium-1 and medium-2 in term of x axis direction must equal.

Particle velocity displacement inside medium-1 can be obtained as,

$u_{x1} = \frac{\partial}{\partial_x}\phi_{p1} - \frac{\partial}{\partial_z}\phi_{s1} = \frac{\partial(\phi_{pi}+\phi_{pr})}{\partial_x} - \frac{\partial(\phi_{si}+\phi_{sr})}{\partial_z}$.
$u_{x1} = (j.k_{p1}.sin\,\theta_{pi}.\phi_{pi} + j.k_{p1}.sin\,\theta_{pr}.\phi_{pr}) - (j.k_{s1}.cos\,\theta_{si}.\phi_{si} - j.k_{s1}.cos\,\theta_{sr}.\phi_{sr})$

Particle velocity displacement inside medium-2 can be obtained as,

$u_{x2} = \frac{\partial}{\partial_x}\phi_{p2} - \frac{\partial}{\partial_z}\phi_{s2} = \frac{\partial\phi_{pt}}{\partial_x} - \frac{\partial\phi_{st}}{\partial_z}$.
$u_{x2} = (j.k_{p2}.sin\,\theta_{pt}.\phi_{pt}) - (j.k_{s2}.sin\,\theta_{st}.\phi_{st})$

In order to fulfill the continuity at the interface, then

$u_{x1} = u_{x2}$.
$(j.k_{p1}.sin\,\theta_{pi}.\phi_{pi} + j.k_{p1}.sin\,\theta_{pr}.\phi_{pr}) - (j.k_{s1}.cos\,\theta_{si}.\phi_{si} - j.k_{s1}.cos\,\theta_{sr}.\phi_{sr}) =$
$(j.k_{p2}.sin\,\theta_{pt}.\phi_{pt}) - (j.k_{s2}.sin\,\theta_{st}.\phi_{st})$

From the Snell's Law,

$\frac{c_1}{sin\,\theta_1} = \frac{c_2}{sin\,\theta_2} \Leftrightarrow \frac{\omega/k_1}{sin\,\theta_1} = \frac{\omega/k_2}{sin\,\theta_2}$, thus we obtained that $k_{p1}\,sin\,\theta_{pi} = k_{p1}\,sin\,\theta_{pr} = k_{p2}\,sin\,\theta_{pt} = k_{s1}\,sin\,\theta_{si} = k_{s1}\,sin\,\theta_{sr} = k_{s2}\,sin\,\theta_{st}$ of which the existence of exponential equation might be neglected on both equations side. We also may neglected complex function (j) on both equations. After the common components are neglected, we derived the solution of the continuity for particle velocity displacement u_x for $z=0$, and it is expressed as:

$$A_{pi}.k_{p1}.sin\,\theta_{pi} + A_{pr}.k_{p1}.sin\,\theta_{pr} + A_{sr}.k_{s1}.cos\,\theta_{sr} - A_{si}.k_{s1}.cos\,\theta_{si} =$$
$$A_{pt}.k_{p2}.sin\,\theta_{pt} - A_{st}.k_{s2}.cos\,\theta_{st}. \tag{2.48}$$

b. continuity of particle velocity displacement u_z for $z=0$; The particle velocity displacement at the vicinity interface of medium-1 and medium-2 in term of z axis direction must equal.

$u_{z1} = u_{z2}$.

The particle velocity displacement inside medium-1 and medium-2 can be obtained as the following explanation.

$u_{z1} = \frac{\partial}{\partial_z}\phi_{p1} + \frac{\partial}{\partial_x}\phi_{s1} = \frac{\partial(\phi_{pi}+\phi_{pr})}{\partial_z} + \frac{\partial(\phi_{si}+\phi_{sr})}{\partial_x}$.

$u_{z2} = \frac{\partial}{\partial_z}\phi_{p2} + \frac{\partial}{\partial_x}\phi_{s2} = \frac{\partial\phi_{pt}}{\partial_z} + \frac{\partial\phi_{st}}{\partial_x}$.

After doing derivation of the sound potential to the respected axis, thus particle velocity displacement in term of z-axis direction can be obtained as,

$u_{z1} = (j.k_{p1}.cos\,\theta_{pi}.\phi_{pi} - j.k_{p1}.cos\,\theta_{pr}.\phi_{pr}) + (j.k_{s1}.sin\,\theta_{si}.\phi_{si} + j.k_{s1}.sin\,\theta_{sr}.\phi_{sr})$

$u_{z2} = j.k_{p2}.cos\,\theta_{pt}.\phi_{pt} + j.k_{s2}.sin\,\theta_{st}.\phi_{st}$

From the equations above, we derived the solution of the continuity for particle velocity displacement u_z for $z=0$ by the same manner as explained in item [a.] and it is expressed as:

$$A_{pi}.k_{p1}.cos\,\theta_{pi} - A_{pr}.k_{p1}.cos\,\theta_{pr} + A_{si}.k_{s1}.sin\,\theta_{si} + A_{sr}.k_{s1}.sin\,\theta_{sr} =$$
$$A_{pt}.k_{p2}.cos\,\theta_{pt} + A_{st}.k_{s2}.sin\,\theta_{st}. \tag{2.49}$$

c. continuity of stress distortion σ of z component for $z=0$; The stress distortion at the vicinity interface of medium-1 and medium-2 in term of z axis direction must equal. Stress distortion is calculated from the first derivation of the particle velocity displacement, which is obtained from the previous calculation.

For the stress distortion inside medium-1 can be obtained from the equation below.

$\sigma_{z1} = E_1\left[\frac{\partial u_{x1}}{\partial_x} + \frac{\partial u_{z1}}{\partial_z}\right] + 2G_1\frac{\partial u_{z1}}{\partial_z}$,

where,

$\frac{\partial u_{x1}}{\partial_x} = (j.k_{p1}.sin\,\theta_{pi}.\frac{\partial\phi_{pi}}{\partial_x} + j.k_{p1}.sin\,\theta_{pr}.\frac{\partial\phi_{pr}}{\partial_x}) -$

$(j.k_{s1}.cos\,\theta_{si}.\frac{\partial\phi_{si}}{\partial_x} + j.k_{s1}.cos\,\theta_{sr}.\frac{\partial\phi_{sr}}{\partial_x})$,

$\frac{\partial u_{x1}}{\partial_x} = -k_{p1}^2.sin^2\,\theta_{pi}.\phi_{pi} - k_{p1}^2.sin^2\,\theta_{pr}.\phi_{pr} + k_{s1}^2.sin\,\theta_{si}.cos\,\theta_{si}.\phi_{si} -$

$k_{s1}^2.sin\,\theta_{sr}.cos\,\theta_{sr}.\phi_{sr}$,

and

$\frac{\partial u_{z1}}{\partial_z} = (j.k_{p1}.cos\,\theta_{pi}.\frac{\partial\phi_{pi}}{\partial_z} - j.k_{p1}.cos\,\theta_{pr}.\frac{\partial\phi_{pr}}{\partial_z}) +$

$(j.k_{s1}.sin\,\theta_{si}.\frac{\partial\phi_{si}}{\partial_z} + j.k_{s1}.sin\,\theta_{sr}.\frac{\partial\phi_{sr}}{\partial_z})$,

$\frac{\partial u_{z1}}{\partial_z} = -k_{p1}^2.cos^2\,\theta_{pi}.\phi_{pi} - k_{p1}^2.cos^2\,\theta_{pr}.\phi_{pr} - k_{s1}^2.sin\,\theta_{si}.cos\,\theta_{si}.phi_{si} +$

$k_{s1}^2.sin\,\theta_{sr}.cos\,\theta_{sr}.\phi_{sr}$.

Thus, the total stress distortion inside medium-1 is

$\sigma_{z1} = -E_1.k_{p1}^2.sin^2\,\theta_{pi}.\phi_{pi} - E_1.k_{p1}^2.sin^2\,\theta_{pr}.\phi_{pr} - E_1.k_{p1}^2.cos^2\,\theta_{pi}.\phi_{pi} -$

$E_1.k_{p1}^2.cos^2\,\theta_{pr}.\phi_{pr} - 2G_1.k_{p1}^2.cos^2\,\theta_{pi}.\phi_{pi} - 2G_1.k_{p1}^2.cos^2\,\theta_{pr}.\phi_{pr} -$

$2G_1.k_{s1}^2.sin\,\theta_{si}.cos\,\theta_{si}.\phi_{si} + 2G_1.k_{s1}^2.sin\,\theta_{sr}.cos\,\theta_{sr}.\phi_{sr}$

While the stress distortion inside medium-2 can be obtained from the equation below.

$$\sigma_{z2} = E_2 \left[\frac{\partial u_{x2}}{\partial_x} + \frac{\partial u_{z2}}{\partial_z} \right] + 2G_1 \frac{\partial u_{2z}}{\partial_z},$$

where,

$$\frac{\partial u_{x2}}{\partial_x} = j.k_{p2}.sin\,\theta_{pt}.\frac{\partial \phi_{pt}}{\partial_x} - j.k_{s2}.cos\,\theta_{st}.\frac{\partial \phi_{st}}{\partial_x},$$

$$\frac{\partial u_{x2}}{\partial_x} = -k_{p2}^2.sin^2\,\theta_{pt}.\phi_{pt} + k_{s2}^2.sin\,\theta_{st}.cos\,\theta_{st}.\phi_{st},$$

and

$$\frac{\partial u_{z2}}{\partial_z} = j.k_{p2}.cos\,\theta_{pt}.\frac{\partial \phi_{pt}}{\partial_z} + j.k_{s2}.sin\,\theta_{st}.\frac{\partial \phi_{st}}{\partial_z}),$$

$$\frac{\partial u_{z2}}{\partial_z} = -k_{p2}^2.cos^2\,\theta_{pt}.\phi_{pt} - k_{s2}^2.sin\,\theta_{st}.cos\,\theta_{st}.\phi_{st}.$$

Thus, the total stress distortion inside medium-2 is

$$\sigma_{z2} = -E_2.k_{p2}^2.sin^2\,\theta_{pt}.\phi_{pt} - E_2.k_{p2}^2.cos^2\,\theta_{pt}.\phi_{pt} - 2G_2.k_{p2}^2.cos^2\,\theta_{pt}.\phi_{pt} -$$

$$2G_2.k_{s2}^2.sin\,\theta_{st}.cos\,\theta_{st}.\phi_{pt}$$

For continuity,

$$\sigma_{z1} = \sigma_{z2}, \text{ thus,}$$

$$-E_1.k_{p1}^2.sin^2\,\theta_{pi}.\phi_{pi} - E_1.k_{p1}^2.sin^2\,\theta_{pr}.\phi_{pr} - E_1.k_{p1}^2.cos^2\,\theta_{pi}.\phi_{pi} -$$

$$E_1.k_{p1}^2.cos^2\,\theta_{pr}.\phi_{pr} - 2G_1.k_{p1}^2.cos^2\,\theta_{pi}.\phi_{pi} - 2G_1.k_{p1}^2.cos^2\,\theta_{pr}.\phi_{pr} -$$

$$2G_1.k_{s1}^2.sin\,\theta_{si}.cos\,\theta_{si}.\phi_{si} + 2G_1.k_{s1}^2.sin\,\theta_{sr}.cos\,\theta_{sr}.\phi_{sr} = \qquad (2.50)$$

$$-E_2.k_{p2}^2.sin^2\,\theta_{pt}.\phi_{pt} - E_2.k_{p2}^2.cos^2\,\theta_{pt}.\phi_{pt} - 2G_2.k_{p2}^2.cos^2\,\theta_{pt}.\phi_{pt} -$$

$$2G_2.k_{s2}^2.sin\,\theta_{st}.cos\,\theta_{st}.\phi_{st}$$

After the common components are omitted, we derived the solution of the continuity for stress distortion σ_z for $z=0$, and it is expressed as:

$$-E_1.k_{p1}^2.sin^2\,\theta_{pi}.A_{pi} - E_1.k_{p1}^2.sin^2\,\theta_{pr}.A_{pr} - E_1.k_{p1}^2.cos^2\,\theta_{pi}.A_{pi} -$$

$$E_1.k_{p1}^2.cos^2\,\theta_{pr}.A_{pr} - 2G_1.k_{p1}^2.cos^2\,\theta_{pi}.A_{pi} - 2G_1.k_{p1}^2.cos^2\,\theta_{pr}.A_{pr} -$$

$$2G_1.k_{s1}^2.sin\,\theta_{si}.cos\,\theta_{si}.A_{si} + 2G_1.k_{s1}^2.sin\,\theta_{sr}.cos\,\theta_{sr}.A_{sr} = \qquad (2.51)$$

$$-E_2.k_{p2}^2.sin^2\,\theta_{pt}.A_{pt} - E_2.k_{p2}^2.cos^2\,\theta_{pt}.A_{pt} - 2G_2.k_{p2}^2.cos^2\,\theta_{pt}.A_{pt} -$$

$$2G_2.k_{s2}^2.sin\,\theta_{st}.cos\,\theta_{st}.A_{st}$$

d. continuity of stress distortion σ of x component for $z=0$; The stress distortion at the vicinity interface of medium-1 and medium-2 in term of x axis direction must equal.

$$\sigma_{x1} = \sigma_{x2}$$

For the stress distortion inside medium-1 can be obtained from the equation below.

$$\sigma_{x1} = G_1 \left[\frac{\partial u_{x1}}{\partial_z} + \frac{\partial u_{z1}}{\partial_x} \right].$$

While the stress distortion inside medium-2 can be obtained from the equation below.

$$\sigma_{x2} = G_2 \left[\frac{\partial u_{x2}}{\partial_z} + \frac{\partial u_{z2}}{\partial_x} \right].$$

Thus, the total stress distortion inside medium-1 is

$$\sigma_{x2} = -E_2.k_{p2}^2.sin^2\,\theta_{pt}.\phi_{pt} - E_2.k_{p2}^2.cos^2\,\theta_{pt}.\phi_{pt} - 2G_2.k_{p2}^2.cos^2\,\theta_{pt}.\phi_{pt} -$$
$$2G_2.k_{s2}^2.sin\,\theta_{st}.cos\,\theta_{st}.\phi_{pt}$$

For continuity,

$\sigma_{x1} = \sigma_{x2}$, thus, by doing the same manner, the fourth boundary condition is obtained.

$$G_1.k_{s1}^2.sin^2\,\theta_{sr}.\phi_{sr} - G_1.k_{s1}^2.cos^2\,\theta_{sr}.\phi_{sr} + G_1.k_{s1}^2.sin^2\,\theta_{si}.\phi_{si} -$$
$$G_1.k_{s1}^2.cos^2\,\theta_{si}.\phi_{si} - 2G_1.k_{p1}^2.sin\,\theta_{pr}.cos\,\theta_{pr}.\phi_{pr} + 2G_1.k_{p1}^2.sin\,\theta_{pi}.cos\,\theta_{pi}.\phi_{pi} = \qquad (2.52)$$
$$G_2.k_{s2}^2.sin^2\,\theta_{st}.\phi_{st} - G_2.k_{s2}^2.cos^2\,\theta_{st}.\phi_{st} + 2G_2.k_{p2}^2.sin\,\theta_{pt}.cos\,\theta_{pt}.\phi_{pt}$$

After the common components are omitted, we derived the solution of the continuity for stress distortion σ_z for z=0, and it is expressed as:

$$G_1.k_{s1}^2.sin^2\,\theta_{sr}.A_{sr} - G_1.k_{s1}^2.cos^2\,\theta_{sr}.A_{sr} + G_1.k_{s1}^2.sin^2\,\theta_{si}.A_{si} -$$
$$G_1.k_{s1}^2.cos^2\,\theta_{si}.A_{si} - 2G_1.k_{p1}^2.sin\,\theta_{pr}.cos\,\theta_{pr}.A_{pr} + 2G_1.k_{p1}^2.sin\,\theta_{pi}.cos\,\theta_{pi}.A_{pi} = \qquad (2.53)$$
$$G_2.k_{s2}^2.sin^2\,\theta_{st}.A_{st} - G_2.k_{s2}^2.cos^2\,\theta_{st}.A_{st} + 2G_2.k_{p2}^2.sin\,\theta_{pt}.cos\,\theta_{pt}.A_{pt}$$

The equations of four boundary conditions has been achieved as shown in the Eq. 2.48, Eq. 2.49, Eq. 2.51 and Eq. 2.53. From those equation we attempt to formulate into matrix form. The component of incident waves are separated from the reflection and transmission waves.

$$\left(\begin{array}{cc} k_{s1}.cos\,\theta_{sr} & k_{p1}.sin\,\theta_{pr} \\ -k_{s1}.sin\,\theta_{sr} & k_{p1}.cos\,\theta_{pr} \\ 2G_1.k_{s1}^2(sin\,\theta_{sr}\,cos\,\theta_{sr}) & -E_1.k_{p1}^2 - 2G_1.k_{p1}^2.cos^2\,\theta_{pr} \\ -G_1.k_{s1}^2(cos^2\,\theta_{sr} - sin^2\,\theta_{sr}) & -2G_1.k_{p1}^2(sin\,\theta_{pr}\,cos\,\theta_{pr}) \end{array}\right.$$

$$\left.\begin{array}{cc} k_{s2}.cos\,\theta_{st} & -k_{p2}.sin\,\theta_{pt} \\ k_{s2}.sin\,\theta_{st} & k_{p2}.cos\,\theta_{pt} \\ 2G_2.k_{s2}^2(sin\,\theta_{st}\,cos\,\theta_{st}) & E_2.k_{p2}^2 + 2G_2.k_{p2}^2.cos^2\,\theta_{pt} \\ G_2.k_{s2}^2(cos^2\,\theta_{st} - sin^2\,\theta_{st}) & -2G_2.k_{p2}^2(sin\,\theta_{pt}\,cos\,\theta_{pt}) \end{array}\right) \left(\begin{array}{c} A_{sr} \\ A_{pr} \\ A_{st} \\ A_{pt} \end{array}\right)$$

$$= \left(\begin{array}{cc} k_{s1}.cos\,\theta_{si} & -k_{p1}.sin\,\theta_{pi} \\ k_{s1}.sin\,\theta_{si} & k_{p1}.cos\,\theta_{pi} \\ 2G_1.k_{s1}^2(sin\,\theta_{si}\,cos\,\theta_{si}) & E_1.k_{p1}^2 + 2G_1.k_{p1}^2.cos^2\,\theta_{pi} \\ G_1.k_{s1}^2(cos^2\,\theta_{si} - sin^2\,\theta_{si}) & -2G_1.k_{p1}^2(sin\,\theta_{pi}\,cos\,\theta_{pi}) \end{array}\right) \left(\begin{array}{c} A_{si} \\ A_{pi} \end{array}\right). \qquad (2.54)$$

When the parameters such as,

$k_{p1} = (\frac{\omega^2 \rho_1}{E_1+2G_1})^{1/2}$, $k_{s1} = (\frac{\omega^2 \rho_1}{G_1})^{1/2}$, $k_{p2} = (\frac{\omega^2 \rho_2}{E_2+2G_2})^{1/2}$ and $k_{s2} = (\frac{\omega^2 \rho_2}{G_2})^{1/2}$ are substituted into the equation above then,

$$
\left(
\begin{array}{cc}
k_{s1}.cos\,\theta_{sr} & k_{p1}.sin\,\theta_{pr} \\
-k_{s1}.sin\,\theta_{sr} & k_{p1}.cos\,\theta_{pr} \\
2\omega^2.\rho_1(sin\,\theta_{sr}\,cos\,\theta_{sr}) & -\frac{\omega^2 \rho_1}{E_1+2G_1}(E_1+2G_1.cos^2\,\theta_{pr}) \\
-\omega^2.\rho_1(cos^2\,\theta_{sr}-sin^2\,\theta_{sr}) & -2G_1\frac{\omega^2 \rho_1}{E_1+2G_1}(sin\,\theta_{pr}\,cos\,\theta_{pr})
\end{array}
\right.
$$

$$
\left.
\begin{array}{cc}
k_{s2}.cos\,\theta_{st} & -k_{p2}.sin\,\theta_{pt} \\
k_{s2}.sin\,\theta_{st} & k_{p2}.cos\,\theta_{pt} \\
2\omega^2.\rho_2(sin\,\theta_{st}\,cos\,\theta_{st}) & \frac{\omega^2 \rho_2}{E_2+2G_2}(E_2+2G_2.cos^2\,\theta_{pt}) \\
\omega^2.\rho_2(cos^2\,\theta_{st}-sin^2\,\theta_{st}) & -2G_2\frac{\omega^2 \rho_2}{E_2+2G_2}(sin\,\theta_{pt}\,cos\,\theta_{pt})
\end{array}
\right)
\left(
\begin{array}{c}
A_{sr} \\
A_{pr} \\
A_{st} \\
A_{pt}
\end{array}
\right)
$$

$$
= \left(
\begin{array}{cc}
k_{s1}cos\,\theta_{si} & -k_{p1}sin\,\theta_{pi} \\
k_{s1}sin\,\theta_{si} & k_{p1}cos\,\theta_{pi} \\
2\omega^2.\rho_1(sin\,\theta_{si}\,cos\,\theta_{si}) & \frac{\omega^2 \rho_1}{E_1+2G_1}(E_1+2G_1.cos^2\,\theta_{pi}) \\
\omega^2.\rho_1(cos^2\,\theta_{si}-sin^2\,\theta_{si}) & -2G_1\frac{\omega^2 \rho_1}{E_1+2G_1}(sin\,\theta_{pi}\,cos\,\theta_{pi})
\end{array}
\right)
\left(
\begin{array}{c}
A_{si} \\
A_{pi}
\end{array}
\right). \qquad (2.55)
$$

From the equation above, we may substitute the trigonometry functions below into the equation.

$$2\sin\theta\cos\theta = \sin 2\theta$$
$$\cos^2\theta - \sin^2\theta = \cos 2\theta$$
$$\cos^2\theta = 1 - \sin^2\theta$$

After substitute the trigonometry function above, thus we obtained

$$
\left(
\begin{array}{cc}
k_{s1}.\cos\theta_{sr} & k_{p1}.\sin\theta_{pr} \\
-k_{s1}.\sin\theta_{sr} & k_{p1}.\cos\theta_{pr} \\
\omega^2.\rho_1(\sin 2\theta_{sr}) & -\frac{\omega^2 \rho_1}{E_1+2G_1}(E_1+2G_1-2G_1\sin^2\theta_{pr}) \\
-\omega^2.\rho_1(\cos 2\theta_{sr}) & \frac{\omega^2 G_1 \rho_1}{E_1+2G_1}(\sin 2\theta_{pr})
\end{array}
\right.
$$

$$
\left.
\begin{array}{cc}
k_{s2}.\cos\theta_{st} & -k_{p2}.\sin\theta_{pt} \\
k_{s2}.\sin\theta_{st} & k_{p2}.\cos\theta_{pt} \\
\omega^2.\rho_2(\sin 2\theta_{st}) & -\frac{\omega^2 \rho_2}{E_2+2G_2}(E_2+2G_2-2G_2\sin^2\theta_{pt}) \\
-\omega^2.\rho_2(\cos 2\theta_{st}) & \frac{\omega^2 G_2 \rho_2}{E_2+2G_2}(\sin 2\theta_{pt})
\end{array}
\right)
\left(
\begin{array}{c}
A_{sr} \\
A_{pr} \\
A_{st} \\
A_{pt}
\end{array}
\right)
$$

$$= \begin{pmatrix} k_{s1}\cos\theta_{si} & -k_{p1}\sin\theta_{pi} \\ k_{s1}\sin\theta_{si} & k_{p1}\cos\theta_{pi} \\ \omega^2.\rho_1(\sin 2\theta_{si}) & \frac{\omega^2\rho_1}{E_1+2G_1}(E_1+2G_1-2G_1\sin^2\theta_{pi}) \\ \omega^2.\rho_1(\cos 2\theta_{si}) & -\frac{\omega^2 G_1 \rho_1}{E_1+2G_1}(\sin 2\theta_{pi}) \end{pmatrix} \begin{pmatrix} A_{si} \\ A_{pi} \end{pmatrix}. \tag{2.56}$$

Since on both side has ω^2, we may neglect its existence in that above equation. In addition, if the Snell's Law $k_{p1}\sin\theta_{pi} = k_{s1}\sin\theta_{si}$ and $k_{p2}\sin\theta_{pt} = k_{s2}\sin\theta_{st}$ thus we will have

$(\frac{\omega^2.\rho_1}{E_1+2G_1})^{1/2}\sin\theta_{pi} = (\frac{\omega^2.\rho_1}{G_1})^{1/2}\sin\theta_{si}$
$(\frac{\omega^2.\rho_2}{E_2+2G_2})^{1/2}\sin\theta_{pt} = (\frac{\omega^2.\rho_2}{G_2})^{1/2}\sin\theta_{st}$

Also if we square both side, thus we have

$\frac{\rho_1}{E_1+2G_1}\sin^2\theta_{pi} = \frac{\rho_1}{G_1}\sin^2\theta_{si}$
$\frac{\rho_2}{E_2+2G_2}\sin^2\theta_{pt} = \frac{\rho_2}{G_2}\sin^2\theta_{st}$

From trigonometry, we have $1 - 2\sin^2\theta = \cos 2\theta$. If we utilizing those equation above and substitute into Eq. 2.54, then we obtain

$$\begin{pmatrix} k_{s1}.\cos\theta_{sr} & k_{p1}.\sin\theta_{pr} & k_{s2}.\cos\theta_{st} & -k_{p2}.\sin\theta_{pt} \\ -k_{s1}.\sin\theta_{sr} & k_{p1}.\cos\theta_{pr} & k_{s2}.\sin\theta_{st} & k_{p2}.\cos\theta_{pt} \\ \rho_1\sin 2\theta_{sr} & -\rho_1\cos 2\theta_{sr} & \rho_2\sin 2\theta_{st} & \rho_2\cos 2\theta_{st} \\ -\rho_1\cos 2\theta_{sr} & -\frac{G_1\rho_1}{E_1+2G_1}\sin 2\theta_{pr} & \rho_2\cos 2\theta_{st} & -\frac{G_2\rho_2}{E_2+2G_2}\sin 2\theta_{pt} \end{pmatrix} \begin{pmatrix} A_{sr} \\ A_{pr} \\ A_{st} \\ A_{pt} \end{pmatrix}$$

$$= \begin{pmatrix} k_{s1}\cos\theta_{si} & -k_{p1}\sin\theta_{pi} \\ k_{s1}\sin\theta_{si} & k_{p1}\cos\theta_{pi} \\ \rho_1\sin 2\theta_{si} & \rho_1\cos 2\theta_{si} \\ \rho_1\cos 2\theta_{si} & -\frac{G_1\rho_1}{E_1+2G_1}\sin 2\theta_{pi} \end{pmatrix} \begin{pmatrix} A_{si} \\ A_{pi} \end{pmatrix}. \tag{2.57}$$

Separating similar parameters,

$$\begin{pmatrix} k_{s1} & k_{p1} & k_{s2} & -k_{p2} \\ -k_{s1} & k_{p1} & k_{s2} & k_{p2} \\ \rho_1 & -\rho_1 & \rho_2 & \rho_2 \\ -\rho_1 & -\frac{G_1\rho_1}{E_1+2G_1} & \rho_2 & -\frac{G_2\rho_2}{E_2+2G_2} \end{pmatrix} . \begin{pmatrix} \cos\theta_{sr} & \sin\theta_{pr} & \cos\theta_{st} & \sin\theta_{pt} \\ \sin\theta_{sr} & \cos\theta_{pr} & \sin\theta_{st} & \cos\theta_{pt} \\ \sin 2\theta_{sr} & \cos 2\theta_{sr} & \sin 2\theta_{st} & \cos 2\theta_{st} \\ \cos 2\theta_{sr} & \sin 2\theta_{pr} & \cos 2\theta_{st} & \sin 2\theta_{pt} \end{pmatrix}$$

$$
\begin{pmatrix} A_{sr} \\ A_{pr} \\ A_{st} \\ A_{pt} \end{pmatrix} = \begin{pmatrix} k_{s1} & -k_{p1} \\ k_{s1} & k_{p1} \\ \rho_1 & \rho_1 \\ \rho_1 & -\frac{G_1\rho_1}{E_1+2G_1} \end{pmatrix} \cdot \begin{pmatrix} \cos\theta_{si} & \sin\theta_{pi} \\ \sin\theta_{si} & \cos\theta_{pi} \\ \sin 2\theta_{si} & \cos 2\theta_{si} \\ \cos 2\theta_{si}) & \sin 2\theta_{pi} \end{pmatrix} \begin{pmatrix} A_{si} \\ A_{pi} \end{pmatrix}.
\tag{2.58}
$$

Because θ_{si} isn't always defined when the longitudinal wave stand for input wave, thus θ_{sr} may be used instead of incident angle. This situation is also applied for opposite condition, when θ_{si} is not defined. Thus the equation above can be modified as the equation below.

$$
\begin{pmatrix} k_{s1} & k_{p1} & k_{s2} & -k_{p2} \\ -k_{s1} & k_{p1} & k_{s2} & k_{p2} \\ \rho_1 & -\rho_1 & \rho_2 & \rho_2 \\ -\rho_1 & -\frac{G_1\rho_1}{E_1+2G_1} & \rho_2 & -\frac{G_2\rho_2}{E_2+2G_2} \end{pmatrix} \cdot \begin{pmatrix} \cos\theta_{sr} & \sin\theta_{pr} & \cos\theta_{st} & \sin\theta_{pt} \\ \sin\theta_{sr} & \cos\theta_{pr} & \sin\theta_{st} & \cos\theta_{pt} \\ \sin 2\theta_{sr} & \cos 2\theta_{sr} & \sin 2\theta_{st} & \cos 2\theta_{st} \\ \cos 2\theta_{sr} & \sin 2\theta_{pr} & \cos 2\theta_{st} & \sin 2\theta_{pt} \end{pmatrix}
$$

$$
\begin{pmatrix} A_{sr} \\ A_{pr} \\ A_{st} \\ A_{pt} \end{pmatrix} = \begin{pmatrix} k_{s1} & -k_{p1} \\ k_{s1} & k_{p1} \\ \rho_1 & \rho_1 \\ \rho_1 & -\frac{G_1\rho_1}{E_1+2G_1} \end{pmatrix} \cdot \begin{pmatrix} \cos\theta_{sr} & \sin\theta_{pr} \\ \sin\theta_{sr} & \cos\theta_{pr} \\ \sin 2\theta_{sr} & \cos 2\theta_{sr} \\ \cos 2\theta_{sr}) & \sin 2\theta_{pr} \end{pmatrix} \begin{pmatrix} A_{si} \\ A_{pi} \end{pmatrix}.
\tag{2.59}
$$

2.4 Sound Potential

Sound potential is one of the substance that must be calculated in our research. We need to calculate sound potential and compared to the result from measurement to verify whether the calculation method is correct. We first assume that a sound is generated from a small vibrating source. This will be important and we need a fundamental derivation of calculation, since the shape of transducer have several variations form.

Refers to [59] on chapter 3, in spherical coordinates for a wave whose components vary as $\exp(j\omega t)$, this equation can be written as

$$
\frac{1}{r^2}\frac{\partial}{\partial r}\left(r^2\frac{\partial\phi}{\partial r}\right) + k^2\phi = 0
\tag{2.60}
$$

where $k = \omega/c$. The solution of the equation above is

$$
\phi = A\frac{e^{\pm j.k.r}}{r}
\tag{2.61}
$$

The - sign corresponds to a spherical wave propagating outward from the original and the + sign

corresponds to one propagating in toward it.

2.5 Acoustic Impedance

By definition, acoustic impedance is defined as the measure of the opposition that a system presents to the acoustic flow resulting of an acoustic pressure applied to the system [60]. In the field fluid mechanic, a wave traveling through a material element will induce a gradient in the pressure applied at its two opposite faces along the wave propagation direction [61]. Pressure gradient raised in the material is determined by the density at the state of equilibrium and particle acceleration which is obtained from twice derivation of displacement potential $\phi = \phi_0 \cos(\omega t - kz)$. If the velocity potential function ϑ meet the equation of

$$\frac{\partial \varphi}{\partial z} = \dot{\phi} \tag{2.62}$$

the excessive pressure that arises inside the material, when a mechanical wave propagates through, can be described by the equation below.

$$\triangle P = P - P_0 = -\rho \frac{\partial \varphi}{\partial t} \tag{2.63}$$

where,

$$\varphi = \int \dot{\phi}\, \mathrm{d}x = -\left(\frac{\dot{\phi}_0}{k}\right)\sin(\omega t - kz) \tag{2.64}$$

By inserting Eq. 2.64 into Eq. 2.63, thus we obtain

$$\triangle P = -\rho\frac{\partial \varphi}{\partial t} = \rho\left(\frac{\omega}{k}\right)\dot{\phi}_0\cos(\omega t - kz).$$

Replacing ratio of angular frequency and wave number in the bracket by speed, thus

$$\triangle P = \rho.c.[\dot{\phi}_0\cos(\omega t - kz)].$$

As we knew that the equation inside square bracket is simply particle velocity u, thus acoustic impedance can be obtained by dividing excessive pressure by particle velocity and can be expressed as the equation below.

$$Z = \frac{\triangle P}{u} = \rho.c \tag{2.65}$$

2.6   Attenuation

Two main elements contribute to ultrasound attenuation: absorption and scattering. Flashback to the previous matter, a non-attenuated plane harmonic wave of frequency υ propagating in a homogeneous medium along the positive *x*-axis as stated in Eq. 2.13. From the equation, it is known that frequency has an important role of wave. In such a case of imaging, high resolution of image may be obtained from high frequency. Lord Rayleigh stated, one spot of image might be well described as a circle with the diameter is equal to wavelength of the applied wave. Since the wavelength is inversely proportional to the frequency, thus the higher the frequency used in the system, the smaller the spatial pixel we obtained from the measurement.

Higher frequency provides a better resolution on the image. Nevertheless, it has an intrinsic high attenuation factor; therefore it can't be neglected in the numerical calculation.

In our system, ultrasound travels through three different mediums, two solids and liquid. Ultrasound energy will be dissipated, since intrinsically the medium absorbs its energy when it moves pass through liquids. The first theory relating to viscosity and attenuation was derived by Stokes [11]. He derived plane wave attenuation coefficient affected by shear viscosity only. When ultrasound pressure takes place, it may introduce small gradient of temperature and generate heat conduction and some amount compression. However, when the fluid's compressibility cannot be ignored, the volume viscosity coefficient must be considered into calculation. The equation below is the general form of attenuation, which takes into account shear viscosity (η), volume viscosity (η^v) and heat conduction (τ) [11, 62].

$$\beta\left[\frac{np}{cm}\right] = \frac{\omega^2}{2\rho c^3}\left[(\frac{4}{3}\eta + \eta^v) + \tau(\frac{1}{c_v} - \frac{1}{c_p})\right]$$

(2.66)

where β, ρ, ω, c are attenuation coefficient, density of the medium, angular frequency, and speed of sound in the medium, respectively. While specific heat at a constant volume and specific heat at a constant pressure are presented as c_v and c_p.

The attenuation coefficient of pure water and some other low viscous and low attenuation liquids may be expected has a linear function relationship to the frequency (υ) for homogeneous liquid.

$$\beta(\upsilon) = a + b.\upsilon$$

(2.67)

where a = -0.001119 and b = 0.001877 [11].

The intrinsic attenuation of pure water (β) is around 0.2 dB/ cm at 100 MHz. By extending the linear line of Eq. 2.67, attenuation coefficient of higher frequency can be achieved.

In the case of solid, attenuation is affected by many contributing factors. Each factor has their own

characteristic to contribute attenuation and occasionally they are also affected by the other factors. Therefore, accurate absolute attenuation values are never quoted and in the most cases the relative attenuation is measured as a function of some parameters, such as temperature, pressure or magnetic fields [2].

The polystyrene attenuation (γ) is in the range of 6 – 10 dB/cm at 10 MHz [63]. Other references also investigate ultrasound attenuation (dB/cm) in the polymer, especially for polystyrene by providing attenuation line as a function of frequency. The attenuation curve as described in Eq. 2.68 was obtained from several measurements of polystyrene and then compared to the ECAH model [9, 64].

$$\gamma(\upsilon) = 0.285\upsilon. \tag{2.68}$$

By extending the linear line of Eq. 2.68, attenuation coefficient of polystyrene for higher frequency can be achieved.

The attenuation coefficient of sapphire (dB/μs) as a function of frequency can be obtained from the curve provided in the ref [10]. It provides a wide frequenciec range, stretching from 200 – 10000 MHz, in which the frequency system in this research is laid.

2.7   Spatial Resolution
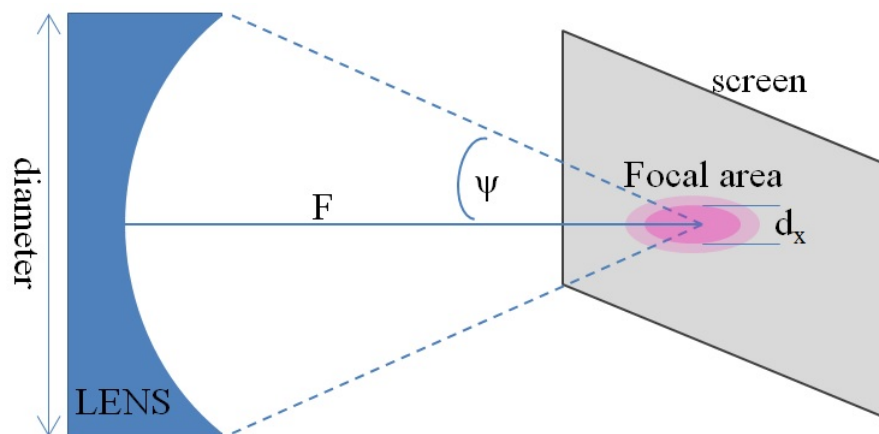
Figure 2.10: Description of focal area as a pixel in digital imaging.

In the acoustic microscopy, the quality of image is always a big issue. Poor image caused by low resolution may generate a bad analysis of observation. In order to improve the quality, it is always related to resolution. The term resolution is often used for a pixel count in digital imaging. Number of pixel in a certain area of image can be obtained from how many divisions of image areas are. To increase the number

of pixel in a certain length of image, thus the object should be divided into higher number of area. The more division will provide high resolution. It means that the division area become smaller.

If we bring the above analogy into acoustic microscopy system, the division area may be illustrated as a region taken from focal area. The focal area of the concave transducer will represent one pixel in a screen as show in Fig. 2.10. In some references [2, 65], the beam width of d_x is proportional to the wavelength by the relationship:

$$d_x = \lambda.F\sharp \qquad\qquad (2.69)$$

where $F\sharp$ is the ratio of the focal distance F to the diameter of lens.

Chapter 3

System Setup and Analysis

In this chapter we will review the system installed in this research. Three systems are developed in this thesis. First system is acoustic impedance microscope for tissue observation. The second and third systems are acoustic microscope used for cell observation. The first part of this chapter will be begun from the schematic of system, explanation of flow work and comparison between each system. The components which compose the system are also described in more detail. The last part are the analysis of system and speed of sound measurement.

3.1   System Layout and Explanation

A set of acoustic microscope system has been established to observe the target. The system consists of several components and will be described in this chapter. Figure 3.1 shows the established acoustic microscope in our laboratory.
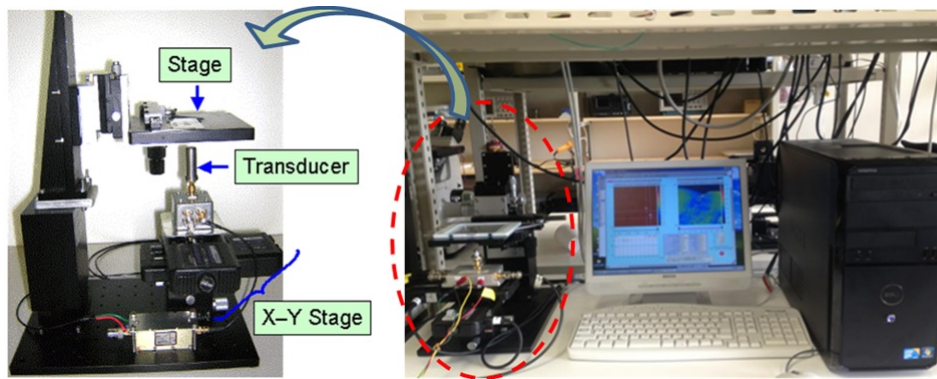
Figure 3.1: Acoustic microscope system in our laboratory.

In order to operate the acoustic microscope, a personal computer (PC) is needed as a place to embed control system and also stand as Human-Machine Interface (HMI) where user can give input variable and also to display the result of measurement. From PC, a control command is sent to the stage driver (Sigma KOKI, two axis stage controller, SHOT-202) trough GPIB (General Purpose Interface Bus) interface. The output of stage driver consists of two pulses, moving command pulse and trigger pulse. Moving command pulse is sent to x-y mechanical stage to perform x-y scanning mechanism. Trigger pulse is sent to pulsar

receiver to generate a very sharp electric pulse which is delivered to transducer (piezoelectric material). An acoustic wave is generated as a conversion result from sharp electric pulse by piezoelectric material. This acoustic wave is then transmitted toward the target, reflected back and received by the same transducer. The reflected acoustic wave is then converted back into analog electrical signal and sent to the PC via A/D board (Acqiris DP210 2GS/s 500MHz). The PC performs a computation to interpret signal from A/D board into acoustic intensity information. Figure 3.2 shows a layout of acoustic microscope system and typical of received acoustic signal.
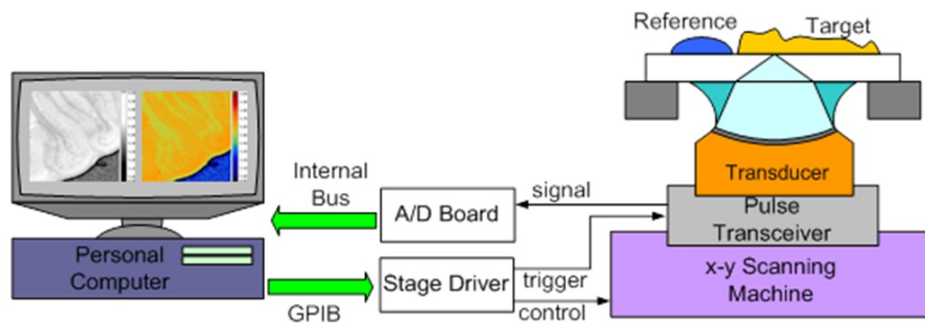
Figure 3.2: Layout of acoustic microscope system and typical of received acoustic signal.

The above explanation is used for tissue observation. In order to observe cell, we need to adjust the program as well as some equipment such as Sigma KOKI (SHOT-204MS) for stage driver and Agilen Acqiris U1065A (Model DC 222) for A/D Board. Table below shows the environment for tissue and cell observation.
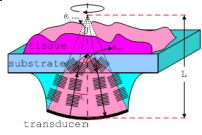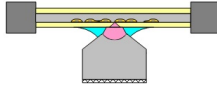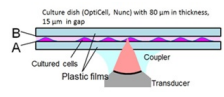
Description	Tissue Ac. Impd.	Cell Ac. Impd.	Internal Struc. of Cell
Frequency	30-100 MHz	200-400 MHz	200-400 MHz
Transd. type	Concave	Lens	Lens
Angle of Focusing	44°	120°	120°
Piezoelectric	PVDF-TrFe	ZnO	ZnO
Subs. Material	P.Styrene	P.Styrene	P.Styrene
Subs. Thickness	0.8 mm	0.08 mm	0.08 mm
Product Name	Nunc Delta Surface	Nunc Opticell	Nunc Opticell
Calc. Method	Fourier Analysis	Fourier Analysis	Refl Intensity
Struct. of target			

Table 3.1: The similarity and difference between three acoustic microscope.

The output of this acoustic microscope is 2D image of biological microscopy. The best image can be

obtained by placing the focal point onto the target. It can be obtained by moving position of the transducer up and down until the maximum reflection is received. This position is then maintained during the scanning process.

3.1.1 Transducer

In this thesis, two type of transducer are used, acoustic spherical and acoustic lens. Both transducers generate focused beam. The physical appearance look similar as it is shown in Fig. 3.3. However, the inside part of transducers (dashed circle) are different. Acoustic Spherical Transducer (AST) was built up from flexible piezoelectric material. It is shown in Fig. 3.3 (a), flexible piezoelectric material is pasted onto the prepared concave rod. For the practical measurement, we used this type of transducer, of which piezoelectric material is chosen from PVDF thin film [66]. In addition, PVDF is also has low intrinsic insertion loss as it is well matched to the water and biological tissue [2, 65]. Transducer made with material are typically very wide-band. However, due to its low electromechanical coupling coefficient, PVDF is not an ideal transmitting material. PVDF transducers are commercially available with operating frequency up to 100 MHz. The concave has a radius of 3.2 mm and 2.4 mm of its aperture. In this type of transducer, concave rod has no function, except to sustain the shape of piezoelectric.
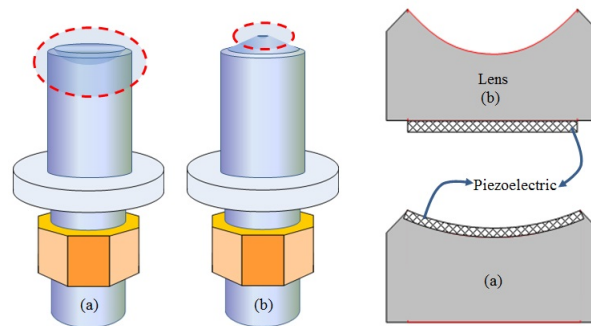
Figure 3.3: The transducer. (a) Concave piezoelectric transducer. (b) Flat piezoelectric transducer with concave lens.

The second type of transducer as shown in Fig. 3.3 (b) is made from flat ZnO piezoelectric material, and attached to concave sapphire rod [67]. As the demand needs high resolution image, high frequency of ultrasound must be applied. However, high frequency will affect small amount of received signal. When received signal intensity is getting smaller, it will affect the quality of image. One way to overcome this situation is shortening the path of the beam. It can be realized by constricting the radius of curvature rod. Since it is not easy to paste piezoelectric material onto it, another method was employed, i.e., put concave rod into function as lens and paste the piezoelectric material onto its bottom part. This kind of transducer is called Acoustic Lens Transducer (ALT) with curvature shape of lens was provided. In addition, spherical aberration

can be reduced if material of lens is chosen so that the ratio between speed of sound in the medium and lens is small. ZnO possess large electromechanical coupling coefficient. It was also found that ZnO material is suitable for more than 100 MHz transducer [2, 65]. When an electric pulse is transmitted, piezoelectric material convert into mechanical pulse. Plane wave is generated from the bottom side of the lens, propagate to the upper side. Concave shape will bend the direction of plane wave and focused the wave at focal point. The concave shape of sapphire has a radius of 0.25 mm and 0.25 mm of its aperture.

3.1.2 Substrate

In order to determine the material for substrate, we may choose several polymers which are available in the market. However, it is not easy to determine the appropriate material and thickness of substrate. In order to maintain the target from vibration during scanning process, substrate should has adequate thick to withstand the load thereon. Conversely, substrate should has adequate thin to reduce attenuation. Substrate thickness should consider these two parameters, frequency and the system.

Regarding the material for substrate, it should has impedance matching to pure water and tissue. If impedance is too high, then, most of acoustic wave will be reflected and only small portion will reach the target. If impedance is close to pure water or tissue impedance, then most of acoustic wave will be transmitted, and only small portion will be received by transducer. Polymethylmethacrylate (PMMA) and Polystyrene (PS) are available in the market and have a good number of impedance. In this study, we chose PS, due to the acoustic impedance of PS is much lower than PMMA. In addition to acoustic impedance, special treatment PS has a good hydrophilic for substrate-tissue adhesion.

Figure 3.4: Polystyrene dish that is used in this research.

Two type of substrate are used as shown in Fig. 3.4. The first is Nunclon$^T M$ delta surface. It has a polystyrene substrate with 0.8 mm in thickness and used to mount a target. This substrate plate is also provided by a cap, in order to decrease evaporation of the target. The second substrate is Nunc Opticell. It consists of two parallel gas-permeable, cell culture treated polystyrene membranes 75 μm thick and 2 mm

apart. Each side has a growth area of 50 cm^2, total 100 cm^2. Access to the cells is via two resealing ports providing a closed growth environment with sterile fluid path, minimizing the risk of contamination [68].

Some information regarding acoustic and mechanical properties of polystyrene were obtained from some references. Density of polystyrene is covering from 1040 – 1090 kg/m^3 [70]. Other references say that polystyrene density is 1040 – 1050 kg/m^3 [71, 72]. While the speed of acoustic inside the polystyrene is covering from 2320 – 2450 m/s and acoustic impedance is 2.42 – 2.55 MNs/m^3 [72]. In the numerical calculation we have decided to utilize 2340 m/s for the speed of acoustic inside polystyrene, with the density of 1051 kg/m^3.

3.1.3 Properties of Water

An important issue regarding ultrasonic transducers is the need for impedance matching. Biological tissue is placed on the polystyrene substrate. If air is utilized as a coupling medium, it will be a big difference of impedance between air and substrate. A major part of the acoustic beam will be reflected on this interface, and only a small part of the beam is transmitted toward the target. It causes the low quality of the image, since only small reflection intensity that is received by the transducer. Utilizing liquid will help to improve impedance matching between liquid and substrate.
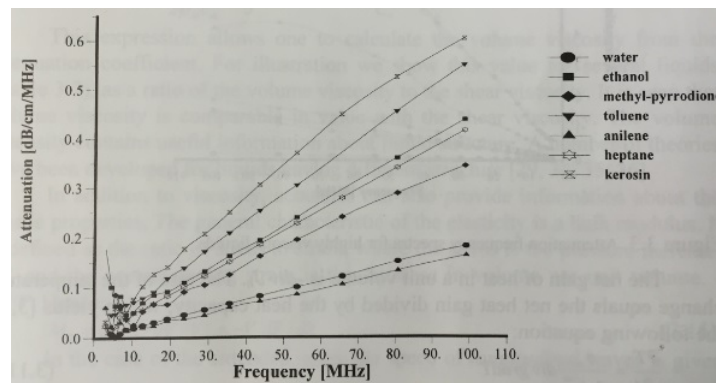
Figure 3.5: Attenuation frequency spectra for liquids with low viscosity.

In this thesis, pure water is used as a coupling material to couple the transducer and substrate. Since pure water has much higher acoustic impedance than air, utilizing pure water as a coupling material will raise impedance matching up. Water also has low attenuation coefficient, appropriate mass density and appropriate other physical properties compared to the other low viscosity liquid [11] as shown in the Fig. 3.5 and Table 3.2. Furthermore, water is a non-dispersive medium, so that all frequency component of the pulse are propagate with the same velocity [69].

40

Note	Sound Speed m/s	Attenuation [100MHz] dB/cm/MHz	tempera ture ^{o}C	density [g/cm^3]	compressibility [10^{-10}m^2/N^1]
water	1498	0.18	25	0.997	4.47
HCl	1509	0.18	25.3		
KCl	1547	0.18	23.7	1.04	4.02
LiCl	1552	0.18	25.4	1.02	4.07
NaCl	1559	0.18	25.6	1.04	3.96
CaCl$_2$	1572	0.18	25.8	1.06	3.82
CuSO$_4$	1555	0.94	25.8	1.13	3.66
MgSO$_4$	1623	0.63	26.6	1.1	3.45
MnSO$_4$	1593	0.69	25.7	1.12	3.52
AlCl$_3$	1640	0.22	23.9	1.08	3.44
Al$_2$(SO$_4$)$_3$	1634	1.28	26.1	1.13	3.31

Table 3.2: Water physical properties compared to the other solutions[11].

3.2 Echo Measurement

In this manuscript, reflection mode of scanning acoustic microscope is discussed. Ultrasonic beam will be transmitted through several layers, i. e. water, substrate and the target.
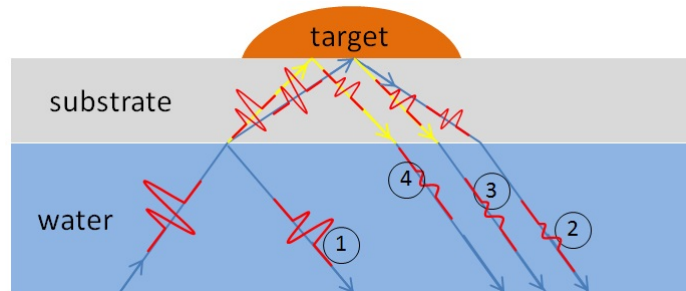
Figure 3.6: Description of propagation wave inside each layer. Blue and yellow arrows show propagation of pressure and shear waves respectively.

When ultrasound beam is transmitted with a certain deflection angle, two types of waves, i. e. pressure and shear wave is generated. Since the shear wave inside water are close to zero, the existence of this wave is neglected in the water. Therefore, it is only pressure incidence wave is considered in coupling medium as shown in Fig. 3.6. When the incidence wave is impinging water-substrate interface, some parts are transmitted as pressure and shear wave and the other is reflected as marked by number 1 (wave-1). Inside polystyrene, there are three wave propagations, i. e. transmitted pressure-reflected pressure, transmitted pressure-reflected shear, and transmitted shear-reflected shear. These waves will be transmitted as pressure

waves inside the coupling medium and marked by number 2 (wave-2), 3 (wave-3) and 4 (wave-4). Figure 3.7 shows a reflection ultrasound waveform, reflected at water-substrate interface and substrate-target interface. Pressure wave usually has higher speed compared to the shear wave. Since the substrate has several tens order of the wavelength, wave-1 and wave-2 have an adequate distance for a certain period. By applying window function, either wave-1 or wave-2 can be analyzed independently without influence from the other wave.
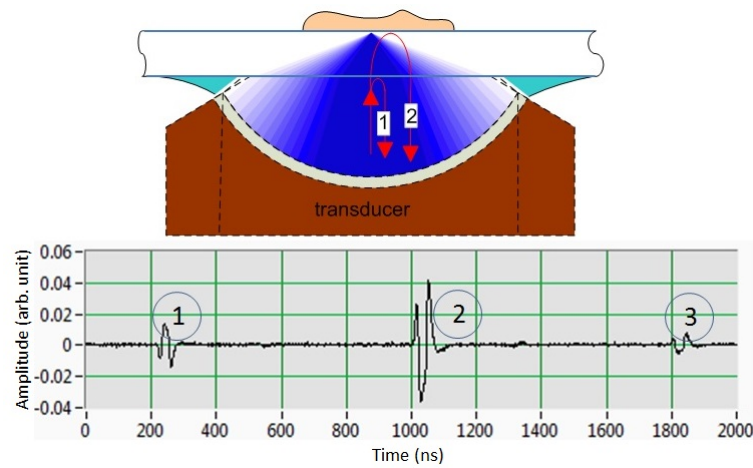
Figure 3.7: Reflected ultrasound wave from the interface between water-substrate and substrate-target.

3.3   Transducer Analysis

3.3.1   Sound Field Analysis

Two transducers, which are used in this thesis, have a concave shape. The contour of the shape will influence the distribution of sound potential generated by the transducer. In order to calculate sound potential at a certain probe point in front of the transducer, the sound source magnitude and the length of probe point to the source must be known. Since the transducer has a concave shape, the distance at the concave surface will have a variation length to the probe point. Therefore, it needs to divide the concave shape into several small areas. The smaller the area, the shape will be closer to the plane rather than concave, and the calculation result will be more accurate.

Figure 3.8 shows a small fragment at surface of the concave shape. From that figure, area of the small fragment *ABCD* can be calculated. Let's assume the angle of ∠*FOZ* is dψ and ∠*AEB* is dφ. If the fragment is very small, then we may assume as a small plane (rectangular), with a certain length to the probe point. Now the total area of small fragment *ABCD* is multiplication of *AD* and *AB*.

$AD = L.\mathrm{d}\psi$

$AB = L\sin\psi.\mathrm{d}\varphi$, thus area of the fragment is

$\mathrm{d}A_{ABCD} = AD.AB$,

$$\mathrm{d}A_{ABCD} = L^2.\mathrm{d}\psi.\sin\psi.\mathrm{d}\varphi \qquad (3.1)$$
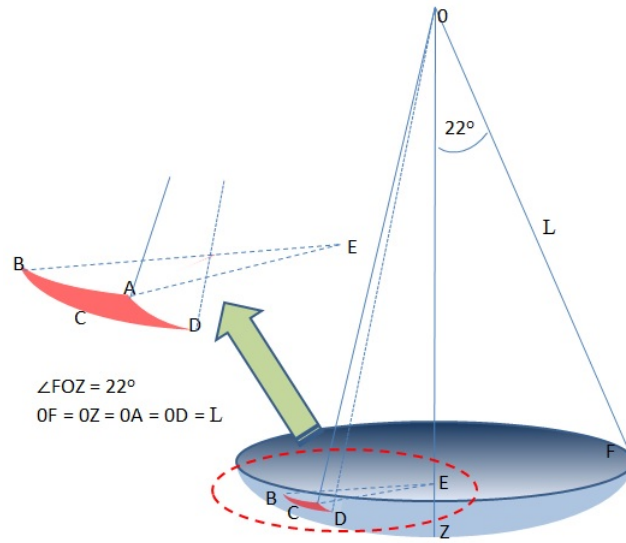
Figure 3.8: Small fragment source at the concave shape of the transducer.

Equation 2.61 has explained how to calculate sound potential caused from a small vibrating source. Utilizing this equation, then we can express the sound potential at a probe point with a certain distance from the source, by substitute Eq. 3.1 into Eq. 2.61.

$$\phi = A \int_0^\varphi \int_0^\psi \frac{e^{-j.k.r}}{r} L^2.\mathrm{d}\psi.\sin\psi.\mathrm{d}\varphi \qquad (3.2)$$

$$\phi = A \frac{e^{-j.k.r}.L^2.\sin\psi}{r} \psi.\varphi \qquad (3.3)$$

Figure 3.9 shows an axial cross sectional of sound field distribution (left side) in front of the transducer shown in Fig. 3.8, with L = 3.2 mm, and aperture = 2.4 mm. In this calculation, we used 50 MHz ultrasound. The magnitude at the entire concave surface of the transducer is assuming to 1 and it has same phase angle. Two profile of sound field distribution is also shown (right side) at z = 2.5 mm and z = 3.2 mm. From the figure we can draw a conclusion that the biggest intensity of sound is located around the focal point.
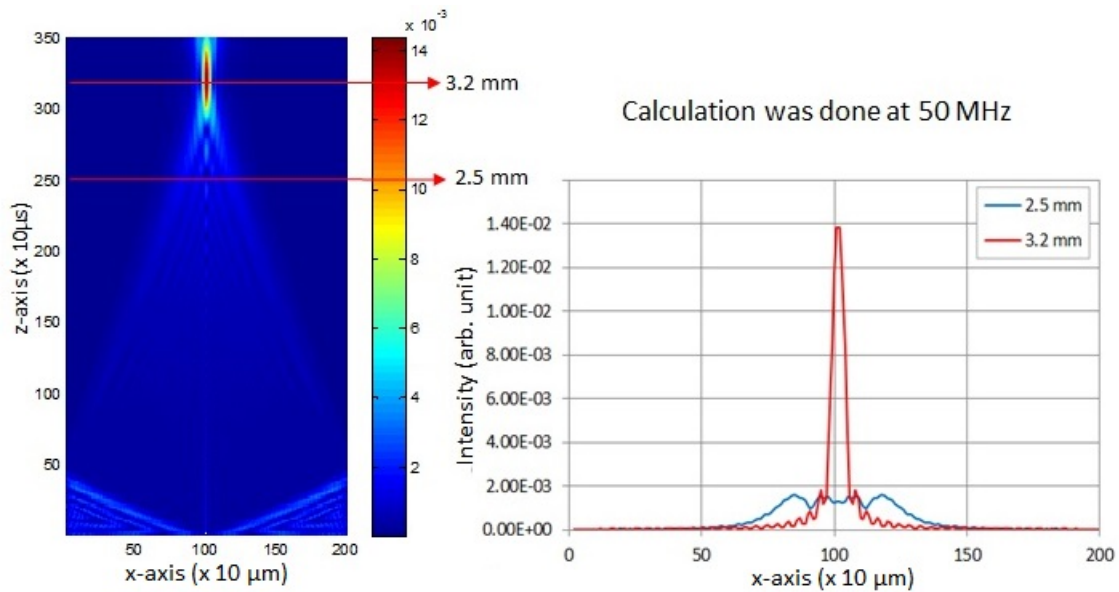
Figure 3.9: Result of sound field distribution calculation.

3.3.2 Resolution

The quality of image is strongly correlated to resolution. Figure 3.10 shows the resolution graph considering angle of focusing and frequency applied to the transducer. Group (i) are the graphs taken from the concave transducer without lens. Group (ii) are the graphs taken from the transducer with lens.
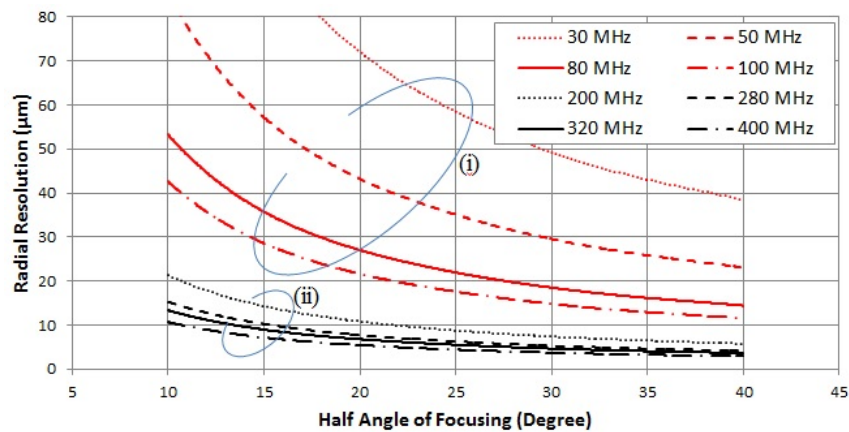
Figure 3.10: Spatial resolution based on angle of focusing and frequency.

3.4   *k*-space Analysis

As it has already explained in the previous chapter, in order to obtain sound potential distribution at a certain probe point at a certain z, we can take the advantage from calculation provided by Eq. 2.61. Moving the probe point to the x and y axes, thus we will obtained two dimensional (2D) profile of sound potential distribution. Afterwards, this profile is propagated along radial line to the z-axis direction. During propagation, this profile will meet an interface of two mediums with different physical properties. Since the transducer produced a focused ultrasound beam, thus, most of ultrasound component will form deflection angle to the interface line. Therefore, Snell's Law is needed to determine deflection angle (transmission angle) in the other side medium. However, it will be very difficult to determine transmission angle and magnitude from real space of above profile.

To solve the problem above, as an alternative is converting 2D profile from real space into *k*-space. As it has already known that *k*-space is derived from Fourier Transform, so in this material we also will discuss Fourier Transform. The term of k-space is taken from the letter "*k*", which has a meaning of wave number. In wave equation, wave number is wave quantity by unit length (in this research we applied meter). Wavelength is equivalent to the frequency, if domain reference is time.

$$k.x = 2.\pi.\upsilon$$

Afterwards, we can utilize Fourier Transform

$$F(\phi(z)) = \Phi(k_z) = \int_{-\infty}^{+\infty} \phi.e^{-j(k_z.z)}\mathrm{d}z, \tag{3.4}$$

for transferring real space into *k*-space, and

$$F^{-1}(\Phi(k_z)) = \phi(z) = \int_{-\infty}^{+\infty} \Phi(k_z).e^{j(z.k_z)}\mathrm{d}k_x z, \tag{3.5}$$

for transferring back *k*-space into real space.

We may say that the output of *k*-space is Fourier spectra or Frequency spectra or wave number spectra. There are several advantages offered by wave number spectra, i.e., the wave number and magnitude of each component can be known. This bring a possibility to know the deflection angle of each component as well.

3.5 Acoustic Impedance Derivation from Acoustic Intensity

It has been explained in the previous section, acoustic impedance is obtained from the multiplication of material density and sound speed. Most of the researchers make use this formulation in order to calculate acoustic impedance of the material. They measured the density and the speed of sound in a certain material, and subsequently they can calculate acoustic impedance. In the case of 2D image, especially for microscopic image it is very difficult to determine the distribution of acoustic impedance of the target. Usually, they portray a 2D image of target as a distribution of speed of sound and attenuation data. For this purpose, the target must be sliced in a certain widths, in order to determine the speed of sound and attenuation inside the target.

Herewith, we propose a new technique to obtain 2D image of acoustic impedance microscopy derived from acoustic intensity reflected from target. For this purpose, we are going to explain as follow.

3.5.1 Acoustic Impedance from Vertical Incidence

Based on the its structure, transducer is categorized into three. They are flat, small angle of focused and large angle of focused transducers. As it is explained in the previous study [56, 57, 73], the analysis of small angle of focused transducer may be approached by flat transducer. In this case, ultrasound beam is assumed to be perpendicular transmission to the interface line of two different mediums. As an illustration of this situation, it is described in Fig. 3.11 below.

Two reflection signals are reflected from tissue and reference, produced from the same source. In order to perform quantitative observations; both of targets, tissue and reference material should be observed. These two materials may be observed in the same field of view; however, if this is impractical, they may be observed separately under the same conditions.

The reflection intensity of the wave that is perpendicular to the normal interface line can be obtained from a well-known formula, as:

$$S_{ref} = \frac{Z_{ref} - Z_{sub}}{Z_{ref} + Z_{sub}} S_0, \tag{3.6}$$

and

$$S_{tgt} = \frac{Z_{tgt} - Z_{sub}}{Z_{tgt} + Z_{sub}} S_0, \tag{3.7}$$

where S_0 is the transmitted sound, S_{tgt} is the reflection from the target, S_{ref} is the reflection from the reference, and Z_{tgt}, Z_{ref} and Z_{sub} are the acoustic impedances of the target, reference and substrate,
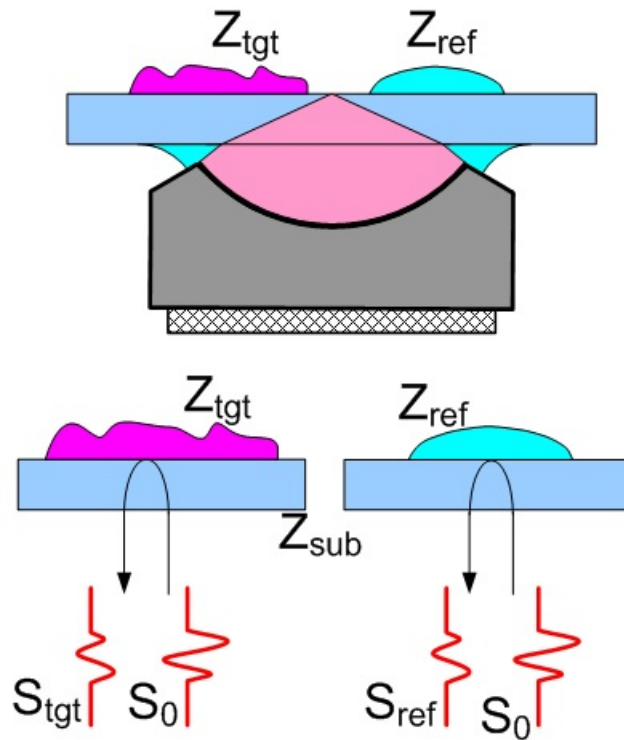
Figure 3.11: Illustration of small angle of focused transducer is approached as a vertical incidence analysis.

respectively. Substituting eq. 3.6 into eq. 3.7, the acoustic impedance of the target can be calculated as shown in eq. 3.8.

$$Z_{tgt} = \frac{1 - \frac{S_{tgt}}{S_{ref}} \cdot \frac{Z_{sub} - Z_{ref}}{Z_{sub} + Z_{ref}}}{1 + \frac{S_{tgt}}{S_{ref}} \cdot \frac{Z_{sub} - Z_{ref}}{Z_{sub} + Z_{ref}}} Z_{sub}. \tag{3.8}$$

By utilizing the equation above, acoustic impedance of target which is being observed under vertical incidence can be calculated. Application of this formula for small angle of focused transducer will generate error, however, it can be neglected, because the error is too small.

3.5.2 Oblique Incidence

In a practical measurement, large angle of focused transducer is used, replacing small angle of focused transducer. A large focused transducer is preferable to improve image quality and provides higher intensities, as well as image resolution. Because the ultrasound wave is focused, utilizing vertical analysis into this system is predicted to generate a significant error. Therefore, oblique incidence is considered in the calculation. In the chapter 4, there will be an especial discussion of comparing this two method and verification with the

measurement of several saline solution.

The transducer, which has a concave shape transmits spherical ultrasound wave that is composed of oblique incidence. To simplify the analysis, we utilize plane wave analysis instead of the spherical wave. Fourier analysis will be suitable because the sound field can be decomposed into many plane waves with different propagation angles. It has already described in the previous section (Chapter 2) that the magnitude of reflection and transmission parts from oblique incidence can be achieved, depending on the material of medium and angle of the incident wave. Referring this explanation we can solve the problem of oblique incidence regarding its angle and magnitude.

3.5.3 Plane wave

In order to approximate best result of calculation to concave shape of transducer, the shape must be divided into several parts. Each part will transmit ultrasound wave, from which we may calculate sound field distribution. The more division created in the concave shape, the more accurate the approximation to obtain sound field distribution. In order to calculate sound field at a certain probe point, we may refer to Eq. 3.2. By doing the same manner, 2D of sound field distribution in real space can be achieved. By converting this achievement into *k*-space, we can get the information of plane wave, regarding its magnitude, propagation angle and wave number.

3.5.4 Acoustic Impedance from Oblique Incidence

After the plane wave with a certain deflection of incident angle to interface of two different medium was known, we may obtain the intensity of either reflection or transmission wave. From this calculation we would like to establish a curve for converting acoustic intensity into acoustic impedance. By providing various of assumed target, i.e., saline solution of which acoustic impedance were known, reflection acoustic intensity can be calculated. The curve is established based on the value of acoustic intensity and acoustic impedance. Figure 3.12 shows the illustration of our proposal in this research.

3.6 Speed of Sound in Saline Solution

In this thesis, one part that is very essential is to describe the speed of sound rigorously. The accurate measurement of speed of sound is needed to yield the accuracy of acoustic impedance of target. In order to achieve that purpose, measurement of speed of sound inside of various saline solutions are done and compared to the famous formula by other researchers. In liquid, sound consists of compression waves only. The speed of a compression wave is determined by the medium's compressibility and density. Here, we
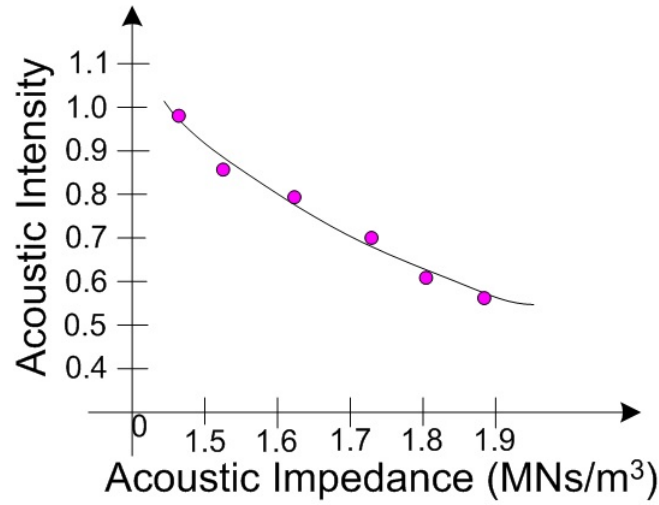
Figure 3.12: Illustration of calibration curve to convert acoustic intensity into acoustic impedance.

will describe two famous formulas used by UNESCO, *i.e.*, Del Grosso and Chen-Millero. Three parameters, salinity, temperature and pressure are considered into the calculation.

3.6.1 UNESCO Formula: Chen and Millero

Chen and Millero formula [74] is described as

$$c(S, T_t, P) = Cw(T_t, P) + A(T_t, P)S + B(T_t, P)S^{3/2} + D(T_t, P)S^2 \tag{3.9}$$

where,

$$\begin{aligned}
Cw(T_t, P) =& (C_{00} + C_{01}T_t + C_{02}T_t^2 + C_{03}T_t^3 + C_{04}T_t^4 + C_{05}T_t^5) + \\
& (C_{10} + C_{11}T_t + C_{12}T_t^2 + C_{13}T_t^3 + C_{14}T_t^4)P + \\
& (C_{20} + C_{21}T_t + C_{22}T_t^2 + C_{23}T_t^3 + C_{24}T_t^4)P^2 + \\
& (C_{30} + C_{31}T_t + C_{32}T_t^2)P^3
\end{aligned}$$

$$\begin{aligned}
A(T_t, P) =& (A_{00} + A_{01}T_t + A_{02}T_t^2 + A_{03}T_t^3 + A_{04}T_t^4) + \\
& (A_{10} + A_{11}T_t + A_{12}T_t^2 + A_{13}T_t^3 + A_{14}T_t^4)P + \\
& (A_{20} + A_{21}T_t + A_{22}T_t^2 + A_{23}T_t^3)P^2 + \\
& (A_{30} + A_{31}T_t + A_{32}T_t^2)P^3
\end{aligned}$$

$$B(T_t, P) = B_{00} + B_{01}T_t + (B_{10} + B_{11}T_t)P$$

$$D(T_t, P) = D_{00} + D_{10}P$$

T_t = temperature in degrees Celsius

S = salinity in Practical Salinity Units (parts per thousand)

P = pressure in bar

3.6.2   UNESCO Formula: Del Grosso

Del Grosso formula [74] is described as

$$c(S, T_t, P) = C_{000} + \triangle\, C_{T_t} + \triangle\, C_S + \triangle\, C_P + \triangle\, C_{ST_tP} \tag{3.10}$$

where,

$$\triangle\, C_{T_t}(T_t) = C_{T1}T_t + C_{T2}T_t^2 + C_{T3}T_t^3$$

$$\triangle\, C_S(S) = C_{S1}S + C_{S2}S^2$$

$$\triangle\, C_P(P) = C_{P1}P + C_{P2}P^2 + C_{P3}P^3$$

$$\triangle\, C_{S,T_t,P}(S, T_t, P) = C_{TP}T_tP + C_{T3P}T_t^3P + C_{TP2}T_tP^2 + C_{T2P2}T_t^2P^2 +$$
$$C_{T_tP3}T_tP^3 + C_{ST}ST_t + C_{ST2}ST_t^2 + C_{STP}ST_tP +$$
$$C_{S2TP}S^2T_tP + C_{S2P2}S^2P^2$$

T_t = temperature in degrees Celsius

S = salinity in Practical Salinity Units

P = pressure in kg/cm^2

Coefficients	Numerical Value	Coefficients	Numerical Value
C_{00}	1402.388	A_{02}	7.166E-5
C_{01}	5.03830	A_{03}	2.008E-6
C_{02}	-5.81090E-2	A_{04}	-3.21E-8
C_{03}	3.3432E-4	A_{10}	9.4742E-5
C_{04}	-1.47797E-6	A_{11}	-1.2583E-5
C_{05}	3.1419E-9	A_{12}	-6.4928E-8
C_{10}	0.153563	A_{13}	1.0515E-8
C_{11}	6.8999E-4	A_{14}	-2.0142E-10
C_{12}	-8.1829E-6	A_{20}	-3.9064E-7
C_{13}	1.3632E-7	A_{21}	9.1061E-9
C_{14}	-6.1260E-10	A_{22}	-1.6009E-10
C_{20}	3.1260E-5	A_{23}	7.994E-12
C_{21}	-1.7111E-6	A_{30}	1.100E-10
C_{22}	2.5986E-8	A_{31}	6.651E-12
C_{23}	-2.5353E-8	A_{32}	-3.391E-13
C_{24}	1.0415E-12	B_{00}	-1.922E-2
C_{30}	-9.7729E-9	B_{01}	-4.42E-5
C_{31}	3.8513E-10	B_{10}	7.3637E-5
C_{32}	-2.3654E-12	B_{11}	1.7950E-7
A_{14}	1.389	D_{00}	1.717E-3
A_{14}	-1.262E-2	D_{10}	-7.9836E-6

Table 3.3: Coefficients of Chen and Millero formula.

Coefficients	Numerical Value	Coefficients	Numerical Value
C_{000}	1402.392	C_{TP}	0.6353509E-2
C_{T1}	0.5012285E1	C_{T2P2}	0.2656174E-7
C_{T2}	-0.551184E-1	C_{TP2}	-0.1593895E-5
C_{T3}	0.221649E-3	C_{TP3}	0.5222483E-9
C_{S1}	0.1329530E1	C_{T3P}	-0.4383615E-6
C_{S2}	0.1288598E-3	C_{S2P2}	-0.1616745E-8
C_{P1}	0.1560592	C_{ST2}	0.9688441E-4
C_{P2}	0.2449993E-4	C_{S2TP}	0.4857614E-5
C_{P3}	-0.8833959E-8	C_{STP}	-0.3406824E-3
C_{ST}	-0.1275936E-1		

Table 3.4: Coefficients of Dell Grosso formula.

Chapter 4

Acoustic Impedance Microscope for Soft Biological Tissue

4.1 Brief Description

This chapter proposes a new method for microscopic acoustic imaging that utilizes the cross sectional acoustic impedance of biological soft tissues. In the system, a focused acoustic beam with a wide band frequency of 30 - 100 MHz is transmitted across a plastic substrate on the rear side of which a soft tissue object is placed. By scanning the focal point along the surface, a 2-D reflection intensity profile is obtained. In this chapter, interpretation of the signal intensity into a characteristic acoustic impedance is discussed. Because the acoustic beam is strongly focused, interpretation assuming vertical incidence may lead to significant error. To determine an accurate calibration curve, a numerical sound field analysis was performed. In these calculations, the reflection intensity from a target with an assumed acoustic impedance was compared with that from water, which was used as a reference material. The calibration curve was determined by changing the assumed acoustic impedance of the target material. The calibration curve was verified experimentally using saline solution, of which the acoustic impedance was known, as the target material. Finally, the cerebellar tissue of a rat was observed to create an acoustic impedance micro profile. More details of the numerical analysis and verification of the observation results will be described here.

4.2 Background

Optical microscopy is often used to observe biological soft tissues. One of its advantages is that it provides very high spatial resolution; however, it requires a staining process to retrieve good contrast in the resulting images. This process may take several days for observation or at least several tens of minutes for a rapid observation. Conversely, in some instances, observations using ultrasound may be a powerful measure because no staining process would be required, potentially leading to a rapid and potentially accurate observation. In ultrasonic observations, the image contrast is determined by acoustic properties such as the speed of sound and attenuation, which are reflected by visco-elastic properties.

Most acoustic microscopes are of the scanning type (SAM). SAM was developed by Quate and Lemons in 1974 with a focused ultrasonic beam formed by an acoustic lens [42]. Thanks to the development of

piezoelectric copolymer films, a concave-type transducer has become available recently with a lower cost if the frequency range is as low as 100 MHz [3]. Utilization of SAM for the visualization of cells or target has been performed. The results were visualized into 2D images based on intensity, the speed of sound, attenuation and thickness [50–54]. In most SAMs for biological and medical use, a tissue slice or cells are placed on a flat substrate, and the local speed of sound can be estimated by comparing two reflections from the top and bottom surfaces. To acquire the response, focused ultrasound is transmitted across the coupling medium between the transducer and target. Because this measurement requires a thin slice of biological material, it requires a specific device for slicing the tissue. Alternatively, if the target is cultured cells, contact between the cells and transducer through a coupling media may introduce contaminants into the target.

As one of solutions to the above-mentioned problems, several researchers proposed acoustic impedance microscopy [56–58, 73]. In those previous studies, the acoustic wave at the focal point was approximated to be a plane wave propagating vertically to the target. It is assumed that the above calculation may generate error when a highly focused transducer is used. In such a case, calibration should be performed based on the results of an accurate sound field analysis.

In another previous paper [3], different angles of propagation of many beams were considered; however, frequency components were not considered. Several numerical calculations of the sound field were performed for a certain application using a finite differential time domain (FDTD) [75–77]. Several authors also developed and improved numerical calculations based on a Fourier Transform of the so-called Angular Spectrum Method for Non-Destructive Test (NDT); this method is used to investigate the presence of a plane interface [78, 79]. In a recent report, this technique is also used to solve the calculation for linear and non-linear pulsed sound fields [80, 81]. A similar concept that uses the reflection coefficient method for predicting mass density was presented by Saito [82]. Fourier analysis has also been applied to calculate acoustic propagation in multilayer media by Tittmann et al. [83]; because they used an acoustic lens transducer for their measurements, the pupil function of the lens is considered.

Here, we applied Fourier analysis to calculate the sound field. When an oblique incident occurs, information regarding the angle of propagation and wave number are required.

In this chapter, the outline of acoustic impedance microscopy and its sound propagation analysis using Fourier transform and the curve for converting reflection intensity into acoustic impedance will be described. In addition, for example, the observation and analysis results using the cerebellar tissue of a rat will be exhibited.

4.3 System Setup

Figure 3.2 shows the block diagram system for an acoustic impedance microscope [3, 15]. A PVDF-TrFE concave type transducer with an aperture with a 2.4-mm diameter and a focal length of 3.2 mm was

used. Its half angle of focusing was 22 degrees. As a coupling medium, pure water was chosen and had a pressure wave speed of 1480 m/s at 20 ^{o}C. A polystyrene substrate (Nunc # 150318 Petri-dish, speed of sound = 2340 m/s) with a thickness of 0.8 mm was used to mount a target, and the substrate was coupled with the transducer through the coupling medium. A stage driver sent a control command to the x-y scanning machine and sent a trigger to the pulse transceiver to generate a short electric pulse that was applied to the transducer and converted into an ultrasound wave. A focused ultrasound beam with a frequency between 30 and 100 MHz as shown in the Fig. 4.1 was transmitted from the front side of the substrate, the rear side of which was in contact with the target. The ultrasound propagated through the coupling medium and substrate, reflected at the interface between the substrate and target and then finally returned to the same transducer. The reflection intensity from the interface between the substrate and target, on which the beam is focused, was acquired and interpreted into the absolute value of the characteristic acoustic impedance of the target. During measurement, the room temperature was maintained by an air conditioner at 20-21 ^{o}C. Measurements were performed under ambient pressure, but the pressure was not controlled.
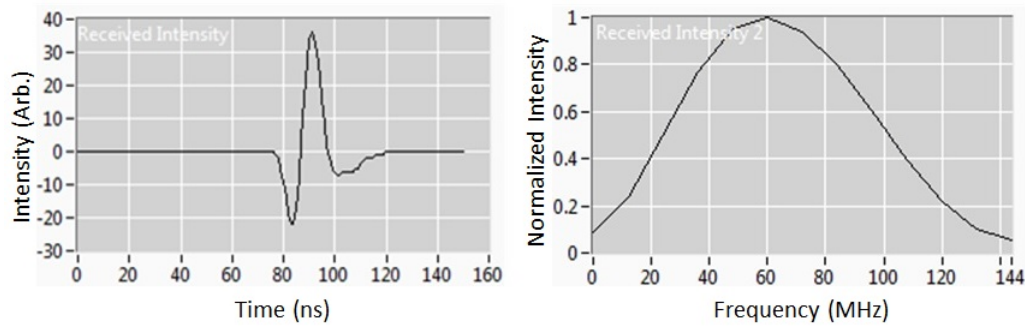
Figure 4.1: Typical acoustic waveform reflected from the target and its frequency spectra.

4.4 Methodology and Analysis

4.4.1 Focused Beam with Oblique Incidences

In a practical measurement, a focused transducer is preferable to improve image quality; a focused transducer provides higher intensities as well as image resolution. Because the beam is focused, oblique incidence calculation is performed, particularly when the focusing angle is large. In such a case, Fourier analysis will be suitable because the sound field can be decomposed into many plane waves with different propagation angles. If the beam is decomposed into plane waves, the transmission and reflection ratio on the interface can be calculated by considering the boundary condition across the interface between the different media. Figure 4.2 shows the concept of plane wave propagation. The calculation can thus be performed in the order of i) sound field analysis without a substrate, ii) transmission of each plane wave into the substrate

from the coupling medium, iii) reflection from the target, iv) transmission from the substrate to the coupling medium and v) calculation of the transfer function of the system.
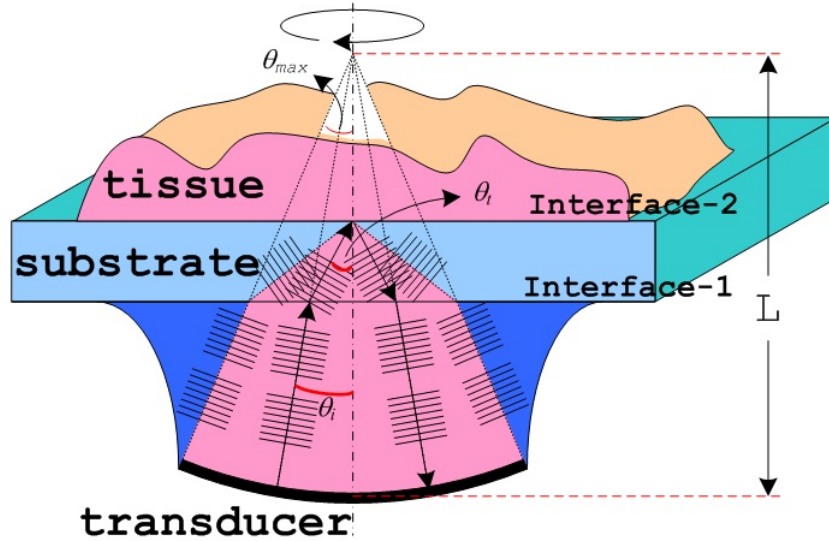
Figure 4.2: Plane wave analysis for a focused acoustic beam.

4.4.2 Sound Field without Substrate

A spherical transducer generates an acoustic wave with the same phase from any small fragment on the surface. This unattenuated wave is composed of several sinusoidal waves and can be described by Eq. 4.1:

$$\phi_0 = A_0 + \Sigma_{n=1}^{N} A_n . e^{-j(2\pi.f.t.n+\vartheta_n)} \tag{4.1}$$

where A_0 is the magnitude of the DC component, A_n is the magnitude of the sinusoidal components of the nth order, ϑ_n is the phase of the sinusoidal components of the nth order, and n is the harmonic order.

If the spherical transducer is placed in free space that is filled with a uniform coupling medium, as shown in Fig. 3.9, the sound field $\phi(x,y,z)$ (i.e., displacement potential) at a certain probe point produced by a small fragment of sound source da on the surface of the transducer can be represented as:

$$\phi(x,y,z) = \phi_0 . \frac{e^{-j(\boldsymbol{k}.\boldsymbol{l})}}{|\boldsymbol{l}|} da, \tag{4.2}$$

where,

ϕ = sound potential,

ϕ_0 = unattenuated potential at the surface of transducer,

l = distance between two points,

k = wave number,

da = small fragment (area).

In a similar manner, the potential distribution along a line that is perpendicular to the z-axis can be calculated and shown as Fig. 3.9 (right side). Because the geometry of the transducer is axis-symmetric, the 2D potential distribution on a certain plane can be obtained by rotating the above linear distribution. Figure 4.3 show sound field distribution in 1D and 2D, after rotation function is performed.
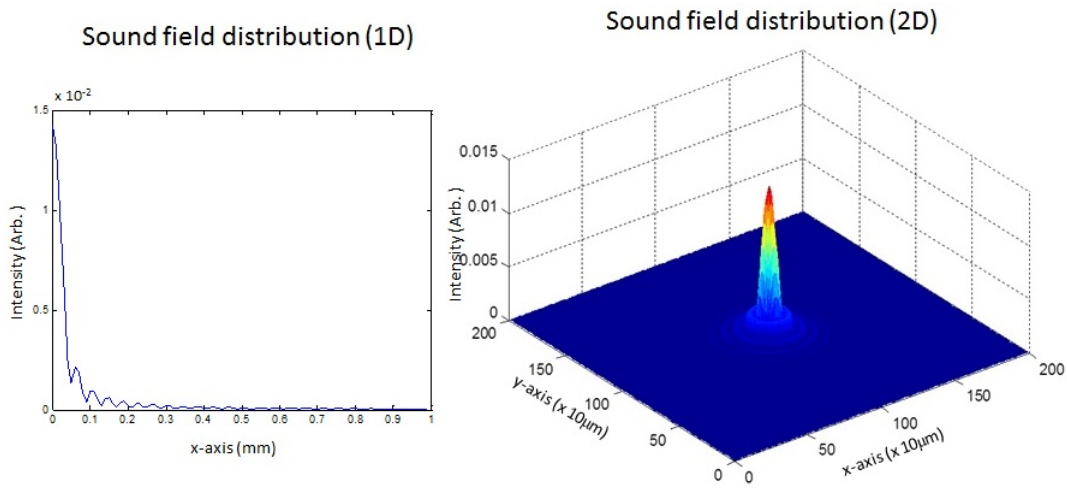
Figure 4.3: Sound field is calculated along one at a certain z. Performing rotation function, 2D of sound field distribution is achieved

4.4.3 Transmission and Reflection Ratio Based on Boundary Condition

When a substrate is inserted, a boundary plane will be established at the interface between the coupling medium and substrate. When a plane wave is emitted into the substrate, it will change the direction of propagation following Snell's law. Concurrently, the wave component in k-space will be modified due to the transmission or reflection ratio, depending on the incident angle:

$$\frac{c_1}{sin\,\theta_1} = \frac{c_2}{sin\,\theta_2}$$

where c_1, c_2 are the velocities of the incident and transmitted waves, respectively; and θ_1, θ_2 are the angles of the incident and transmitted waves, respectively.

Because a sound wave is composed of many plane waves with significant angles of propagation, an oblique incident analysis of the sound must be considered. As shown in Fig. 2.9, six types of waves should be considered: the incident pressure wave, the incident shear wave, the reflected pressure wave, the reflected shear wave, the transmitted pressure wave and the transmitted shear wave. The relation between these coefficient has been described in Eq. 2.59, as shown in the equation below.

$$\begin{pmatrix} k_{s1} & k_{p1} & k_{s2} & -k_{p2} \\ -k_{s1} & k_{p1} & k_{s2} & k_{p2} \\ \rho_1 & -\rho_1 & \rho_2 & \rho_2 \\ -\rho_1 & -\frac{G_1\rho_1}{E_1+2G_1} & \rho_2 & -\frac{G_2\rho_2}{E_2+2G_2} \end{pmatrix} \cdot \begin{pmatrix} \cos\theta_{sr} & \sin\theta_{pr} & \cos\theta_{st} & \sin\theta_{pt} \\ \sin\theta_{sr} & \cos\theta_{pr} & \sin\theta_{st} & \cos\theta_{pt} \\ \sin 2\theta_{sr} & \cos 2\theta_{sr} & \sin 2\theta_{st} & \cos 2\theta_{st} \\ \cos 2\theta_{sr} & \sin 2\theta_{pr} & \cos 2\theta_{st} & \sin 2\theta_{pt} \end{pmatrix}$$

$$\begin{pmatrix} A_{sr} \\ A_{pr} \\ A_{st} \\ A_{pt} \end{pmatrix} = \begin{pmatrix} k_{s1} & -k_{p1} \\ k_{s1} & k_{p1} \\ \rho_1 & \rho_1 \\ \rho_1 & -\frac{G_1\rho_1}{E_1+2G_1} \end{pmatrix} \cdot \begin{pmatrix} \cos\theta_{sr} & \sin\theta_{pr} \\ \sin\theta_{sr} & \cos\theta_{pr} \\ \sin 2\theta_{sr} & \cos 2\theta_{sr} \\ \cos 2\theta_{sr}) & \sin 2\theta_{pr} \end{pmatrix} \begin{pmatrix} A_{si} \\ A_{pi} \end{pmatrix}.$$

In the process of ultrasound propagation, two transmissions and one reflection occurs.

4.4.4 Received Intensity

When the 2D potential distribution of ultrasound is obtained in the coupling medium (see previous section), it moves into substrate. Because most beams have a deflection angle of propagation, transforming a 2D potential distribution into a 2D plane wave k-space is helpful because the angular component is easily determined. The expression of the 2D plane wave in k-space is found using a Fourier transform, as described in Eq. 4.3

$$\Phi(k_x, k_y) = F\{\phi(x,y)\} \int\int_{-\infty}^{+\infty} \phi(x,y).e^{-j(k_x.x+k_y.y)}\mathrm{d}x\mathrm{d}y, \tag{4.3}$$

where $\Phi(k_x, k_y)$ is the 2D potential distribution in k-space. The plane consists of sound potential information based on its corresponding wave number (k), as a function of k_x and k_y. Since we knew the wave number of corresponding sound potential, it will be easy to find the corresponding angle, as well as to determine the transmission and reflection ratio. Additionally, the k-space is helpful for calculating the propagation of the beam by performing shift Fourier transforms, as described in Eq. 4.4

$$\Phi(k_x,k_y)\mid_z = e^{-j.k_z.(z_r-z)}\Phi(k_x,k_y)\mid_{z_r}. \tag{4.4}$$

$$k_z = \sqrt{|\boldsymbol{k}_1|^2 - (k_x^2 + k_y^2)}. \tag{4.5}$$

$$|\boldsymbol{k}_1| = 2.\pi.f/c_1, \tag{4.6}$$

where k_x, k_y and k_z are wave numbers in terms of the x, y and z directions, respectively; f is the frequency; and c_1 is the speed of sound in the coupling medium. k_1 is the wave number in the coupling medium, and z_r is a position where the measured 2D plane wave $\Phi(k_x,k_y)$ is used as a reference.

The description below is an explanation to obtain the transfer function for one round trip of the ultrasound wave. Referring to Fig. 4.4, we consider several locations to calculate planes, including in the coupling medium, at interface-1 on the coupling medium side and the substrate side and at interface-2 on the substrate side.

From Eq. 4.3, we have Φ_a, which is a 2D plane wave distribution at a given location (Fig. 4.4) with several amplitudes, several wave numbers k_z and angles of propagation in the coupling medium. To calculate the plane wave in the substrate, the plane wave at interface-1 on the coupling medium side must be known. This distribution is then multiplied by the transmission ratio depending on the incident angle. The 2D plane wave distribution at interface-1 in the coupling medium side is determined by:

$$\Phi_b = \Phi_a.e^{-j(k_{z1}.l_1(z))}. \tag{4.7}$$

Thus, the plane wave distribution on the substrate side of interface-1 is:

$$\Phi_c = \Phi_b.A_{pt1}, \tag{4.8}$$

where A_{pt1} is the pressure wave transmission ratio of interface-1 from the coupling medium to the substrate, see Eq. 2.59. When the plane wave reaches the substrate, the wave number k_1 in the coupling medium is replaced by $k_2 = 2.\pi.f/c_2$, where c_2 is the speed of sound in the substrate. Consequently, the wave number k_z as stated in Eq. 4.5 will change. The expression of the plane wave on the substrate side of interface-2 can be written as:

$$\Phi_d = \Phi_c.e^{-j(k_{z2}.l_2(z))}. \tag{4.9}$$

Because the departure and return path of the plane wave are identical inside each medium, we can calculate

the received intensity at the transducer; however, the reflection ratio of interface-2 and the transmission ratio of interface-1 in terms of the return path must be considered. The transfer function of the received intensity by the transducer is described in Eq. 4.10

$$\frac{\Phi_h}{\Phi_a} = R.e^{-2j(k_{z1}.l_1(z) + k_{z2}.l_2(z))}. \tag{4.10}$$

where Φ_h/Φ_a is the transfer function of the received signal at the transducer, R is the total multiplication of the transmission and reflection ratio, and k_{z1} and k_{z2} are the wave numbers in terms of the z direction in the coupling medium and substrate, respectively. $l_1(z)$ and $l_2(z)$ are the length of propagation in the coupling medium and substrate, respectively.

The 2D plane wave in k-space on the surface of the transducer can then be defined as $\Phi_h(k_x, k_y)$. Then, the received intensity at the transducer can be obtained by performing an inverse Fourier transform, as described by eq. 4.11

$$\phi_h(x,y) = F^{-1}\{\Phi_h(k_x, k_y)\} = \int\int_{-\infty}^{+\infty} \Phi_h(k_x, k_y).e^{-j(k_x.x + k_y.y)}dk_x dk_y. \tag{4.11}$$

If the target material is approximated to be uniform in the region of the focal point, the normalized intensity can be represented as:

$$\frac{\phi_h(x,y)}{\phi_{h0}(x,y)}, \tag{4.12}$$

where $\phi_{h0}(x,y)$ corresponds to the signal from the reference material. All of these calculations are performed for one frequency component.

4.4.5 Acoustic Impedance of Saline Solution

The acoustic impedance of a material is defined as a product of the density ρ and the speed of sound c. The acoustic impedance of saline solution is used to verify the calibration curve from the numerical calculations, as shown in Eq. 2.65:

$$Z = \rho.c.$$

The densities of several saline solutions are taken from online [84]. To obtain the speed of sound, we performed measurement as shown in Fig. 4.5.
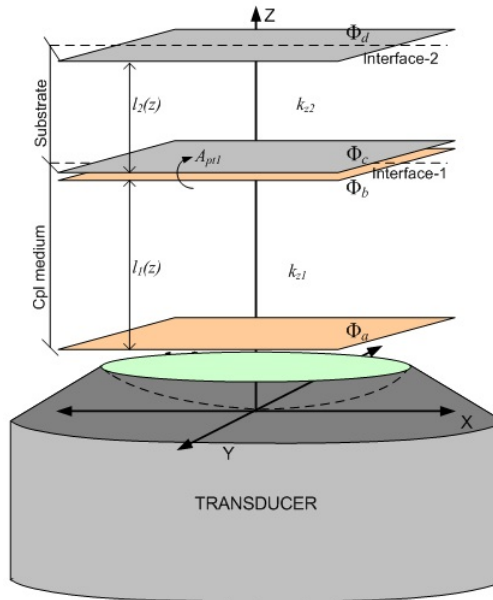
Figure 4.4: Potential distribution in k-space. The departure and return paths of the ultrasonic wave will have the same distance and wave number in each layer
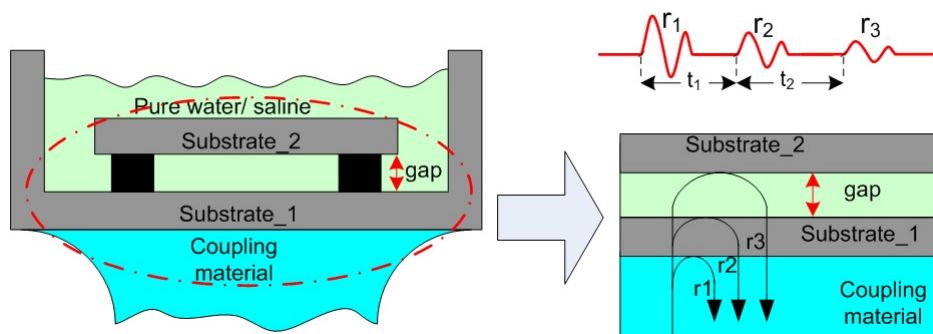
Figure 4.5: Measurement apparatus for measuring the speed of sound measurement in saline solution. The gap between two substrates is 0.85 mm (left side). Description of the reflected beam generated by each layer (right side)

Figure 4.5 left side is used instead of the target shown in Fig. 3.2 for measuring the speed of sound in saline solution. Using a flat transducer, an ultrasonic beam with a frequency between 30 and 100 MHz is transmitted from the bottom side, reaching Substrate_1, the gap and then Substrate_2. Three reflections, r_1, r_2 and r_3, are obtained and recorded by the PC. The time lag between reflections r_2 and r_3 (t_2) in Fig. 4.5 right side corresponds with double the thickness of the gap. The thickness of gap d can be determined by filling the gap with pure water, of which the speed of sound is known to be 1480 m/s at 20 ^{o}C. From this experiment, the gap d is 0.85 mm. When the thickness of the gap and t_2 are known, the speed of sound of the saline solutions can be easily obtained from eq. 4.13

$$c = 2d/t_2. \tag{4.13}$$

4.5 Result and Discussion

4.5.1 Sound Field Analysis

Figure 4.6 shows a typical sound field corresponding to the transducer used. Figure 4.6 (a) represents the sound field when the transducer is placed in water. When the substrate is present, the sound field is distorted, as shown by Fig. 4.6 (b). In this case, the position of the substrate was chosen so that the sound field intensity at the top of the substrate was maximized.

4.5.2 Acoustic Impedance of Saline solution

Several saline solutions with increments of 1% were prepared from 0% up to 10%. Speed of sound measurements were conducted as described in section 3.6. Results were then compared to the well-known formula, formulated by Del Grosso and Chen-Millero [74].

From the trend line equations and measurement results shown in Fig. 4.7, we determined that the measurements agreed with both formulae. Some of the differences shown may have been caused by different references of the speed of sound in pure water. Additionally, both the Del Grosso and Chen-Millero formulae are valid for densities equal to or lower than 4%.

Because there is little difference between the speed of sound graphs generated by the Del Grosso and Chen-Millero equations, we used Del Grosso' results for comparison with the measurements in this study. The density of the weight percentage (w %) of saline solutions are easily found online [84]. Using these data and the speed of sound generated from our measurements and the Del Grosso equation, we compared acoustic impedances, as shown in Table 4.1. Because no significant differences were found, we used acoustic impedance based on measurements for subsequent calculations.

61
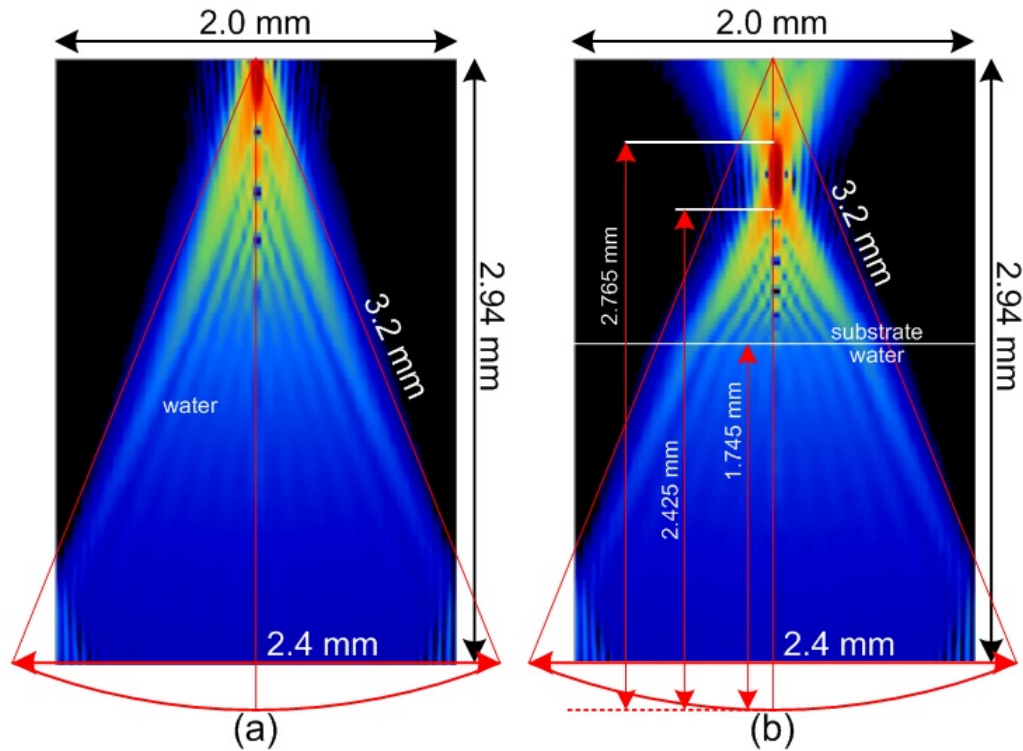
Figure 4.6: Ultrasonic propagation using the curved shape of the transducer in (a) pure water; and (b) pure water and polystyrene as a medium. Frequency: 80 MHz.
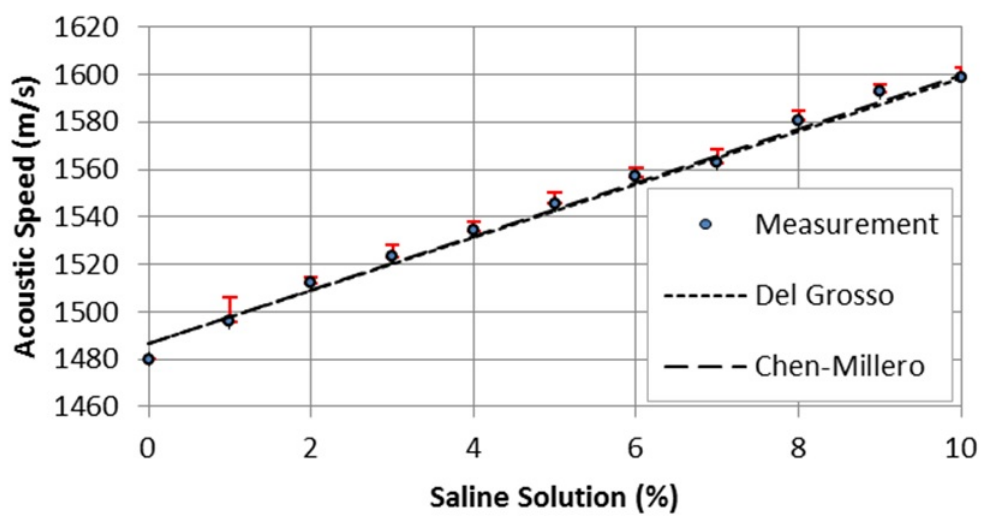
Figure 4.7: Speed of sound measurements with standard deviation error bars, compared to the Del Grosso and Chen-Millero equations.

| Salinity (w %) | Density (kg/m³) | Measurement | | Del-Grosso Eq. | | Perc. Err (%) |
		Speed (m/s)	Z (MNs/m³)	Speed (m/s)	Z (MNs/m³)	
0	1000	1480	1.48	1485.69	1.48569	0.383
1	1005.3	1495.857	1.503785	1496.683	1.50462	0.0552
2	1012.5	1512.058	1.530958	1507.722	1.52657	0.2876
4	1026.8	1534.212	1.575329	1529.942	1.57094	0.2791
6	1041.3	1557.026	1.621331	1552.349	1.61646	0.3013
8	1055.9	1580.528	1.66888	1574.943	1.66298	0.3546
10	1070.7	1598.626	1.711649	1597.725	1.71068	0.0564

Table 4.1: Acoustic impedance of saline solutions obtained by measurement, compared to the Del-Grosso Equation, shown in percentage error.

4.5.3 Received Ultrasound Intensity

Three media must be considered in terms of their structure: coupling water, substrate and target. Referring to Fig. 4.4, two interfaces are created: the interface between the coupling medium and substrate (interface-1) and the interface between the substrate and target (interface-2).

During its round trip through the media, the ultrasound wave passes through 3 interfaces, including transmission from water to the substrate, reflection from the substrate to the target and transmission from the substrate to water. The transmission and reflection ratios of each interface are determined as described in Eq. 2.59.

Once an oblique incident occurs, both pressure and shear waves are generated. Because many reflections with many different types of propagation paths exist, several opportunities to determine intensity may occur at the transducer (e.g., the pressure wave in the coupling medium, the shear wave in the substrate, the reflected shear wave in the substrate and the pressure wave in the coupling medium). In this paper, we need to describe the reflection as the result of only one type of propagation path (i.e., the pressure wave in the coupling medium, the pressure wave in the substrate, the reflected pressure wave in the substrate and the pressure wave in the coupling medium).

Because the pressure wave normally has a higher speed compared to that of the shear wave, these two waves can be separated after an appropriate time has passed, if the waveform is pulse-shaped and has a limited duration. After the pressure wave has been separated, a 2D potential distribution in real space can be calculated, as described in section 3.3. Using a Fourier transform, the 2D plane wave in k-space can be calculated. Referring to the explanation in section 3.5, the total received intensity at the transducer can be calculated by summing all components of the potential distribution in real space.

Figure 4.8 (a) shows the results of the numerical calculations for vertical and oblique incidents. The transmission and reflection ratios for calculating a vertical incident is accomplished with eq. 3.8; for an oblique incident, eq. 2.59 is used. In the curve, the mass density of the target is assumed to be 1000 kg/m³,
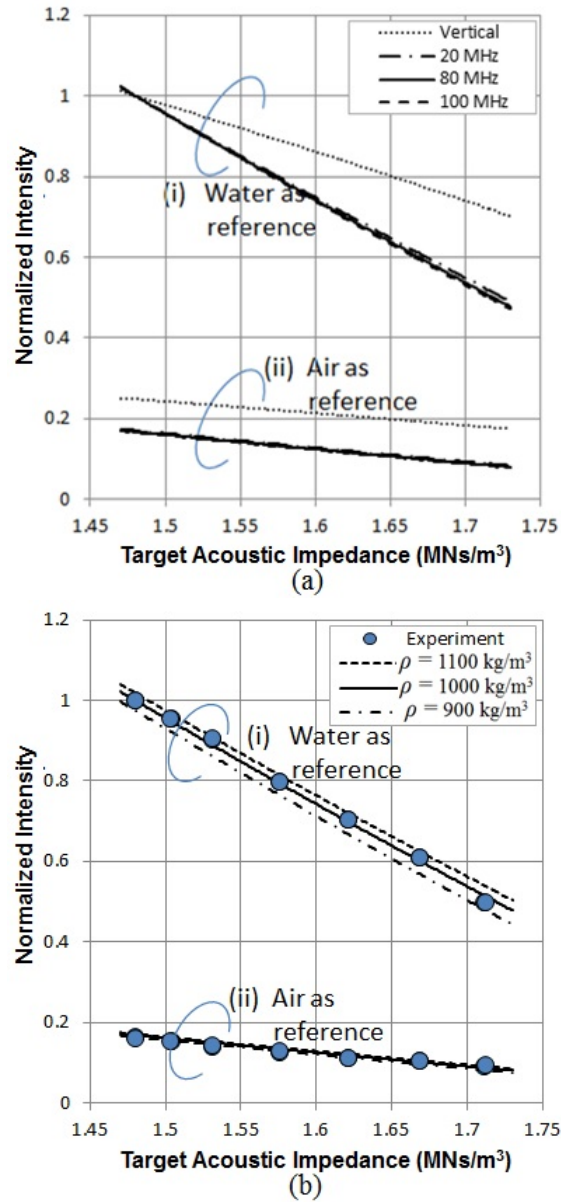
Figure 4.8: (a). Eight calibration curves based on numerical calculation. Round-dotted curves express vertical incident calculations, and dash-dot, solid and dashed curves express oblique incident calculations based at 30, 80 and 100 MHz, respectively. Calibration curves bundled in category (i) and category (ii) used pure water and air as reference materials, respectively. These calculations were performed by considering the density of 1000 kg/m^3. (b) Six calibration curves based on numerical calculation. Dashed, solid and dash-dot curves were calculated at 900, 1000 and 1100 kg/m^3, respectively. Calibration curves bundled in category (i) and category (ii) used pure water and air as reference materials, respectively. These calculations were performed at 80 MHz. Saline solution measurements (circles) are plotted on the same field and show good agreement.

which is a typical value of biological soft tissues. Category (i) represents the results when water is used as a reference material. Therefore, the normalized intensity is always 1.0 at 1.48 MNs/m^3, which is the acoustic impedance of water itself. There is no significant gap between the results when a vertical incident is assumed or when considering a focused sound field. However, the gap becomes larger as the acoustic impedance of the target increases, suggesting that the sound field should be considered in the calibration of acoustic impedance.

The bold dash-dot, solid and dashed curves represent the results at 30 MHz, 80 MHz and 100 MHz, respectively. Results for all frequencies between 30 MHz and 100 MHz are within the region of these curves. It is seen that frequency dependence is negligible.

Category (ii) represents the results using air as a reference material. Because the acoustic impedance of air is low, the normalized intensities can be as low as 0.2 even if the acoustic impedance of the target is the same as water. The gap between the results assuming a vertical incident and by considering a focused sound field is also large (e.g., 1.4 to 1.75 MNs/m^3).

Figure 4.8 (b) shows the numerical calculations at 80 MHz with different mass densities. The normalized reflection intensity is dependent on mass density even if the acoustic impedance is the same. It yields a possibility that the targets may have different density even if they have the same acoustic impedance. However, the influence of the mass density on the result is not significant from 1.4 to 1.8 MNs/m^3. In the figure, the experimental results when using saline solution with different content are plotted. The highest content was 10% by weight, which corresponded to an acoustic impedance of 1.7116 MNs/m^3, a mass density of 1070.7 kg/m^3 and a speed of sound of 1598.6 m/s. The estimated acoustic impedance may include some error because mass density is not known. The possibility deviation error based on this figure is as much as 0.0215 MNs/m^3 or percent error as much as 1.26 %, if mass density is 1100 kg/m^3 is chosen as a calibration curve. However, if 1000 kg/m^3 is chosen as a calibration curve, deviation error may decline as much as 0.0084 MNs/m^3 or 0.5 %. Although the mass density of the target changed from 900 to 1100 kg/m^3, the experimental results were in good agreement with the calibration curve.

4.5.4 Saline Solution Measurement

Substrates typically have higher acoustic impedances than targets, and the reflection intensity decreases with increasing target acoustic impedance. Various saline solution contents, in which acoustic impedance was known, were measured. Either pure water or air was considered as a reference material.

To ensure the beam was in focus at the interface between the upper side of the substrate and the target, the substrate position was set at a distance of 1.745 mm, as shown in Fig. 4.6. At this position, numerical calculation will provide the strongest received intensity. However, it is difficult to determine the exact focal plane in the microscope system because some aberration may occur due to the existence of the substrate. We thus attempt to determine the position where the reflection signal is strongest when we perform the

measurement.

The result of this measurement was plotted in the same table of numerical calculations of the received ultrasound intensity, as shown in Fig. 4.8 (b). From the figure, a substantial discrepancy is found between the vertical incident analysis and the measurement results. The gap becomes more significant as the acoustic impedance of the target increases. Conversely, the gap is found to be significantly reduced if it is compared to the oblique incident analysis calculation. This shows that the numerical calculations agree with the measurements of the saline solutions. Based on the curves at 30 MHz and 100 MHz, there is no significant frequency dependency in this region.

Calculation assuming vertical incidence may provide a good approximation to estimate acoustic impedance of target if the focusing angle is small, as describe in [56, 57]. However, a significant focusing angle is required to obtain good resolution in the resulting image. Based on this result, an oblique incident analysis is believed to be more accurate in calculating an acoustic impedance profile.

4.5.5 Observation of Cerebellar Tissue of Rat

In addition to the theoretical analysis shown, practical observations of the cerebellar tissue of a rat were performed. A rat was dissected, and its whole brain was removed. The isolated cerebellum was sliced using a rotor slicer (Dohan EM, Kyoto, Japan). The slice was incubated in oxygenated phosphate buffer solution (PBS) on ice for one hour. It was then chemically fixed with 4% formaldehyde fixative for 20 minutes.
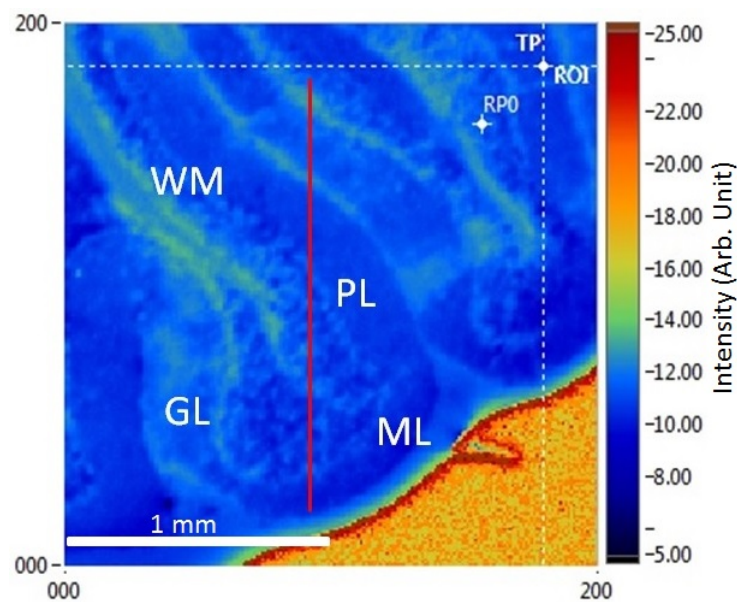

Figure 4.9: Reflection acoustic intensity (arb. unit) of a cerebellar tissue of rat is shown at a scale of 2 mm x 2 mm with 200 x 200 pixels. x and y axes are expressed in pixels.

Some problems may occur due to the contact made between the target and the substrate. Inappropriate contact may generate new layers in between the substrate and target, creating a serious problem that can significantly damage image quality if contact between the tissue and substrate is poor. In such a case, multiple reflections take place across the fluid layer, affecting the frequency spectrum of the reflected signal. This contact problem was discussed in a previous paper [57], where plasma treatment was chosen to solve this problem [85].

Figure 4.9 shows the image of reflection intensity. In the image, the Molecular Layer (ML), Granular Layer (GL), Purkinje Layer (PL) and white matter (WM) are clearly seen. To convert the intensity into acoustic impedance, four different results were produced with vertical incident calculations and focused beam calculations, which used pure water and air as reference materials, respectively. Four 2D acoustic impedance images were produced and compared. Acoustic impedance is found to range from 1.60 to 1.95 MNs/m^3 and from 1.75 to 2.05 MNs/m^3, respectively, as shown in Fig. 4.10 (a) and (b) by the analysis, assuming vertical incidence. Conversely, an acoustic impedance of $1.45 - 1.75$ MNs/m^3 can be found in Fig. 4.11 (a) and (b), when a focused beam was assumed.

As described, the acoustic impedance of the tissue is found to be 1.38 to 1.90 MNs/m^3 [61], and the result assuming a focused beam appears to be more accurate. In addition, the results did not change if the acoustic impedance of the reference material is changed significantly.

Figure 4.12 shows a comparison of acoustic impedances based on oblique incident calculations (i.e., the assumption of this study), vertical incident calculations and calculations using ref [3] along the white line shown in Fig. 4.9. As shown in the figure, vertical incident calculations generated large errors when a highly focused transducer was used. Vertical incident calculations seem to be appropriate when a less focused or flat transducer is used [73]; however, in a previous paper [3], calibration was performed in a similar way to geometric optics. It is assumed that the sound field can be approximately described as a bundle of multiple ultrasound beams. It is known that geometric optics yield a good approximation if the wavelength is sufficiently short compared to the size of the structures with which the wave interacts. Conversely, the wavelength of the ultrasound used in this study is from 15 to 75 micrometers, and the structure of the system is on the order of several hundred micrometers. Thus, in this case, oblique incident calculations and geometric optics calculation yield similar results and are sufficiently accurate, as shown in Fig. 4.12.

However, as shown in Fig. 4.13, the gap between oblique incident calculation and the result from ref [3] becomes significant when the frequency is lower than 20 MHz. If the frequency is sufficiently low, the focal spot becomes wider, and the sound field becomes closer to a plane wave propagating vertically to the substrate; the calibration curve, therefore, becomes closer to the assumption of vertical incidence. It is shown that error increases when the frequency is higher than 100 MHz; this probably originates in aberration due to the insertion of the substrate. The gap is not significant when the frequency is between 20 MHz and 100 MHz.

Geometric optical analysis does not consider frequencies in its calculations and will yield the same
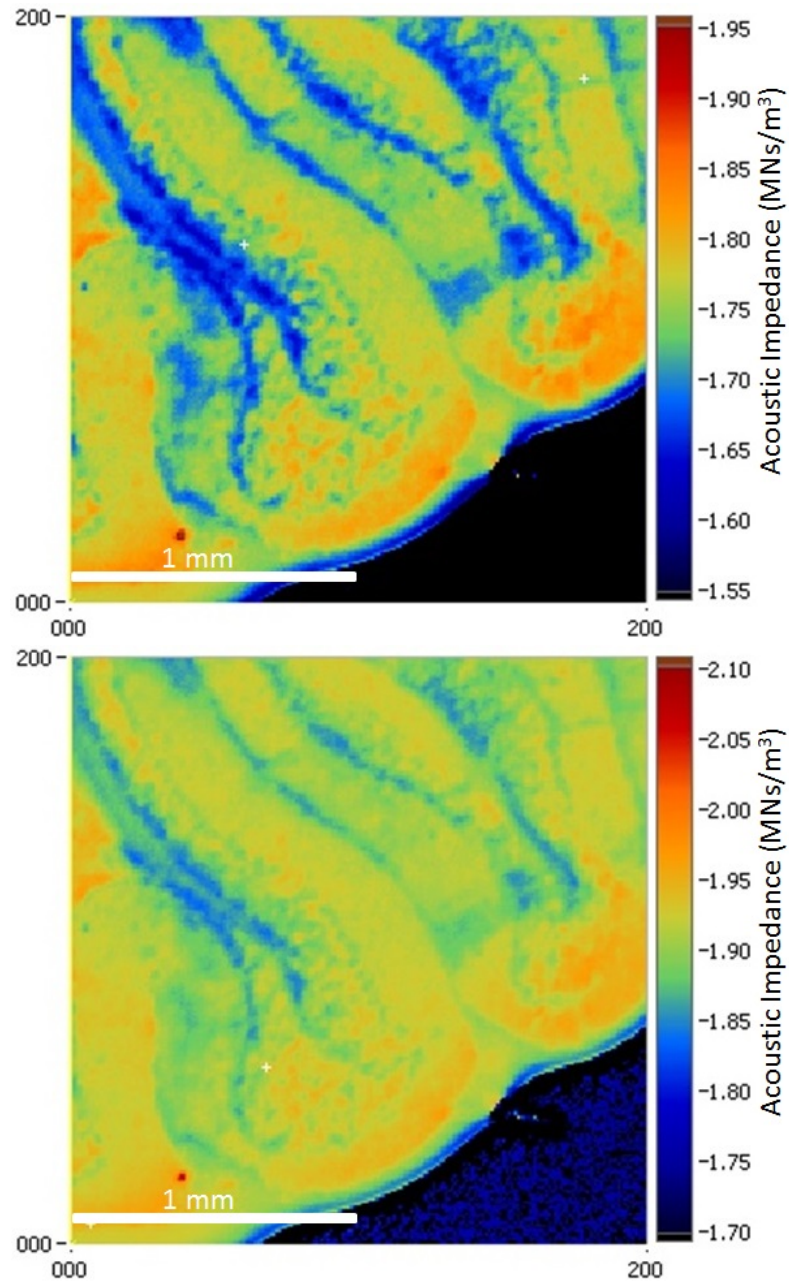
Figure 4.10: Acoustic impedance (MNs/m^3) images of the cerebellar tissue of a rat, based on vertical incident calculations using pure water as a reference material (a) and using air as a reference material (b). Note: the significant differences in acoustic impedance scales. x and y axes are expressed in pixels.
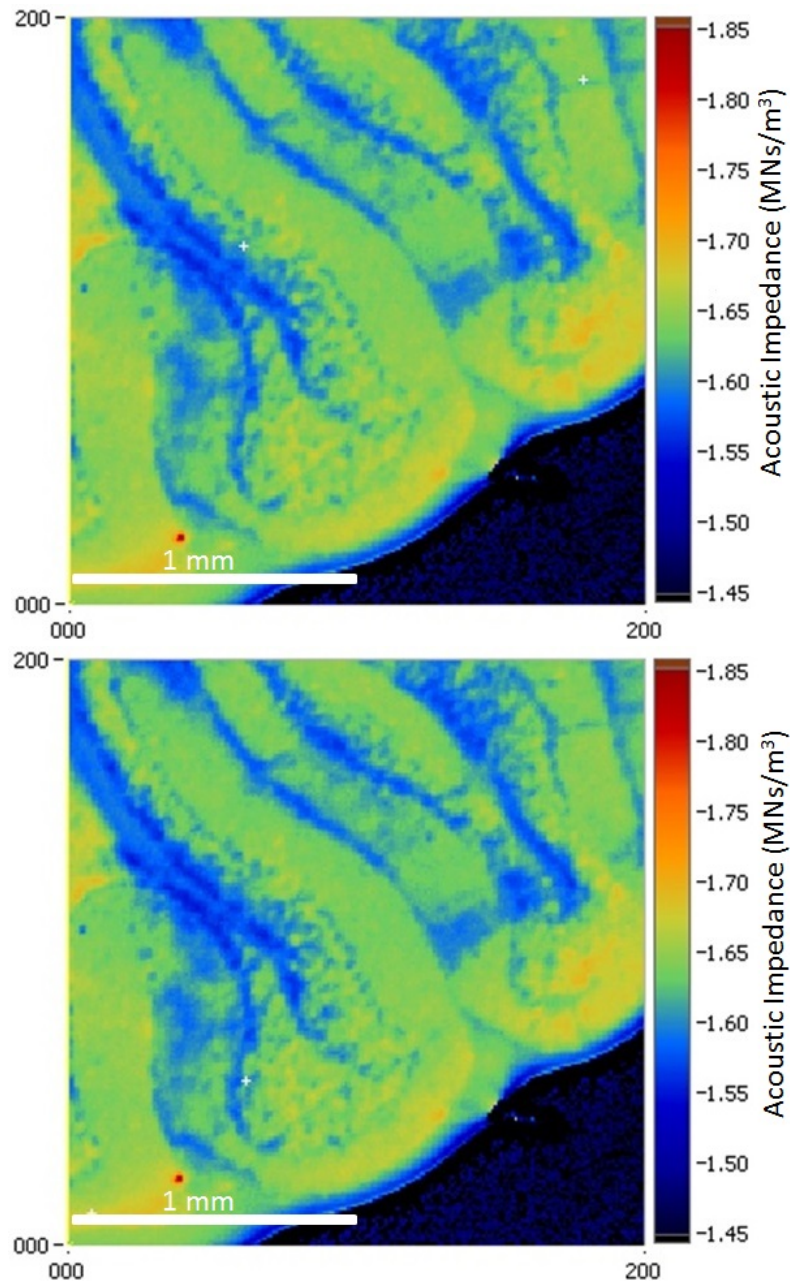
Figure 4.11: Acoustic impedance (in MNs/m^3) images of the cerebellar tissue of a rat, based on vertical incident calculations using pure water as a reference material (a) and using air as a reference material (b). x and y axes are expressed in pixels.
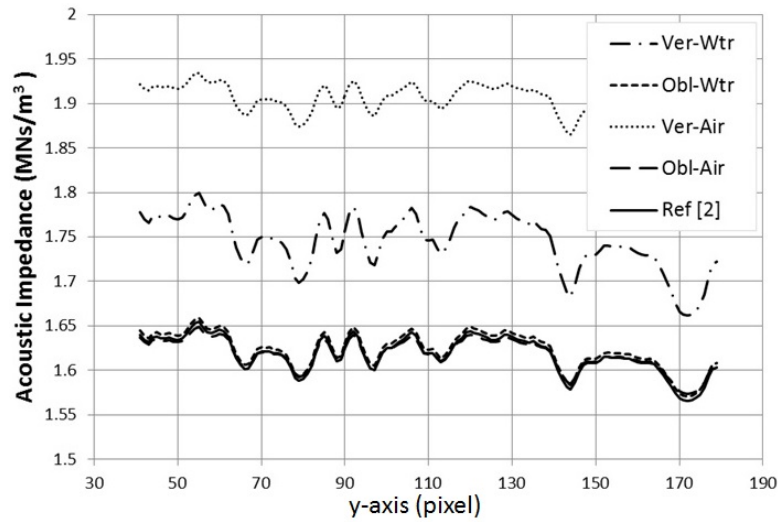
Figure 4.12: Comparison of acoustic impedances along the line shown in Fig. 4.9 based on vertical and oblique incidences and the calculations in ref [3]. Calculations based on ref [3] and oblique incident show more accurate to estimate acoustic impedance of the target compared to that vertical incident calculation.
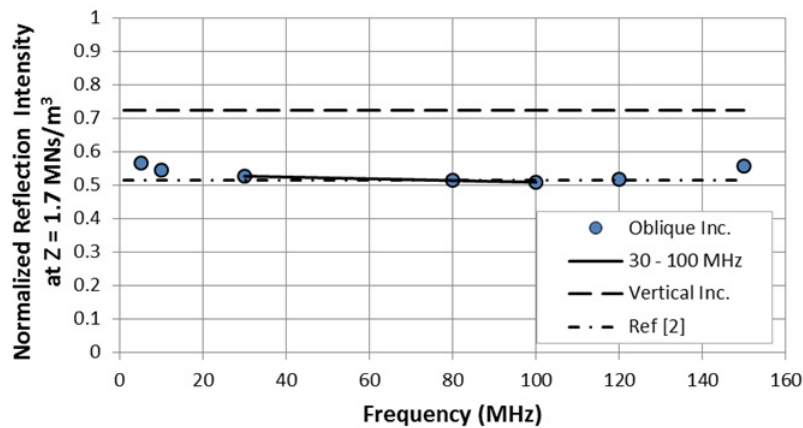
Figure 4.13: Changes in gaps based on the three methods investigated, calculated at 1.7 MNs/m^3. The long-dashed line is obtained from vertical incident calculations; the dash-dot line is obtained from geometric optical calculations [3]; and the circles plotted in the same field are obtained from oblique incident calculations. The solid line is the range of frequencies used in the system.

result of reflection intensity independent of the frequency component of the received signal. Because frequency dependence likely exists, sound field calculations based on wave propagation theory (oblique incident calculation) would be more suitable for accurate calibration. In addition, because the sound field on the target interface can be calculated, it can be expected that image resolution will improve based on the sound field pattern realized.

4.6 Conclusions

We proposed a new type of ultrasonic microscope for biological soft tissues. As the ultrasonic beam is transmitted and received through the substrate (i.e., the target was separated from the coupling medium), a non-invasive observation can be performed without introducing any contamination into the target. In addition, slicing into a thin leaf is not required.

The 2-D reflection intensity profile obtained by scanning the transducer was interpreted into a quantitative profile of characteristic acoustic impedance. For this purpose, sound field was calculated using Fourier analysis. Because the beam was highly focused onto the target, the ultrasonic beam was decomposed into plane waves with different incident angles, and the reflection depending on the incident angle was considered. Subsequently, a calibration curve between the reflection intensity and acoustic impedance was produced that suggested that there was no significant frequency dependence between 30 and 100 MHz. The calibration curve was verified using various contents of saline solution, of which acoustic impedance was known. Based on this result, oblique incident analysis is believed to be more accurate to obtain an acoustic impedance profile.

Finally, the cerebellar tissue of a rat was observed to create an acoustic impedance micro profile. As a part of the tissue, Molecular Layer, Granular Layer, Purkinje Layer and White Matter are clearly observed. From this result, we are pretty sure that this technique can be utilized to discriminate healthy and cancerous tissue, because they have difference stiffness and softness based on cytoskeleton component [86–88]. This technique can skip some processes that are needed by optical microscope, as well as another technique such as PET. It led to a very fast observation. We are very optimistic that such this technique is very useful for quick inspection during the surgery.

Chapter 5

Acoustic Impedance Microscope for Cell Observation

5.1 Brief Description

A new technique is proposed for non-contact quantitative cell observation using focused ultrasonic waves. This technique interprets acoustic reflection intensity into the characteristic acoustic impedance of the biological cell. The cells are cultured on a plastic film substrate. A focused acoustic beam is transmitted through the substrate to its interface with the cell. A two-dimensional (2-D) reflection intensity profile is obtained by scanning the focal point along the interface. A reference substance is observed under the same conditions. These two reflections are compared and interpreted into the characteristic acoustic impedance of the cell based on a calibration curve that was created prior to the observation. To create the calibration curve, a numerical analysis of the sound field is performed using Fourier Transforms and is verified using several saline solutions. Because the cells are suspended by two plastic films, no contamination is introduced during the observation. In a practical observation, a sapphire lens transducer with a center frequency of 300 MHz was employed using ZnO thin film. The objects studied were co-cultured rat-derived glial (astrocyte) cells and glioma cells. The result was the clear observation of the internal structure of the cells. The acoustic impedance of the cells was spreading between 1.62 - 1.72 MNs/m^3. Cytoskeleton was indicated by high acoustic impedance. The introduction of cytochalasin-B led to a significant reduction in the acoustic impedance of the glioma cells; its effect on the glial cells was less significant. It is believed that this non-contact observation method will be useful for continuous cell inspections.

5.2 Background

Several methods are available for examinations of biological and medical specimens, such as X-rays, electromagnetic waves, and optical and acoustical microscopes. For microscopic images, optical rays have short wavelengths that provide very high resolution images. However, because it is not easy to obtain good image contrast, staining is needed. The staining process adds a contaminant to the target. In addition, it requires several hours to perform the staining process. Finally, heavy staining has the potential to alter the biological function of the target or even damage it, causing loss of the target's information.

On the other hand, scanning acoustic microscopy (SAM) is an advantageous method of non-destructive analysis with which the user can measure a sample's properties without touching or damaging it. Because the staining and slicing processes are avoided, the time required for observation is very short. Furthermore, this method has the benefit that it can provide a quantitative evaluation of viscous-elastic or acoustic properties of the target [73, 89–92].

Several researchers have used SAM for cell observation [3, 89–93]. Vector contrast SAM was developed for imaging living stem cells. Signal processing, autofocusing and image processing are required for creating time-lapse motion pictures of mesenchymal stem cells [94]. Zang *et al.* utilized an atomic-force acoustic microscope to study the surfaces, intracellular structure and elasticity of Vascular Smooth Muscle Cells [95]. They mainly placed SAM instrumentation around the cell in the top to bottom order of transducer, coupler, cell and substrate. With this arrangement, they could measure the cell surface, its thickness or the speed of sound in the cell because they had access to the cell's internal structure. However, because the transducer, cell and coupling medium were integrated, it was possible to introduce a contaminant.

Kobayashi *et al.* reported successfully investigating the acoustic impedance of biological tissue [73]. They prevented target contamination during observation. Vertical incidence analysis was used to estimate the acoustic reflection intensity from a small angle of a focused transducer. In our last studies [15, 96], a significant focus transducer was employed with frequencies in the 30 - 100 MHz range. Oblique incidence was taken into account, instead of only vertical incidence analysis. The soft tissue of a rat brain was successfully interpreted with acoustic intensity, which was subsequently converted into acoustic impedance utilizing a calibration curve. These studies provided two advantages: quantitative analysis and freedom from contaminants during observation.

We have used the previous study [96] for a smaller target (*i.e.*, cell structure instead of biological tissue). However, for viewing a cell, the image quality was reduced because the spatial resolution was too low. As the target shrinks, higher spatial resolution must be used to obtain a high-quality image. Hence, higher acoustic frequencies must be applied [4, 50, 97].

In this chapter, we perform quantitative and contaminant-free measurements of cultured cells. We propose a calibration curve as a new method to estimate the acoustic impedance of a cultured cell. A transducer lens with a small radius of curvature is employed. To establish a calibration curve, the lens curvature shape, oblique incidence, frequency dependence and medium properties are considered. To treat multilayered media, we refer to Tittmann *et al.* [83] and the previous works [96]. Numerical calculations with Fourier Transforms are used to obtain acoustic intensities, and the resulting calibration curves are presented. Cell measurements and observations of the effects of drugs utilizing this system are also exhibited.

5.3   System setup and material preparation

Figure 5.1 show a diagram of the SAM used in this research. Glial or glioma cells were used as targets. They were injected into a culture dish and preserved in an incubator before observations. The three major components are described in this chapter: the culture dish and culture method, the transducer, and the observation system.
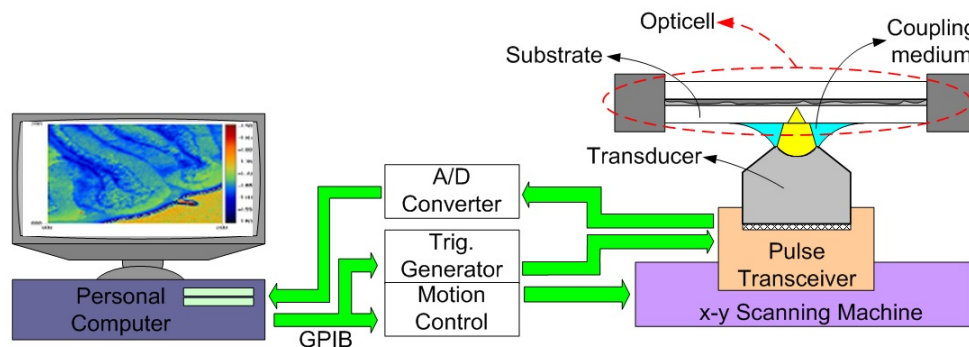
Figure 5.1: Schematic diagram of the SAM [4].

5.3.1   Culture dish and culture method

An OptiCell Cell Culture System (Thermo Scientific Inc. MA, USA) was chosen to cultivate the cell. It had two polystyrene films with thicknesses of 80 μm and a 2 mm gap. The polystyrene film is also used as a substrate during the measurement. Glial cells and gliomas were cultured in the modified astrocyte-deficient medium [98]. Briefly, glial cells were prepared from neonatal VGAT-venus rat cerebellum, and cultured in 10% Calf-serum containing Hanks MEM with 4 g/L glucose and 0.02 g/L kanamycin. After one week incubation, purified and fluorescent glial cells were mixed with rat C6 glioma (DS Pharma Biomedical Co. Ltd. Osaka, Japan), incubated for 4 days before being observed.

5.3.2   Transducer

A transducer of ZnO piezoelectric material (Honda Electric, UPF-5A type) was used for both transmitting and receiving the acoustic wave pulse. The transducer was attached with a sapphire lens of (assumed uniform) curvature of 60 degrees, 0.41 mm aperture diameter and 0.25 mm radius. Pure water (speed of sound = 1480 m/s, density = 1000 kg/m^3) was chosen to couple the substrate and the transducer as shown in Fig. 5.1.

5.3.3 Flow work of system

A set of programs constructed under LabVIEW was run in a Personal Computer (PC). The PC could send two commands through a General Purpose Interface Bus (GPIB). The first command was a motion control that was sent to the stage controller (SIGMA KOKI, SHOT-204MS), which relayed the command to two stepper motors (SIGMA KOKI, serial number 1101585) for x-y scanning. The size of x and y axis steps was adjustable. The second command was sent to a MultiFunction Synthesizer (WaveFactory, model WF 1946B) to create a short pulse. Short pulses were cyclically generated (100 kHz) from the Synthesizer and sent to the transducer. The transducer converted the electrical pulses into ultrasound waves, and transmitted them from the bottom. The focal point was on the interface between the substrate and the cells. Adjusting the focal point was not easy; it was found by moving the transducer up and down until the maximum reflection intensity was received by the transducer. The ultrasonic beam reflected from the local area of the target with a frequency spread from 200 – 400 MHz (as shown in Fig. 5.8) was subsequently received by the same transducer, sent to the PC through an Agilent Acqiris U1065A (model DC222), and interpreted as acoustic intensity. By scanning the target, a 2-D image of reflection intensity was obtained.

5.4 Analysis and Method

5.4.1 Sound fields analysis
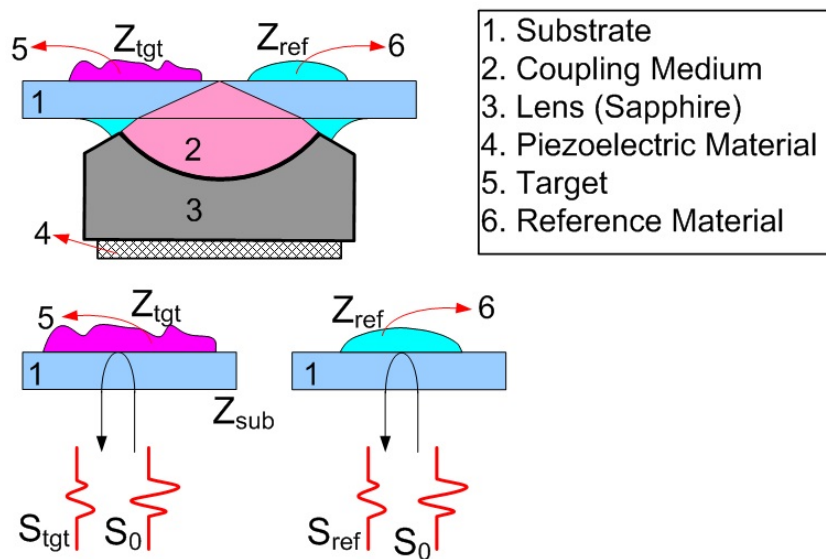
Figure 5.2: Illustration of reflection intensity by assuming vertical incidence. S_0 is the transmitted sound, S_{tgt} is the reflection from the target, S_{ref} is the reflection from the reference, and Z_{tgt}, Z_{ref} and Z_{sub} are the acoustic impedances of the target, reference and substrate, respectively.

Figure 5.2 illustrates the interpretation of reflection intensity as acoustic impedance. Reflection from the target is compared with that from the reference material. In the previous paper [73]it was assumed that the incidence was perpendicular to the substrate. This assumption might be appropriate when the angle of focus is small. However, in this study, the angle of focus was as much as 60 degrees to retain a high spatial resolution. Therefore, we performed sound field analysis to accurately calculate the relationship between reflection intensity and acoustic impedance.
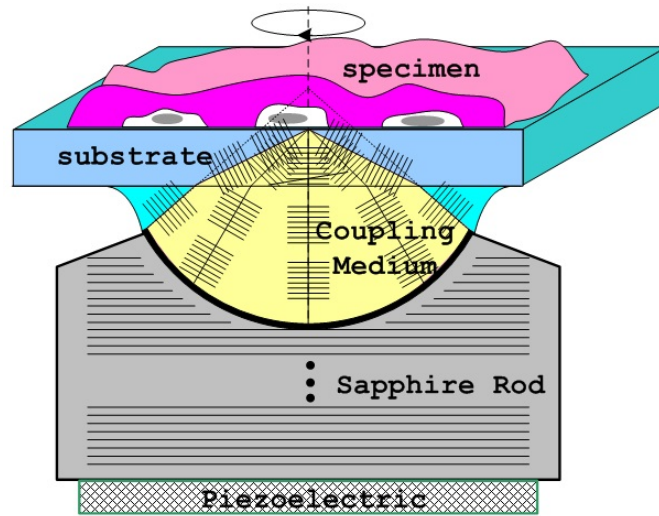
Figure 5.3: Illustration of plane wave component and plane wave decomposition in *k*-space.

Figure 5.3 illustrates the plane waves (in *k*-space) inside each medium with their propagation concepts. Because the piezoelectric device is flat, one component of a plane wave propagates into the sapphire lens, producing sound field potentials on its concave side. Subsequently, a focused beam is produced that can be represented by a number of plane waves with different propagation angles. Each plane wave component strikes the substrate, is reflected from its top surface, and returns to the lens with the same length path inside each medium. The reflection intensity can be calculated as follows.

5.4.1.1 Sound potential on the curved shape

Figure 5.4 shows a diagram of the transducer with its concave lens. One plane wave component is transmitted from the piezoelectric material to the lens, reaching the concave shape. The sound potential at each point on the concave lens is affected by phase delay. The shortest path of the beam inside the lens is at the center of the transducer ($\Delta 0$); $\Delta(x,y)$ is the path of the beam based on radial aperture as a function of x and y. The total phase delay φ at the concave inside of the lens can be expressed as Eq. 5.1.

$$\varphi(x,y) = \frac{\omega}{c_l}.(\Delta(x,y) + \Delta_0), \tag{5.1}$$
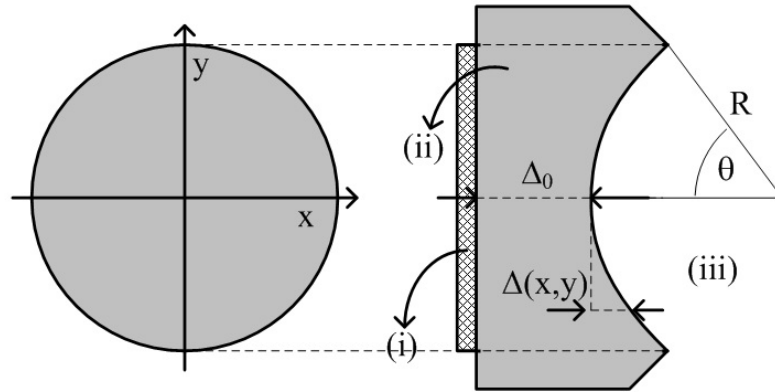
Figure 5.4: Diagram of the transducer. (a) Top view. (b) Side view. Three layers shown as: (i) Piezoelectric material, (ii) Lens rod and (iii) Coupling material.

$$\Delta(x,y) = R - \sqrt{R^2 - (x^2 + y^2)}, \tag{5.2}$$

where R, ω and c_l are radius of the concave, angular frequency of the sound and speed of sound in the lens, respectively.

5.4.1.2   Sound field inside the coupling medium

The plane wave arriving at a point on the concave surface produces a sound potential on the coupling medium side depending on the transmission coefficient and the incident angle to that particular point. As the result, a number of sound potentials with different phases and intensities are generated on the concave surface.

Assuming the coupling medium is uniform, the sound field at a point $\phi(x,y,z)$ from a small fragment of sound source at the concave surface da is described as

$$\phi(x,y,z) = \phi_0 . \frac{e^{-j(\mathbf{k}.\mathbf{l})}}{|\mathbf{l}|} \, da, \tag{5.3}$$

where, ϕ is the sound potential, ϕ_0 is the unattenuated potential at the concave surface, $\mathbf{l}$ is the distance to the point from the small area, $\mathbf{k}$ is the wave number, and da is a small area. In the same manner, the potential distribution can be calculated along a line at z. Because the geometry of the transducer is axially symmetric, a rotation of the potential distribution line will produce a 2D potential distribution on a plane. Figure 5.4 illustrates how to calculate the sound field at a point from the concave surface. The sound field inside the coupling medium can thus be calculated.
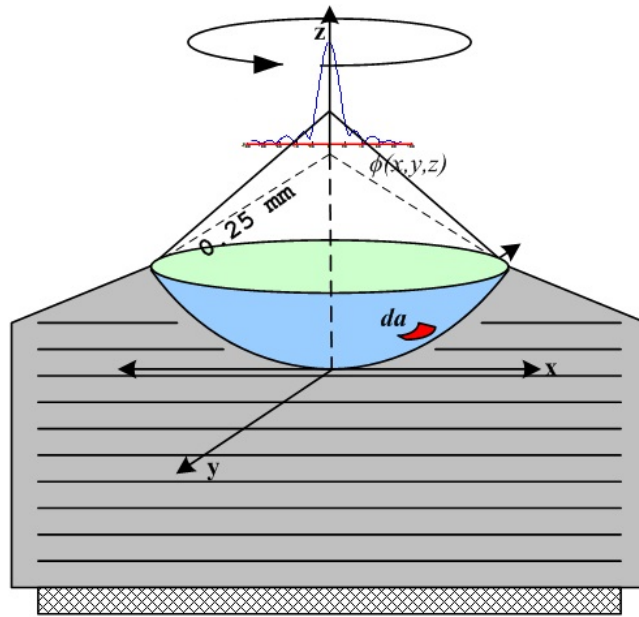
Figure 5.5: Geometrical shape of transducer and sound potential at a certain line at a certain z.

5.4.1.3 Sound field inside the substrate

The sound field in the coupling medium can be interpreted as plane waves with different incident angles by transforming real space into k-space utilizing a 2D Fourier transform. Each plane wave that enters the substrate changes its angle of propagation following Snell's law. The transmission coefficient is determined by the speed of sound and the acoustic properties of the pressure wave in the coupling medium and those of the pressure and shear waves in the substrate.

5.4.1.4 Received signal

Each plane wave component in the substrate is reflected at the interface between the substrate and target, returns through the same medium and is received by the same transducer. Therefore, if the sound field in the substrate in k-space is known, the signal received by the transducer, depending on the acoustic properties of the target, can be calculated. The signal intensity is subsequently normalized with that from the reference material to create the calibration curve.

In fact, when oblique incidence occurs, two types of waves, pressure and shear waves, are generated in the substrate for both transmission and reflection. Because a pressure wave in solid material usually moves faster than a shear wave, an appropriate window function can be used to analyze the two waves separately. In this research, we take only the pressure wave into account for calculation and measurement. A detailed expression of the calculation is described in ref. [96].

5.4.2 Acoustic impedance estimation method

Acoustic impedance was estimated using a calibration curve that converts normalized intensity into acoustic impedance. To develop a calibration curve, we used several saline solutions as targets and calculated the received intensity based on the description above. The result of the calculation was normalized by the received intensity from the reference material (pure water). Thus, a calibration curve can be established.

The calibration curve was then evaluated by measuring various saline solutions whose acoustic impedances were known.

5.5 Result and discussion

5.5.1 Calibration curve

Figure 5.6 shows a typical sound field corresponding to the employed transducer. Part (a) represents the sound field in pure water. When the 0.08-mm-wide substrate is inserted, the beam is bent with a new propagation angle and forms a new focal point, as shown in part (b). The substrate is positioned such that the focal area of the beam is exactly at the interface between upper side of the substrate and the target to obtain the maximum reflection intensity from target. Based on this analysis, the reflected intensity from the assumed target, which can be measured by the same transducer, can be calculated.
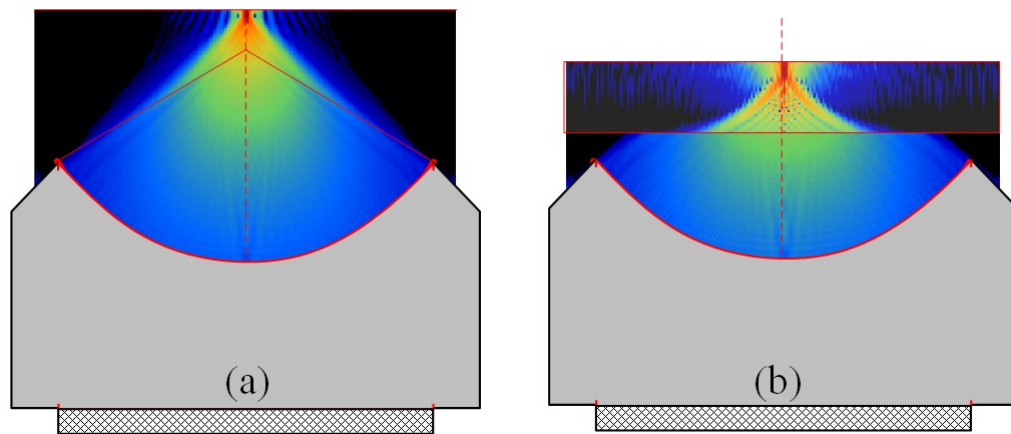

Figure 5.6: Ultrasonic propagation transmitted from ultrasonic lens transducer in (a) pure water (b) pure water and polystyrene as a substrate. Frequency: 300 MHz.

Several similar methods have been proposed by other authors. Raum *et al.* proposed acoustic impedance estimation based on C-mode multi-layer measurement. Acoustic impedance is converted from the voltage

of the maximum image, which is influenced by the material and inclination of the target [99]. Estimation of acoustic impedance for biological tissue were made utilizing geometric optical analysis [3] and vertical incidence analysis [73]. In chapter 4, we introduced a new technique for estimating the acoustic impedance of the target by establishing a calibration curve. A calibration curve was used to convert acoustic intensity into acoustic impedance [96]. A comparison between this technique, geometric optics and vertical incidence analysis was also exhibited. Based on this comparison, we believe that the established calibration curve shown in ref [96] is more accurate for obtaining an acoustic impedance profile.

In this research, we developed a calibration curve based on the system used in this chapter. By executing the same procedure described in the previous chapter, the calculated intensity corresponding to different acoustic impedances of the assumed target is subsequently normalized by the intensity corresponding to the reference material. Through this calculation, a calibration curve is established. As discussed in the following sections, pure water, whose acoustic properties are known, is a good reference material, but we can employ other materials as long as their acoustic impedances have been assessed using pure water as the reference material. The targets might have the same acoustic impedance, but different density. To include this condition, the target properties, i.e., the density, was broadened to include 900, 1000 and 1100 kg/m^3 in the calculation. Based on these numbers, three calibration curves were created as shown in Fig. 5.7 (i). The dashed, solid and dashed-dotted curves show calibration curves utilizing the density of 900, 1000 and 1100 kg/m^3. Because the gaps between the curves are not significant, 1000 kg/m^3 is used as a representative number.
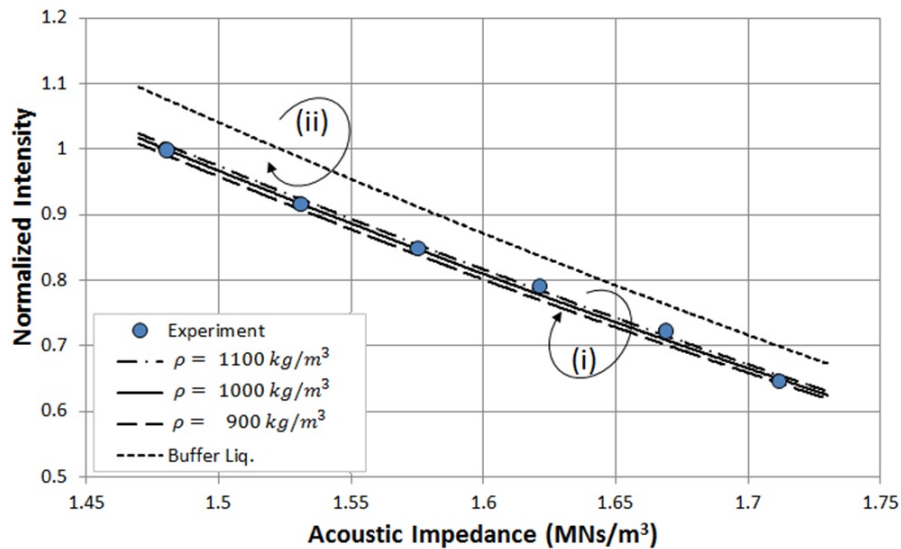

Figure 5.7: Calibration curves established from reflection intensity calculation by sound field analysis at the frequency of 300 MHz. Water was used as a reference is shown in (i) bundle. Buffer liquid was used as a reference shown in (ii). Saline solution measurements of which acoustic impedance were known, were plotted on the calibration curve based on calculation.

5.5.2   Verification using saline solution

To validate the calibration curve we observed saline droplets, whose acoustic impedances are known. The reflected intensity was then normalized using pure water droplets. The results are shown as plots overlapped on curve (i) in Fig. 5.7. It can be observed that the results are in good agreement with the calibration curve in the region of 1.48 – 1.73 MNs/m^3. We can therefore use curve (i) as the master calibration curve.

However, in cell observations of this type, cells are usually observed with buffer liquid. In such a case, the observation of pure water should be done as a different batch. If the buffer liquid can be observed together with cells in the same field of view, it is more convenient to use the buffer liquid itself instead of pure water. For this purpose, the acoustic impedance of buffer liquid can be assessed using pure water prior to the cell observation.

The curve (ii) in Fig. 5.7 shows the calibration curve using the buffer liquid as the reference material. The acoustic impedance of the buffer liquid was assessed as 1.526 MNs/m^3, prior to the calculation.

5.5.3   Frequency dependency

Figure 5.8 shows the profile of the signal received from the target in the time domain and its frequency components. A band-pass filter of -6 dB was used to pass the frequency spread between 200 to 400 MHz. Because a bundle of frequencies operate in this system, we need to know the contribution of each frequency component to establish a calibration curve. Thus we took three frequency components, 200, 300 and 400 MHz, into analysis. The normalized reflection intensity of these frequencies was calculated as shown in table 5.1. It can be observed that the frequency dependence of the reflection is almost negligible from 200 to 400 MHz. We concluded that the calibration curve in Fig. 5.7 is applicable for all of the frequency components employed in this measurement.
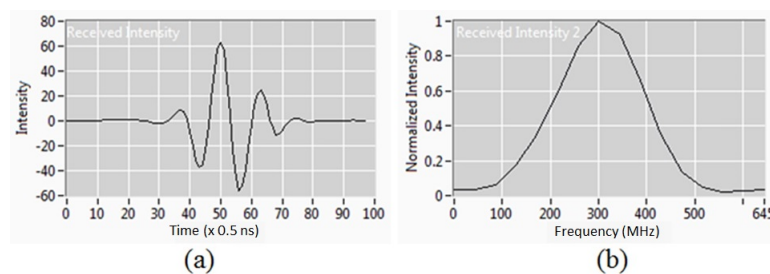

Figure 5.8: A Typical received signal intensity from the target. (a) Time domain. (b) Frequency domain.

Ac. Impedance	Normalized Intensity			Perc. Error
(MNs/m^3)	200 MHz	300 MHz	400 MHz	(%)
1.48	1	1	1	0
1.534	0.91365397	0.91464	0.916075	0.26463
1.581	0.84472205	0.845822	0.847886	0.37386
1.628	0.77706184	0.777471	0.779537	0.31802
1.677	0.71140787	0.710087	0.711334	0.010384
1.721	0.65623485	0.652315	0.651952	0.654776

Table 5.1: Calculation of normalized intensity at 200, 300 and 400 MHz. Percentage error is obtained by comparing data of 200 MHz and 400 MHz.

5.5.4 Attenuation dependency

As it is already described in the previous section, in order to obtain high resolution we need to employ high frequency. However, high frequency has a disadvantage, it is big attenuation. In this section we need to evaluate whether attenuation give a big impact in the calculation. Obviously, attenuation will decrease the received acoustic intensity. However, when we did normalized calculation, the impact of attenuation is almost negligible as shown in the table 5.2

Ac. Impedance	Intensity		Normalized Intensity	
(MNs/m^3)	No Att	With Att	No Att	With Att
1.48	0.0015833	0.000396103	1	1
1.534	0.00144972	0.00036269	0.915631908	0.915646
1.581	0.00134226	0.000335808	0.847761005	0.847779
1.628	0.00123533	0.000309062	0.780224847	0.780257
1.677	0.00112942	0.000282571	0.713332912	0.713378
1.721	0.00103859	0.000259851	0.655965389	0.656019

Table 5.2: Calculation of attenuation using various saline solutions as targets. The result is shown in normalized intensity at 300 MHz.

5.5.5 Observation of Glial cell

For cell observation, most authors have employed ultrasound to penetrate the target, so that the speed of sound in the target is known. Acoustic impedance is obtained by multiplying the speed of sound by the density of the target. In this study, we focused on the cell area, which is laid along the interface between the substrate and cell. Thus, we measure the acoustic intensity reflected from this interface. The acoustic impedance of the target is estimated by converting acoustic intensity with the calibration curve.

Regarding cell imaging, several authors have performed measurements. One problem appears to be

the interference of the reflected signal caused by cell-to-substrate adhesion. Experiments by Brand *et al.* show that the cells were exposed to cisplatin. After several hours (more than 2.5 hours), several cells were growing dark in some of their areas, signaling that the cells were undergoing cell death [100]. There are four phases of a normal cell dying: the normal phase, shrinkage, poor adhesion and cell death, after which the cell floats [101]. Normally or shortly after the cell is exposed to a drug, the cell has normal adhesion to the substrate. A study of a new layer produced by cells for substrate adhesion was performed by Curtis [102]. Later, Izzard and Lochner improved the measurement and eliminated some possible errors [103]. They examined three types of adhesion: focal contact (45 nm), close contact (79 nm) and greater separation (112 - 138 nm). In 1999, Giebel *et al.* also investigated cell substrate adhesion based on Surface Plasmon Resonance Microscopy (SPRM). Their results (25 ± 10 nm for close contact and 160 ± 10 nm for other part of the cell) are in good agreement with those of Izzard and Lochner [104]. Kundu *et al.* also demonstrated that the liquid layer under the cells is of the order of under 100 nm [105]. The appearance of a new layer may have major or minor influence [89] depending on the target and system used.

In this study, we measured the reflection at the interface between the substrate and the cells. In this stage we assumed the target was uniform along its depth and monolayer. A new buffer liquid layer may have appeared between the substrate and the cell. This new layer may significantly influence the reflected intensity. However, we have ignored this effect because the intensity is almost negligible.

Figure 5.9 (a) shows the reflection intensity image with cultured glial cells. The acoustic intensity image was subsequently converted into characteristic acoustic impedance as shown in Fig. 5.9 (b). For this process, because the buffer liquid was visible in the field of view, the calibration curve of Fig. 5.7 (ii) was applied. . If the buffer liquid is not visible, a pure water droplet observed under the same conditions can be used as a reference. In such a case, the calibration curve in Fig. 5.7 (i) can be applied.

In Fig. 5.9, internal structure of each cell is visible. It is assumed that the many white circles in 5.9 (b) correlate to higher acoustic impedance. Other areas, both inside and outside the white circles, have lower acoustic impedance. It can be compared with Fig. 5.10 (a) which is the acoustic impedance profile of a typical glial cell in an enlarged scale. A dark color represents high reflection intensity; conversely, bright color represents low reflection intensity. The result in Fig. 5.10 (a) was obtained from converting acoustic reflection intensity into acoustic impedance utilizing the calibration curve.

The cell is 70% water [106]. Most of the cell is cytoplasm (the gel-like part of cytoplasm is cytosol), whose viscosity is roughly the same as pure water [107]. It is known that cytoskeletons are distributed within the cytoplasm, but they were not dissolved.

Based on Fig 5.10 (a), it can be observed that the cells were trying to move (cell motility). Five steps were performed. First, the cell produced a protrusion. A membrane was pushed by polymerization of cytoskeletal filaments. Then, the cell created an adhesion point on the side of the protrusion. Third, the cell contracted to move in the movement direction. The cell then de-adhered and finally retracted its rear part [108, 109].
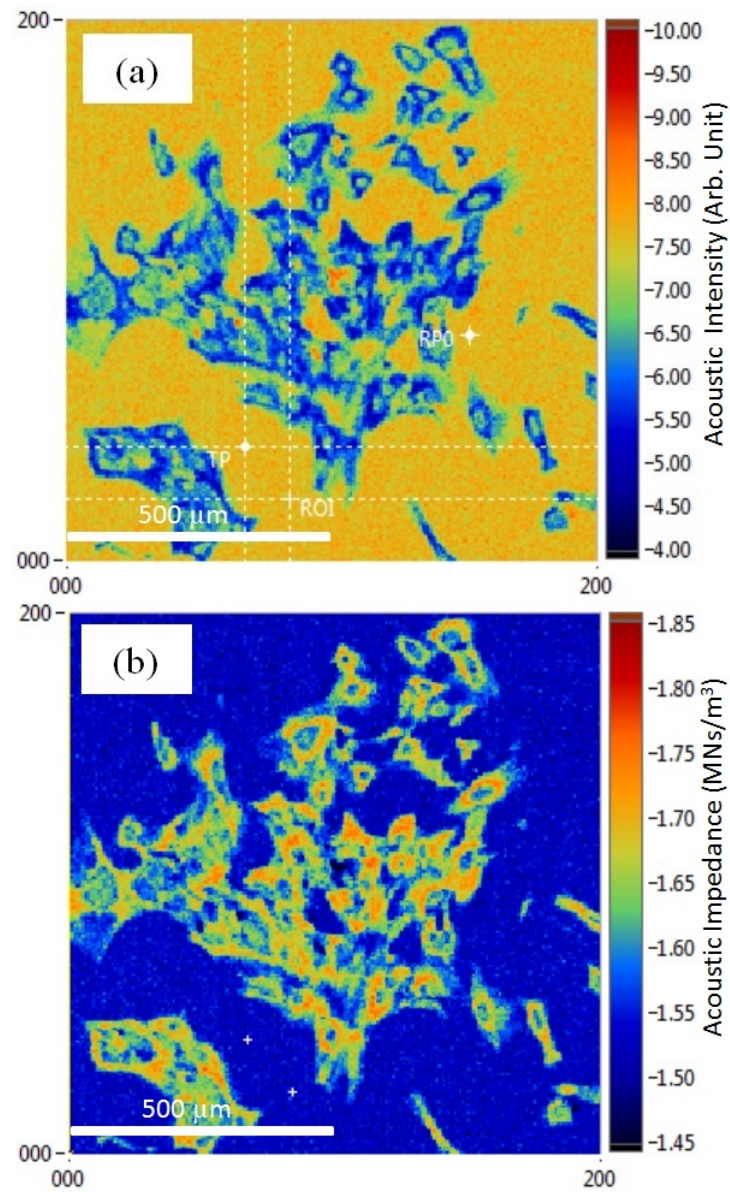
Figure 5.9: (a). 2-D image of cultured glial cells is obtained from acoustic reflection intensity (arb. unit). (b). 2-D image of acoustic impedance is converted from the curve (bottom). These figures are 1000 x 1000 μm, covered by 200 x 200 pixels.

Figure 5.10 (b) shows several areas. Cell motility was well defined by Mitchison and Cramer [108], who classified cell motility into three areas. The protrusions shown in area-4 contain actin microtubules, part of the cytoskeleton. This was also well defined by Raftopoulou and Hall [110]. The cell body is defined as the thickest region of cytoplasm containing the nucleus. This region is shown as area-1 and area-2. The region of intermediate thickness (called the lamella) is between the nucleus and the protrusive structure and is shown as area-2. Both the cell body and intermediate body comprise actin filaments, which can be observed from electron microscopy and fluorescent studies.

Because we know that cytoskeleton is composed of actin filaments and microtubules, area-2 is shown as high acoustic impedance. The center of the body area (area-1) shown with lower acoustic impedance is presumed to be a nucleus. Because the nucleus is suspended by cytoskeleton, it is conjectured that the distance between the substrate and nuclei could be as much as several micrometers. Therefore, it is assumed that the acoustic impedance at this point is not directly influenced by the nucleus itself. Area-3 could be composed of cytosol with fewer actin filaments. It is shown as having less acoustic impedance than the area-2 because cytosol has a viscosity similar to water.

Figure 5.11 shows the transition in acoustic impedance along the vertical line indicated in Fig. 5.10 (a). The two curves are the results calibrated by two different reference materials, *i.e.*, buffer liquid and pure water. The two curves are in good agreement, suggesting that pure water observed at a different time but under the same conditions can be applied as a reference as well when buffer liquid is not visible in the field of view.

From the graph, pixels 25-45 and those over 180 are suggested to be buffer liquid, with its acoustic impedance approximately 1.52 MNs/m^3. The area shown in circle 6 has higher acoustic reflection intensity compared to the surrounding area (circles 5 and 7). This measurement result is in agreement with the comparison results of optical and acoustical images shown by Storhm and Kolios [91], in which the nucleus is shown as of brighter intensity compared to the surrounding area and located in the center. However, Weiss *et al.* showed the opposite, where the center of cell surface is shown as a bright spot (dark color) [90]. In this measurement, the nucleus is estimated as little as 1.6 MNs/m^3 (see circle 6), but as mentioned above, this value is not reliable. Its surrounding area has approximately 1.62 – 1.72 MNs/m^3 in acoustic impedance (see circles 5 and 7). In this estimate of acoustic impedance, the area surrounding the nucleus has the highest acoustic impedance. We presume this area consists of rich actin filaments and microtubules (cytoskeleton composers) that have high density and elasticity compared to cytosol.

Measurement of glial cells by an acoustic microscope showed that its acoustic impedance ranges between 1.5 – 1.7 MNs/m^3 [97]. Other authors showed hela cells' acoustic impedance was 1.55 – 1.697 MNs/m^3 [90–92]. These are in quite good agreement with the results of our measurements even though there are some differences between these two types of cells.
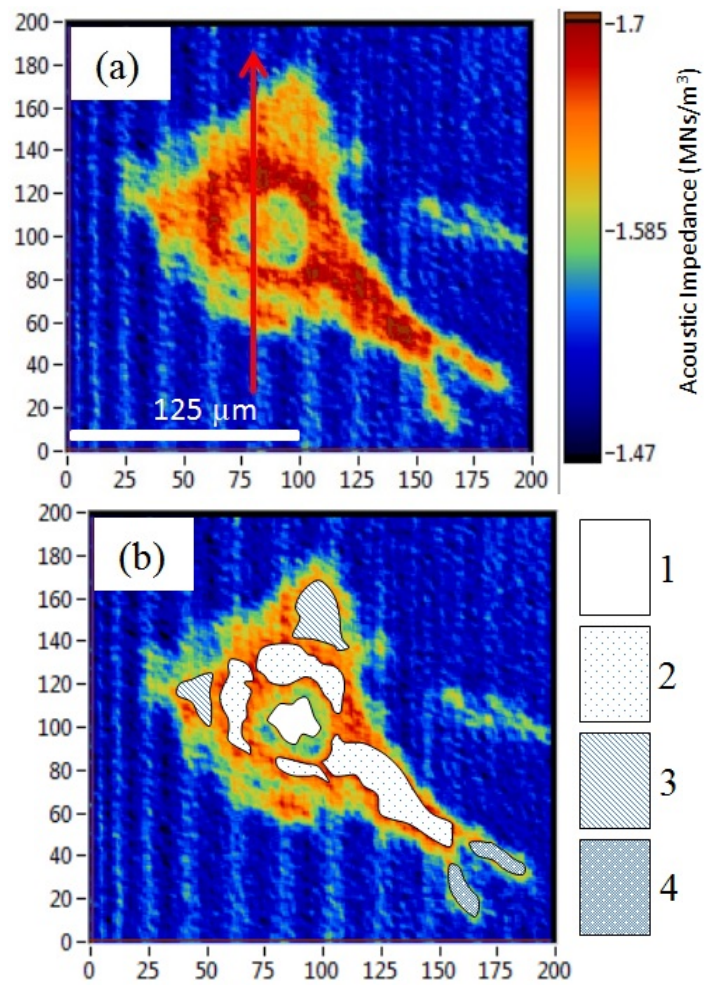
Figure 5.10: (a). 2-D acoustic impedance profile using buffer liquid calibration curve. (b). Regions of cell based on motility process. These figures are 250 x 250 μm, covered by 200 x 200 pixels.
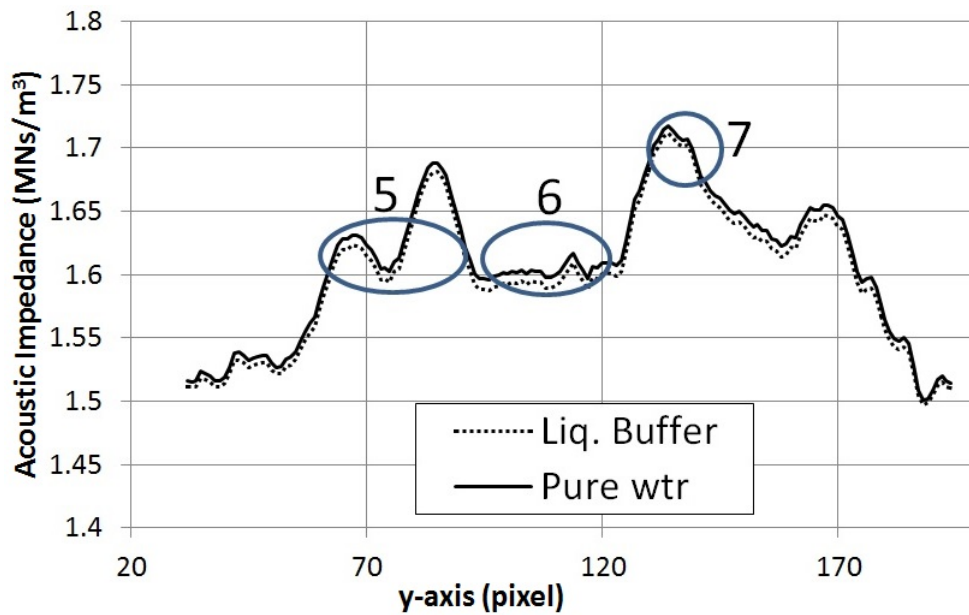
Figure 5.11: Acoustic impedance graph of glial cell along the vertical line shown in Fig. 5.10. Solid line is the graph normalized by pure water. Dotted line is the graph normalized by buffer liquid as reference.

5.5.6   Observation of co culture expose to drug

Because this technique is non-invasive and free from contaminants, it is suitable for inspecting the effects of drugs on the cell. Several authors exploit cytochalasin as a drug and observed its effects on targets. Cytochalasin is used to observe the susceptibility of Galleria mellonella larvae to infection [111] and to observe the correlation of toxin level with the power spectrum generated by electric cell-substrate impedance sensing (ECIS) [112]. As an example, in this chapter, the effect of Cytochalasin-B on glial cells and gliomas is exhibited. Figure 5.12 shows the acoustic impedance image of co-cultured glial cells and gliomas. To identify each glial cell or glioma, the specimen was observed under an optical fluorescent microscope prior to ultrasonic inspections. Glial cells were identified relative to glioma because they emit a specific fluorescence. Here we show two typical glial cells are indicated by circles and gliomas by rectangles.

Acoustic impedance images were acquired shortly before the injection of cytochalasin-B (*i.e.*, 25 μg/ml), and 40 and 90 minutes after the injection. As shown in Fig. 5.13 glial cells had only a small change in their acoustic impedance images, whereas gliomas demonstrated a significant reduction in acoustic impedance. In order to reinforce this result, the target was also observed under fluorescent microscope as shown in fig. 5.14. Bright area shows fluorescent illumination from glial cells.

In addition, we examined nine regions of interest before and 90 minutes after the injection and statistically analyzed them with T-tests. As shown in Fig. 5.15, gliomas were more significantly affected by cytochalasin-B than glial cells in terms of acoustic impedance. The T-test results (5% tolerance) were that
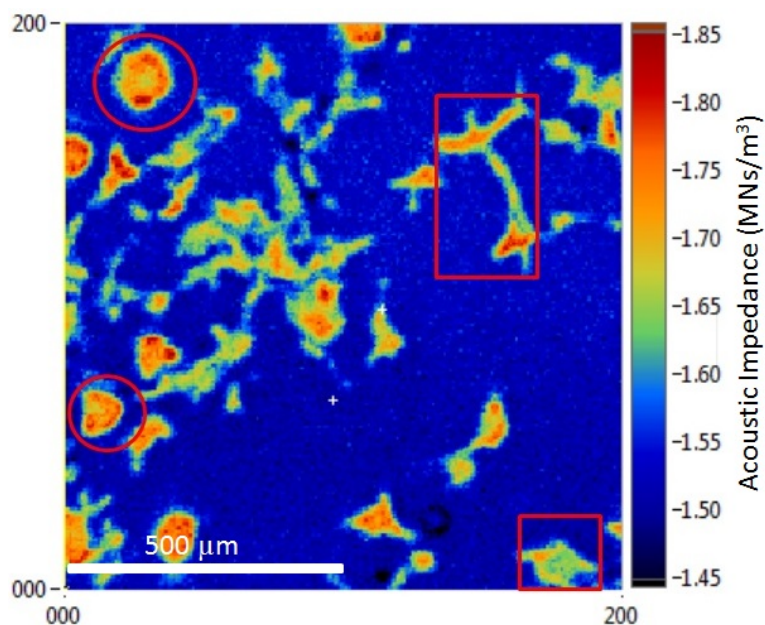
Figure 5.12: Glial cells and gliomas were treated by cytochalasin B. This figure is covered by 200 x 200 pixels.
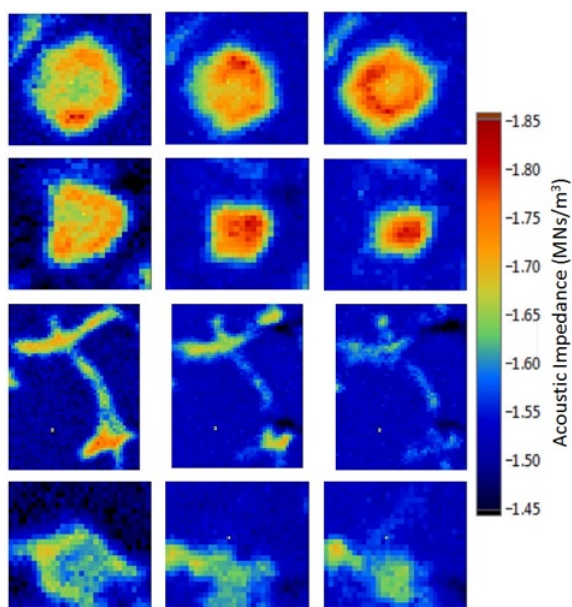

Figure 5.13: Acoustic impedance profile of glial cell and glioma measured at 0, 40 and 90 minutes, from left to right.

there was a significant difference between the acoustic impedances of gliomas before and after being exposed to Cytochalasin-B, whereas no significant difference was observed in the glial cells.
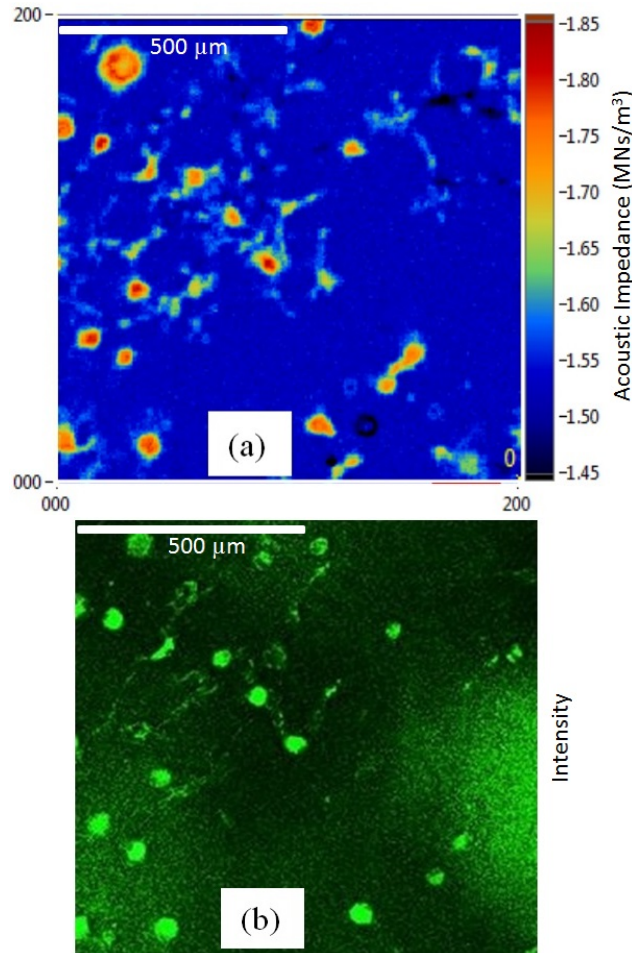
Figure 5.14: Observation result for 90 minutes exposed to cytochalasin B . Acoustical and optical observations are shown in figure a and b respectively.

It is known that cytochalasin disrupts F-actin filaments, which are the one of the main cytoskeleton components [113–115]. As the result of this measurement, it is believed that cytochalasin-B promotes de-polymerization of actin filaments that compose the cytoskeleton of a cell. Therefore, it is reasonable that the acoustic impedance of the corresponding area, which represents its elastic property, diminished after exposure to cytochalasin-B.

Normal and cancerous cells can be distinguished based on their mechanical properties because several measurements have shown that cancerous cells are less stiff than normal cells [86–88]. The lower stiffness of cancerous cells may be caused by fewer actin filaments and microtubules [86]. Because the proportion of cytoskeleton in glioma is much lower than in glial cells, the effect of cytochalasin-B on glioma is expected to

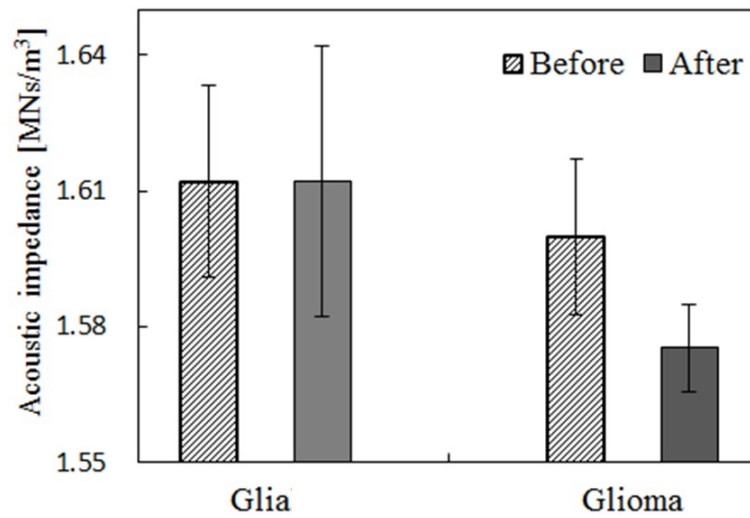Figure 5.15: Bar graph is indicating the average acoustic impedance of glias and gliomas before and after treatment.

be more significant than on glial cell. Nevertheless, it does not seem natural that there was almost no effect of cytochalasin-B on glial cell. It might be that the glial cell in this condition were not active enough to be affected by cytochalasin-B. In addition, there is a tendency that glial cell shrinkage during measurement as shown in Fig. 5.13.

Although further study of the effect of drugs on acoustic impedance is required, this type of quantitative acoustic observation will be useful to assess the condition of biological cells without influencing the cells by the measurement.

5.6 Conclusions

We have proposed a new technique to quantitatively observe cultured cells by means of characteristic acoustic impedance. This technique utilizes a calibration curve to translate acoustic reflection intensity into characteristic acoustic impedance of the biological cell. Practically, the internal structures of the cells were clearly observed through acoustic impedance profiles. The disruption effect of cytochalasin B on actin filaments of glia and glioma is also clearly shown in the experimental results. We believe that this new method is suitable for non-invasive continuous observations of biological cells without introducing contaminants.

For future prospect, we can also utilize this technique to support biological observation. As recently, Japanese researcher, Shinya Yamanaka who got the Nobel for Physiology or Medicine, He found that mature cells can be converted to stem cells [116]. He has been inventing cell replacement therapy using iPS cells.

However, this technique has a potential to introduce cell mutation. For this special case, we may propose our technique to screen healthy cell and remove suspicious or cancerous cell by identifying the acoustic impedance of the corresponding cells. We also realized that several matters such as the creation of new layer, in homogeneous target, cell thickness and reducing vibration of scanning system should be observed further in order to improve our technique.

Chapter 6

Cell's Internal Structure Observation

6.1   Brief Description

This chapter is proposing a new type of observation for the internal structure of biological tissue without introducing contaminants, so-called Cell's Internal Structure Observation. Gliomas were cultured on a thin polystyrene film. The cultured space was subsequently enclosed between two films, with 15 μm in gap distance. A focused ultrasonic beam, its frequency range being 200 - 400 MHz was transmitted from the rear side of the film. Microscopic images were acquired by mechanically scanning the transducer. The acoustic impedance measurement observes the direct reflection from the interface between the plastic substrate and specimen. It reflects acoustic property in the vicinity of the interface between the substrate and specimen. It is highly quantitative but does not perfectly reflect the internal structure. The internal structure measurement observes the reflection from the interface on the surface of the second substrate that is placed with a certain gap. The beam travels twice through the tissue and comes back. Internal structure can clearly be seen with this observation, but quantitative analysis will not be easy because the internal structure through the thickness is not perfectly uniform. In both measurements, observation can be performed without introducing any contaminant to the tissue system.

6.2   Observation and Analysis

In this application, we used the same acoustic microscope system as described in the previous chapter, except target material and measurement methodology.

As shown in Fig. 6.1, acoustic impedance mode can be achieved from the left figure. While the right figure shows the ability of measurement to access the internal structure of target. However, as it was already stated that because transducer, target and coupling medium are integrated into one, this mode has a potential to introduce contaminant.

We need to take the advantages from these two previous studies in order to obtain free contaminant internal structure measurement. A commercially available culture dish (OptiCell, Nunc) was employed. It was composed of two polystyrene films, which has as thin as 80 μm in thickness. The gap between two films was about 2 mm in original but could be adjusted by changing the volume of culture buffer. After several adjustments, the best response was obtained when the gap between two films was 15 μm. Rat glias
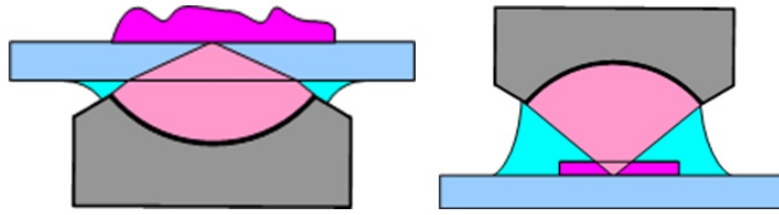
Figure 6.1: The structure of modified reflection and conventional reflection modes of acoustic microscope.

or gliomas sustained by the culture buffer were injected into the gap. This sample then put on the stage for being observed by acoustic microscope as shown in Fig. 6.2. In the real practical work, we did acoustic impedance and internal structure measurement from the bottom side as shown in Fig. 6.3.
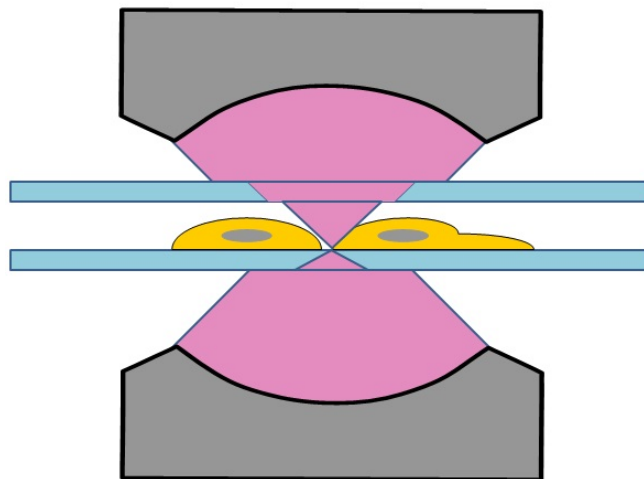

Figure 6.2: Modified acoustic microscope structure for internal structure of cell observation.

The transducer which is composed of a flat ZnO and a sapphire lens was used to transmit ultrasound beam. The beam, being focused on the rear interface between the tissue and substrate, was transmitted and received by the same transducer. Scanning process is done to produce 2D acoustic intensity profile with a view of 400 μm x 400 μm covered by 200 x 200 pixels.

6.2.1   Waveform

As it can be seen in Fig. 6.3, the system has 4 interfaces and generates as much as 4 reflections. The first reflection comes back from the interface between coupling material and substrate. The second comes back from the rear side interface of the first film with the target (interface A). The third is from the front

side interface of the second film with the target (interface B). The last reflection is from the rear interface of the second film with the air. The reflection from the interface A is dependent on the characteristic acoustic impedance of the target. In order to observe the reflection signals from interface-A and interface-B, the reflection from interface-A and interface-B must be separated. Since the gap between two films was far enough (15 μm), overlapping of these two reflections could be avoided. By using appropriate window functions, reflections from interface-A and interface-B can be observed independently.
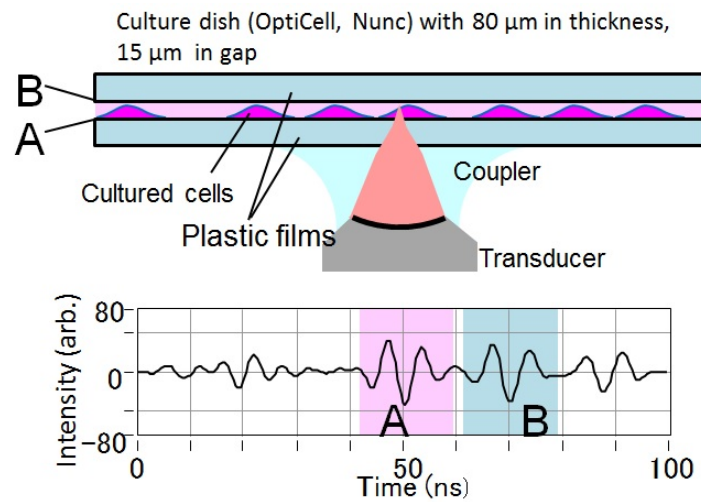

Figure 6.3: Waveforms are generated from interface-A and interface-B. Small time delay between two reflections gives a possibility to observe each waveform independently.

6.2.2   Acoustic Impedance Measurement

In the case of acoustic impedance measurement, reflection A was extracted and then normalized with the reflection from the buffer liquid, which was in the same field of view. Characteristic acoustic impedance of the target in MNs/m^3 was calculated by the procedure described in the previous chapter, which explained the acoustic intensity was converted into acoustic impedance utilizing calibration curve.

6.2.3   Internal Structure Measurement

In the case of internal structure measurement, reflection B was extracted. It is shown in the intensity scale, which is in arbitrary unit. Ultrasonic beam is transmitted from the bottom side through the coupling medium, substrate, target and reflected at the interface between target-upper substrate back to the same transducer. It is supposed that the reflection from interface B is highly influenced by the internal structure of the cell. The measurement result will show the morphological structure of cell, shown by acoustic intensity.
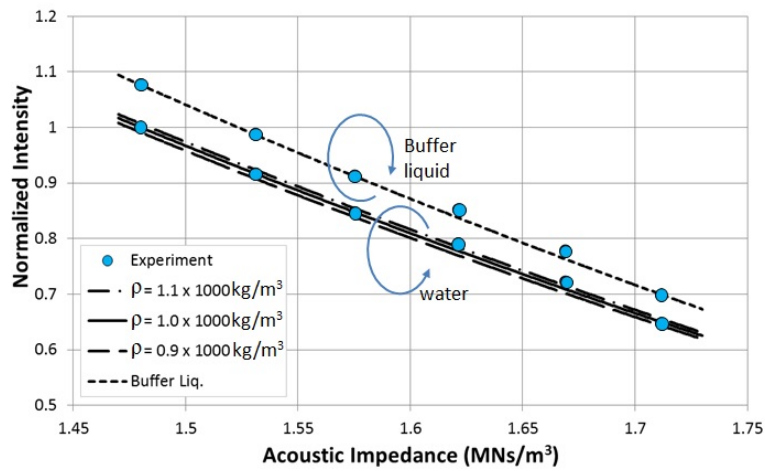
Figure 6.4: Calibration curve to convert acoustic intensity into acoustic impedance. Two types of calibration curves are provided, utilizing water and buffer liquid as a references.

6.3 Results and Discussion

6.3.1 Acoustic Impedance Measurement for Glioma

In the acoustic impedance measurement, ultrasonic beam travels from coupling water into substrate and reflected back at the interface-A. The reflection intensity of the target at the vicinity of an interface-A is then received by the transducer and interpreted into 2D image of acoustic intensity. Figure 6.5 shows the image of acoustic impedance profile obtained by the acoustic impedance measurement. The rings with higher acoustic impedance indicates cytoskeleton. It is assumed that a nucleus is surrounded by cytoskeleton which exhibits high acoustic impedance. However, as it is indicated by the circle, the nucleus is not clearly seen. It is probably due to the fact that the nucleus is sustained by cytoplasm that has lower acoustic impedance.

6.3.2 Internal Structure Measurement for Glioma

Figure 6.6 shows the image of internal structure measurement. The existence of the plastic film in between the coupling medium and target will prevent the target from any contaminant.

The reflection intensity from the interface-B is indicated as a 2D image. The difference of ultrasonic path of internal structure observation compared with the acoustic impedance observation is that the signal makes round trip through the target. Since the target is cell, it is considered as non-homogeneous material. As the focal depth is as less as 10 - 15 μm in this type of transducer, the observation can be performed without significantly losing spatial resolution. The internal structure of the cell, in which ultrasonic beam has penetrated, will give influence (e.g scattering, attenuation) for reflection intensity that is received by the
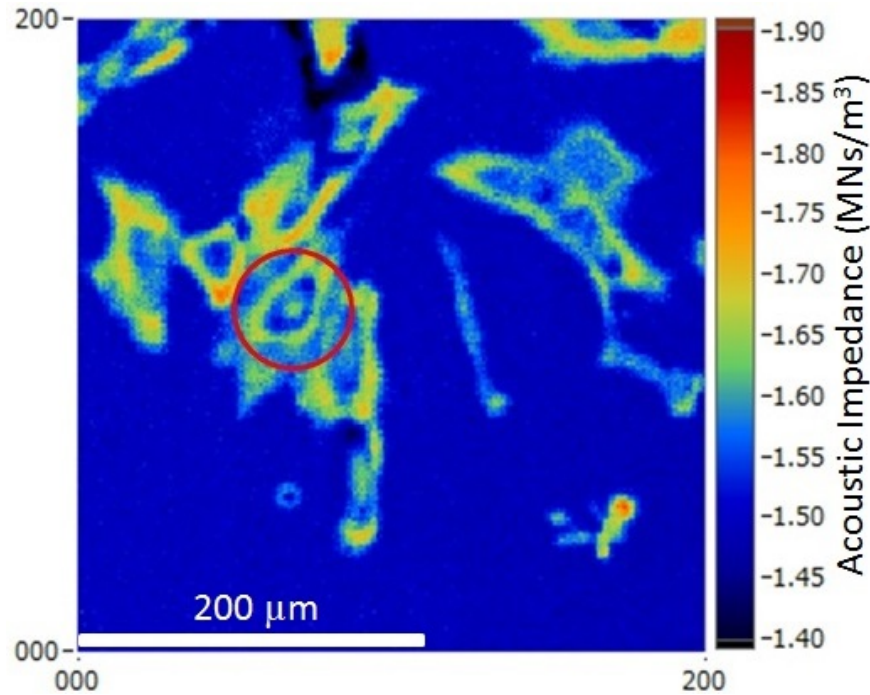
Figure 6.5: Acoustic impedance image of glioma. The image is 400 x 400 μm covered by 200 x 200 pixels.

transducer. This would be the reason why the nucleus of the identical cell is clearly seen inside the circle. Several parameters such as acoustic impedance, attenuation and ultrasonic scattering might contribute to make both nucleus and cytoskeleton to produce lower reflection intensities compared to that either cytoplasm or liquid buffer.

6.3.3 Acoustic Impedance Measurement for Glia

By doing the same procedure, acoustic impedance of Glia was measured as shown in Fig. 6.7. The rings with higher acoustic impedance indicate cytoskeleton. It is assumed that a nucleus is surrounded by cytoskeleton, and exhibits high acoustic impedance. Although cytoskeleton is indicated with high acoustic impedance, its nucleus is not clearly seen. Relatively low acoustic impedance in the central part of the cell would be due to the existence of cytoplasm.

6.3.4 Internal Structure Measurement for Glia

It is considered that the observed image is influenced by the internal structure of the cell, through which the ultrasonic beam has penetrated. This would be the reason why the nucleus of the identical cell is clearly seen in Fig. 6.8. In this figure, both nuclei and cytoskeleton are observed as lower reflection intensities. This

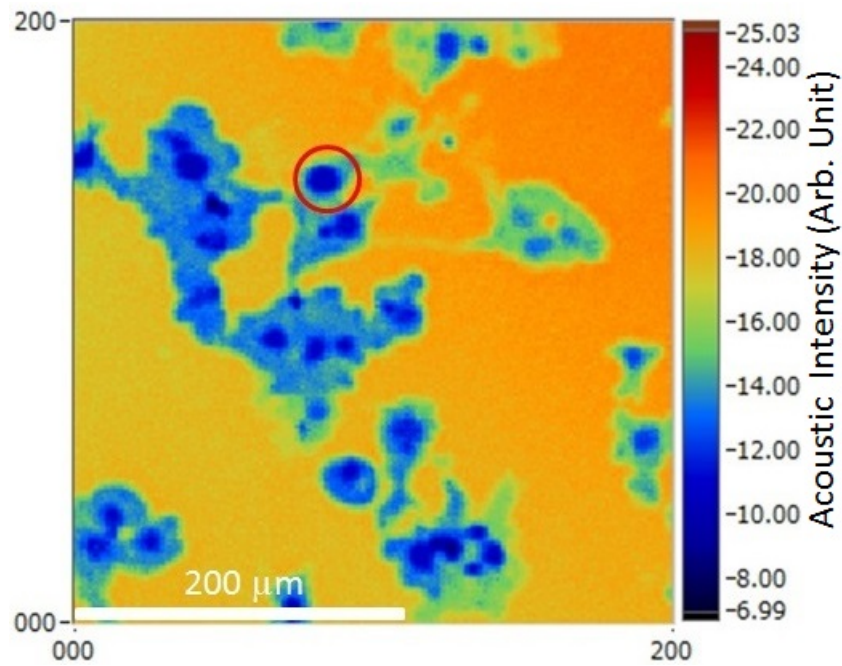Figure 6.6: Reflection acoustic intensity (arb. unit) image of glioma obtained from interface-B. The image is 400 x 400 μm covered by 200 x 200 pixels.
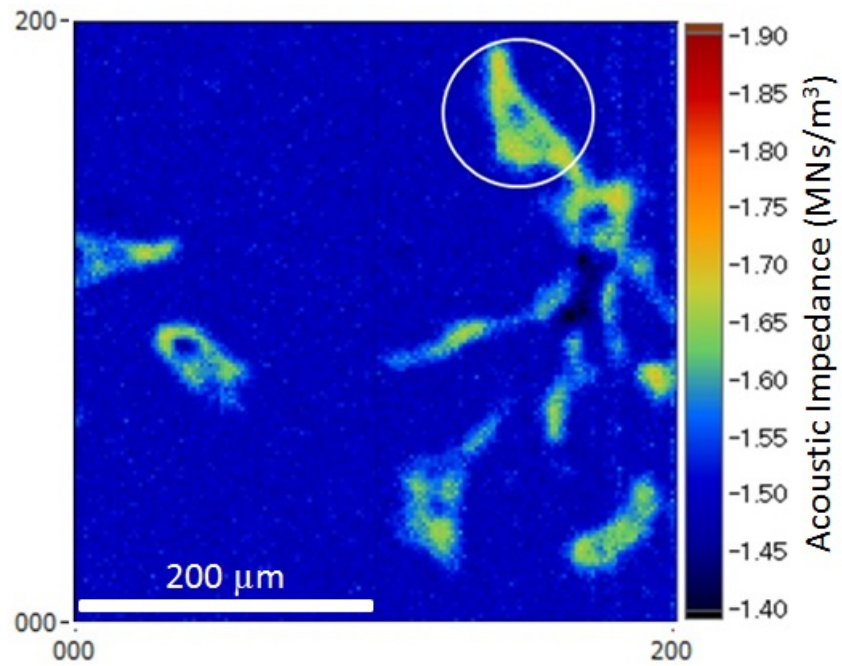

Figure 6.7: Acoustic impedance image of glia. The image was 400 x 400 μm covered by 200 x 200 pixels.

is derived from the higher acoustic impedance, as well as higher attenuation coefficient of the corresponding parts.

However, for quantitative calculation, it is not easy to determine the contribution of each factor, because the cells are located randomly, their size are different and also the internal structure of the cell is supposed to be not uniform. It may need significant approximations. Nevertheless, we think that this observation is useful to observe cell or tissue morphologies with a good contrast.

Furthermore, as the plastic film is existent in between the coupling medium and specimen, the introduction of contaminant would be prevented. For instance, if the specimen is in touch with pure water that is often employed and change its acoustic properties as well as morphologies.
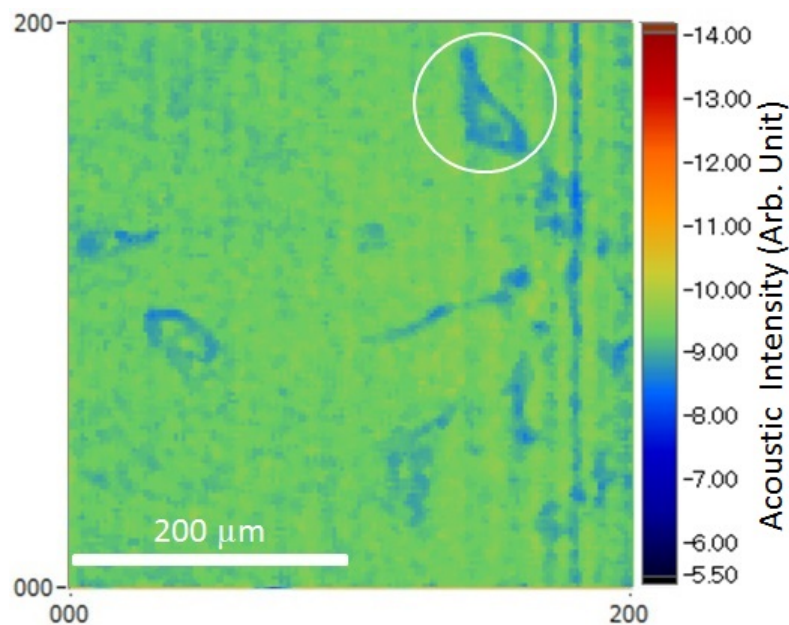
Figure 6.8: Reflection acoustic intensity (arb. unit) image of glia obtained from interface-B. The image is 400 x 400 μm covered by 200 x 200 pixels.

6.3.5   Observation of Hepatoma Tissue

Figure 6.10 shows the image observed with a hepatoma tissue of rat. The tissue was extended onto a slide glass, and covered with a 50 μm-thick PET (polyethylene terephthalate) film. Ultrasonic beam was transmitted through the PET film and focused on the specimen as shown in Fig. 6.9. The reflection from the slide glass was acquired. In order to retain a good focusing, the gap between the slide glass and film was maintained as thin as 15 μm.

Figure 6.9: The structure of the target for measuring hepatoma.

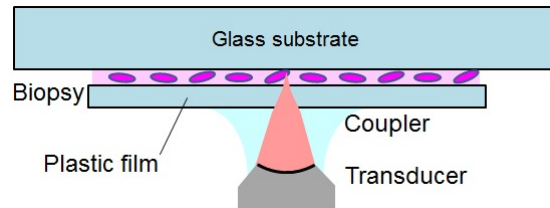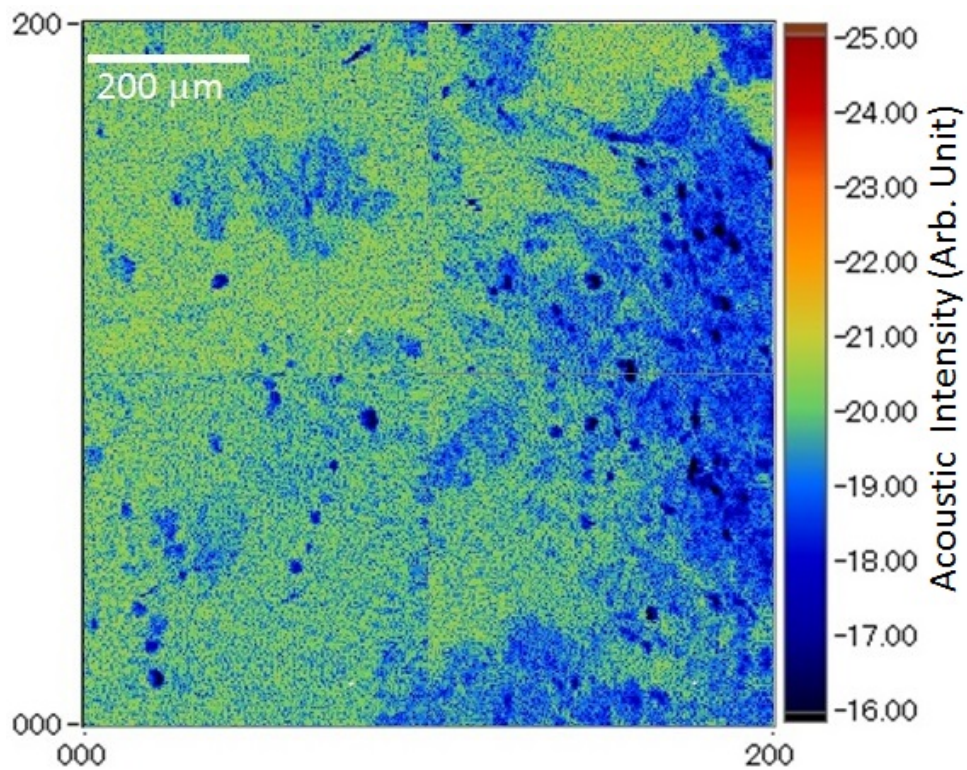Figure 6.10: Reflection image intensity in projection mode of smeared hepatoma, indicated in arbitrary unit. The image is 800 x 800 μm covered by 200 x 200 pixels.

The dark spots, which represent high attenuation, are clearly seen, suggesting the existence of nuclei. As the gap between the films was not totally uniform, quantitative assessment may not be easy to be estimated. Therefore the exact attenuation coefficient may not be easy to be estimated as well. However, it would be enough to see morphology reflected by the cell structure. In addition, as the specimen is placed in between two plastic films after sampling, the specimen is not subjected any contaminants including acoustic coupling medium. Both observations can be performed without introducing any contaminant to the tissue system.

6.4 Conclusion

Two methods, acoustic impedance and internal structure measurements have been applied to measure cell structure using ultrasonic microscope. The advantages of using this microscope are the measurement can be finished quickly and measurement was performed without any contamination. Both acoustic impedance and internal structure measurement, the ultrasonic beam is transmitted from the front side of the plastic film substrate, preventing the specimen from coupling material contamination.

The acoustic impedance measurement observes the direct reflection from the interface-A as it was described in the previous section. The internal structure measurement observes the reflection from the interface-B that is placed with a certain gap. In this measurement, the beam penetrates through the cell and comes back at the surface of the second substrate. The reflection from this surface brings information of internal structure of the cell. Hence, internal structure of cell can clearly be seen. However quantitative analysis will not be easy because non-homogeneous material inside the gap. We found that healthy nucleus is smaller than the cancerous one and small cytoplasm volume relative to nuclei. This method may enhance the result of acoustic impedance measurement concerning to the healthy or cancerous cell observation. In the future, we need to introduce the analysis of acoustic penetration into non-homogeneous material in order to obtain quantitative observation.

Chapter 7

Conclusion, Future Work and Suggestions for Future Application

7.1   Conclusion

The thesis has already described the flow of the content, which is consisting of three achievements. In this chapter, the conclusion is described based on each achievement as follow:

First achievement was described in chapter 4. Acoustic microscope for estimating the acoustic impedance of tissue was proposed. Technique to calculate acoustic impedance and spatial resolution in the previous study has been successfully improved by utilizing Fourier analysis and 22 ^{o} half angle of transducer. The following is the result of tissue observation:

a. We proposed a new type of ultrasonic microscope for biological soft tissues. As the ultrasonic beam is transmitted and received through the substrate (i.e., the target was separated from the coupling medium), a non-invasive observation can be performed without introducing any contamination into the target. In addition, slicing into a thin leaf is not required.

b. The 2-D image of reflection intensity profile obtained by scanning the transducer was interpreted into a quantitative profile of characteristic acoustic impedance. For this purpose, sound field was calculated using Fourier analysis. Because the beam was highly focused onto the target, the ultrasonic beam was decomposed into plane waves with different incident angles, and the reflection depending on the incident angle was considered. Subsequently, a calibration curve was produced and suggested that there was no significant frequency dependence between 30 and 100 MHz. The calibration curve was verified using various contents of saline solution, of which acoustic impedance was known. Based on this result, oblique incident analysis is believed to be more accurate to obtain an acoustic impedance profile.

c. Finally, the cerebellar tissue of a rat was observed to create an acoustic impedance micro profile. As a part of the tissue, Molecular Layer, Granular Layer, Purkinje Layer and White Matter are clearly observed. This technique can skip some processes that are needed by optical microscope, as well as another technique such as PET. It led to a very fast observation. We are very optimistic that such this technique is very useful for quick inspection during the surgery.

101

Second achievement was described in chapter 5. Acoustic microscope for estimating the acoustic impedance of cell was proposed. The structure of sample and transducer were changed. The following is the result of cell observation:

a. A scanning acoustic microscope, using ZnO transducer with a sapphire lens for cell observation was proposed. Its frequency range was spreading from 200 to 400 MHz. A focused acoustic beam driven by a sharp electric pulse was transmitted through the film substrate to the interface between the cell and substrate. By scanning the focal point along the interface, a 2-D image of reflection intensity profile is obtained.

b. As the targets, Glia and Glioma were cultured on the film substrate. The reflection intensity was interpreted into characteristic acoustic impedance by using a calibration curve produced prior to the observation.

c. The calibration curve was created by sound field analysis and verified by using saline solutions of which characteristic acoustic impedances were known.

d. Structure of the cell was clearly observed in the form of acoustic impedance profile. Cytoskeleton was indicated with high acoustic impedance. In addition, the motility of cell could be described clearly.

e. Exposing Glioma to cytochalasin-B resulted in a significant reduction in acoustic impedance, however, its effect to Glia was much less significant.

Third achievement was described in chapter 6. Based on the achievement of chapter 5, the sample was modified. Two targets on the sample were observed and compared. The following is the result of cell observation:

a. Two methods, acoustic impedance and internal structure measurement have been applied to measure cell structure using ultrasonic microscope. Both acoustic impedance and internal structure measurement, the ultrasonic beam is transmitted from the front side of the plastic film substrate, preventing the specimen from any contamination.

b. The acoustic impedance measurement observes the reflection from the interface-A as it was described in the previous section. The internal structure measurement observes the reflection from the interface-B that is placed with a certain gap. In this measurement, the beam penetrates through the cell and comes back at the surface of the second substrate. The reflection from this surface brings information of internal structure of the cell. Hence, internal structure of cell can be clearly seen, however quantitative analysis will not be easy because non-homogeneous material inside the gap.

c. The observation result using internal structure measurement for the nucleus is much clearer than using acoustic impedance measurement.

d. Internal structure measurement can be applied to distinguish the healthy cell from the cancerous one. Healthy nucleus can be found as smaller than the cancerous one and small cytoplasm volume relative to nuclei.

7.2 Future Work

In order to improve the result of these research, there are several points that can be noted for future works. They are:

a. Spatial resolution. The resolution of those systems may be improved by changing transducer and frequency. Increasing the angle of focusing will narrow the distance of focal area, meanwhile, increasing frequency will cause high attenuation. This situation can be compensated by reducing thickness of substrate. However, we must understand that the substrate function as target suspension. If thickness of substrate is too thin, it will generate vibration to the target. Appropriate substrate thickness must be chosen in order to prevent vibration and to fulfill attenuation factor.

b. Observation speed. At this moment, we utilize stepper motor for scanning mechanism. We may improve the speed of scanning mechanism by choosing either voice coil or linear motor.

c. By extending the function of internal structure of cell observation, we can determine density, bulk modulus and shear modulus of specimen (multimode observation).

d. We have successfully investigated the acoustic impedance of glia. In addition, the motility of glia is well described from the measurement. However, we didn't investigate the existence of a new gap on that observation. New layer may exist in between the cell and the substrate. This existence of new buffer liquid may give a significant error in the measurement. We could recognize this situation based on the acoustic impedance value from measurement. By performing new layer evaluation for cell observation we may evaluate the contribution of new layer into measurement.

e. Noise reduction. Noise is always the problem in this measurement. Since the signal in this measurement is very low, noise reduction technique is needed to obtain the maximum SNR ratio and measurement.

7.3 Suggestions for Future Application

We have developed three different structure of acoustic impedance microscope. Those microscopes is used for tissue, cell and internal structure of cell observation as described on chapter 4, 5 and 6. In this observation, comprehensive analysis was done by including all aspect in the system. The result is also verified by measurement and it gives a good agreement. It is proved that this technique is more accurate for

acoustic impedance estimation, as it is shown in the result of measurement. However, this technique does not rule out the possibility for other applications, even though there are several problems and difficulties. And here are several possibilities for future applications.

   a. First structure of reflection mode for tissue observation.

It can be used to investigate the structure and development of brain tissue, distinguish healthy and cancerous tissue based on its acoustic impedance value. However, for stiffer tissue, a problem especially for tissue-substrate adhesion may exist in the system. We need to attentively take care for such kind of this target. For future application, we can use this technique for very short observation to ensure the existence of cancerous tissue before surgery is finished. By small improvement this technique is also applicable for investigating the crack or broken part inside semiconductor components. We also can use this technique to investigate the effect of cosmetic on the skin by observing the elasticity of skin.
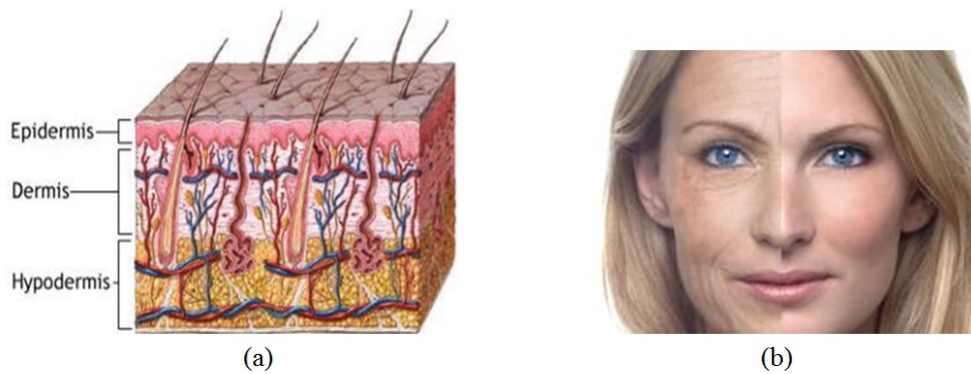

(a)   (b)

Figure 7.1: Skin layers [5] and physical face of young and old women [6].

The human skin consists of three layers. They are epidermis, dermis and hypodermis as shown in Fig. 7.1 left side. Figure 7.1right side shows the physical face of young and old women. Aging process of the skin is affected by renewal rate of epidermis layer and proliferation of cell in dermis layer (consists of collagen and elastin) and ultra violet (UV) exposure, because UV is able to break collagen and elastin down.

Table 7.1 and Fig. 7.2 show the difference between the young and old skin. It can be seen from the morphological of Fig. 7.2 that old skin is less of protein and less stiff compared to that young skin. This difference lead us to have a possibility to measure the elastic of skin. Figure 7.3 (a) shows measurement apparatus based on mechanical measurement. This apparatus are available and easy to be obtained in the market. Rotation torque is used to measure the elastic of the skin. However, we concerned that the result of dermis layer is affected by the other lower layer. Based on that reason, we cooperate with shiseidou (i.e., cosmetic company) and propose a new technique without any influence, especially influence from the other skin layer as shown in Fig. 7.3 (b).

Young	Old
Sheds dead cells every 2 – 4 weeks and is replaced	Slower renewal rate for skin cells
Has ample fatty lipids to hold moisture	Less fatty lipids and is thinner and easily gets dry
Well supported by connective tissues	Less supported due to loss of elasticity
Has adequate oil and sweat glands for moisture and to cool off the skin	Has less oil and sweat glands leaving dry skin
Blemish free due to less UV exposure	Age spots due to UV exposure over time
Firm and smooth	Wrinkled and sagging

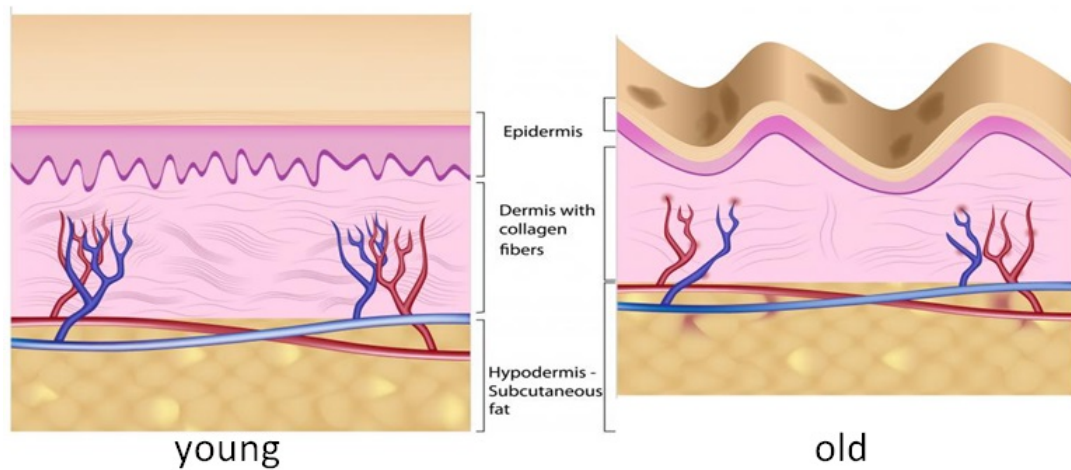Table 7.1: The difference between young and old human skin.

Figure 7.2: The difference between young and old human skin [7].
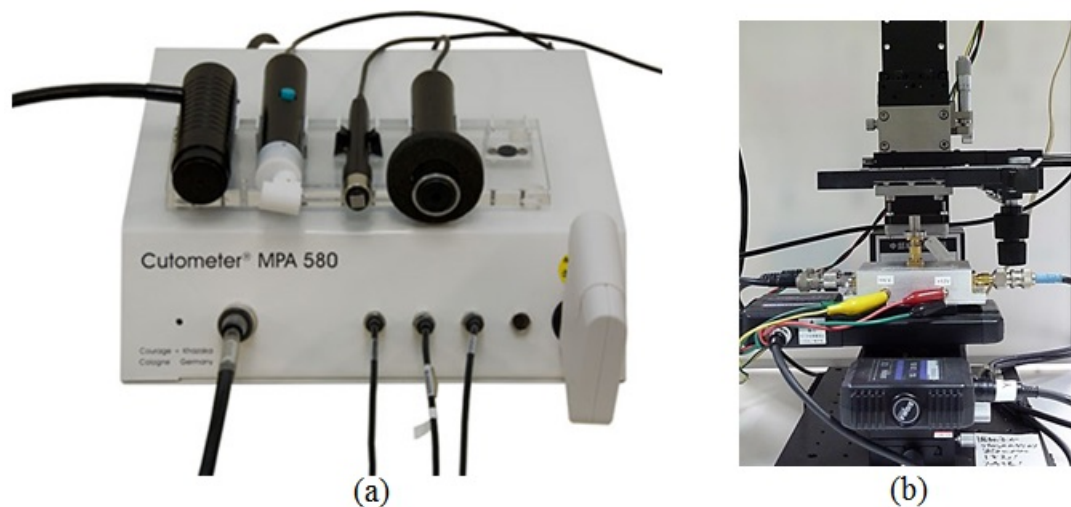

Figure 7.3: (a) Skin torque measurement equipment [8]. (b) Our proposal, acoustic skin measurement.
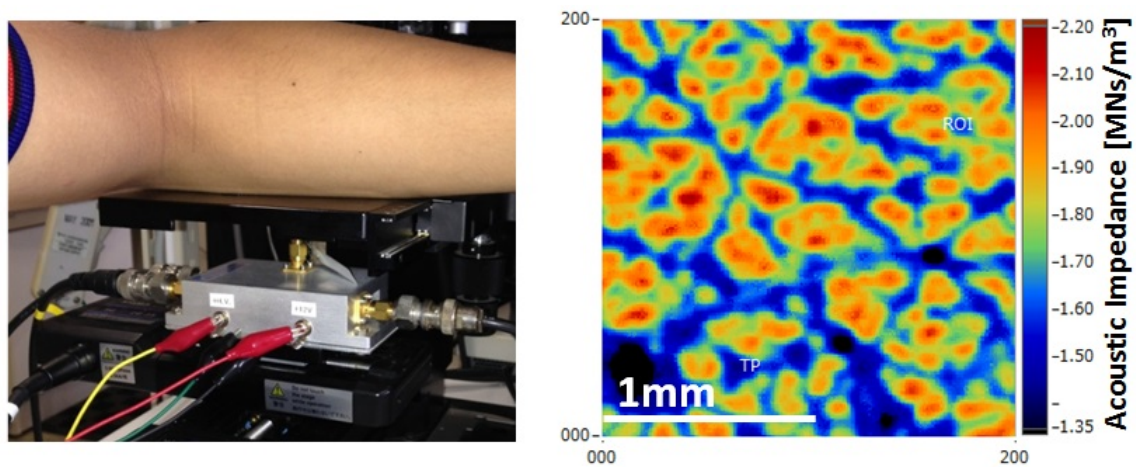
Figure 7.4: Measurement of arm skin in our laboratory and the result shown in acoustic impedance.

Figure 7.4 shows our prototype and preliminary measurement result. We also provided here eight measurement results of arm skin based on gender and age as shown in the Fig. 7.5. From the figure, we believe that the significant different between man and woman were affected by cosmetic. However, further measurement and analysis are needed to confirm this hypothesis.
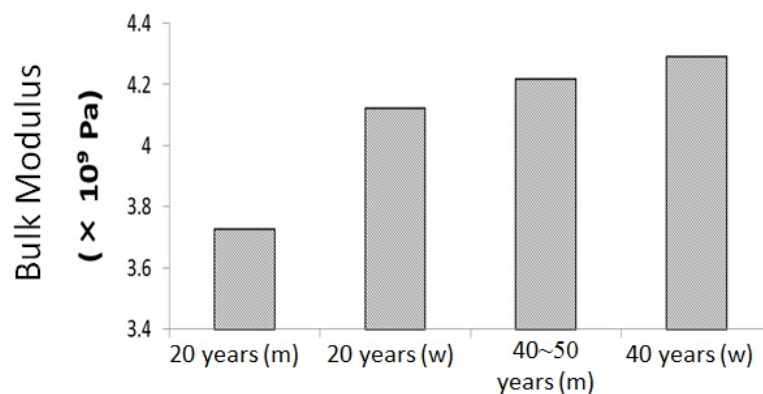

Figure 7.5: (a) Eight preliminary measurement result of arm skin based on gender and age.

b. Second structure of reflection mode for cell observation.

In 2006, Dr. Shinya Yamanaka succeeded to identify a small number of genes within the genome of mice that proved decisive in the reprogramming of mature cells. Nowadays this technology is well known as induced pluripotent stem cells (iPSCs). This technology is very important today, because the stem cell can be programmed and has an ability to function and regenerated to the other organ. Therefore, this technique is able to recover such kind of permanent injury caused by burn or cancer. However, in the process of reprogramming from adult cell into iPSCs, there is a possibility to convert

the cell into cancerous one. Therefore, iPSCs must be reconfirmed and only healthy cell can be implanted to patient. Figure 7.6 shows the illustration of iPSCs therapy. From this stage, our technique is applicable to observe which iPSCs is healthy or cancerous cell.
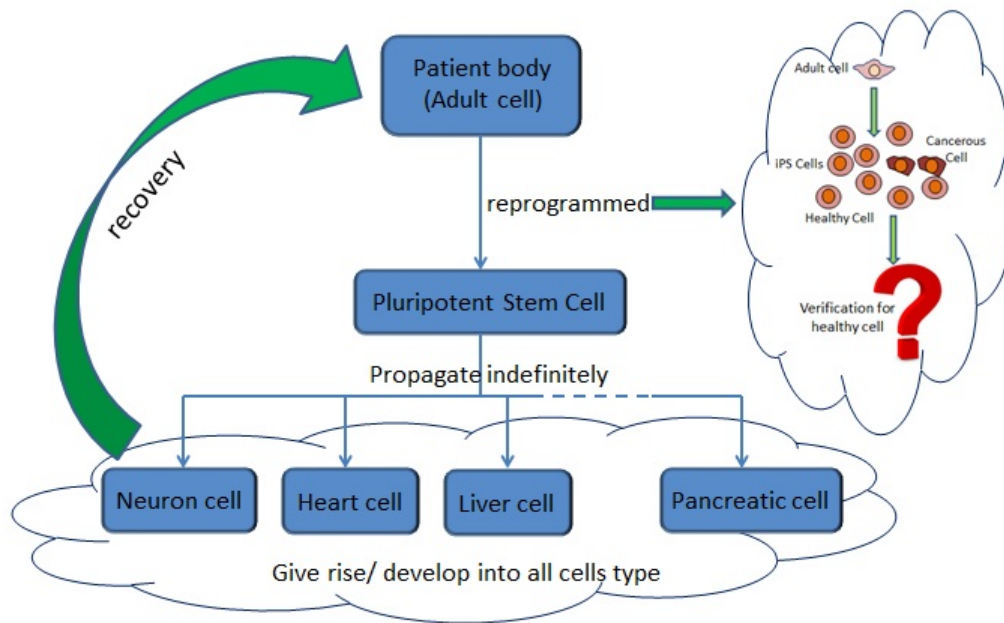

Figure 7.6: The process of generating iPSCs and reprogramming from adult cells into iPSCs.

When the cell is reprogrammed, there is a differentiation (development) process from adult cell into iPSC. Our system is also able for monitoring differentiation of cell. Figure 7.7 shows measurement result of differentiation process from C2C12 Myoblasts.

The acoustic impedance of each cell shown in Fig. 7.7 is calculated, and its average is plotted based on measurement day, as shown in Fig. 7.8. Acoustic impedance is decline from 0 to 6th days. The cytoskeleton of two cells are collapse caused by fusion process. After the 6th day, acoustic impedance is rise up. Two cells are unified. Therefore, polymerization of protein is taken place in order to cure the broken part of cytoskeleton.

c. Internal structure of cell observation.

We have successfully detected the internal structure of cell. Since this measurement is not quantitative yet, it will be a good chance to realize into quantitative measurement. When the acoustic impedance and speed of sound are known, the density of cell can be measured. It will give a chance to measure bulk modulus and elasticity of the cell. For future application, this technique can be used for medical and biological used, as stated above. It is also can be used to evaluated the viscosity of many type of oil and other solutions.
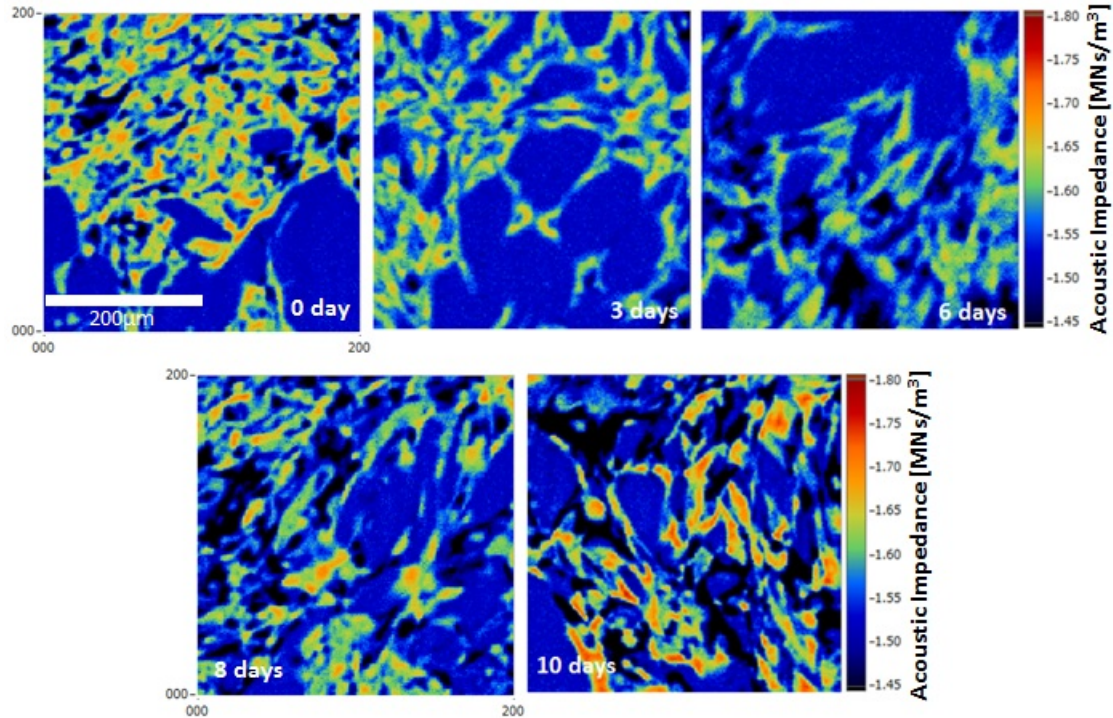
Figure 7.7: The process of tissue development measured at 0, 3, 6, 8 and 10 days. These images are 400 x 400 μm covered by 200 x 200 pixels.
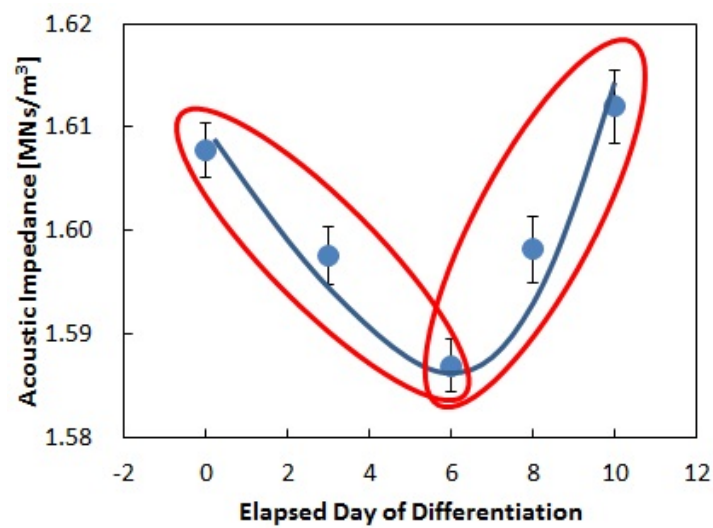

Figure 7.8: The acoustic impedance result based on measurement day.

Appendix A

Appendix. Saline Solution Measurement

Several saline solutions (0 - 10% w) were investigated under acoustic microscope system and shown in 2D image. The left top side are the intensity reflected from pure water. Either right and bottom right side are the intensity reflected from saline solutions. The rest are intensity reflected from air as shown in table A.2. Table A.1 shows the result of measurement based on the content of salt in solution, indicated in intensity and normalized intensity. Figure A.1 shows the plot based on Tabel A.1.

% w	Intensity	Normalization
0	6.742	1
1	6.427	0.953
2	6.093	0.904
4	5.376	0.797
6	4.738	0.703
8	4.104	0.609
10	3.203	0.475

Table A.1: Acoustic intensity measurement results
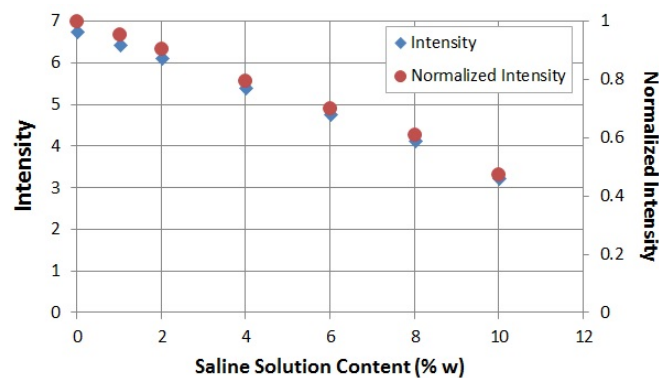

Figure A.1: The plot of saline solution measurement based on its content, shown in intensity and normalized intensity.

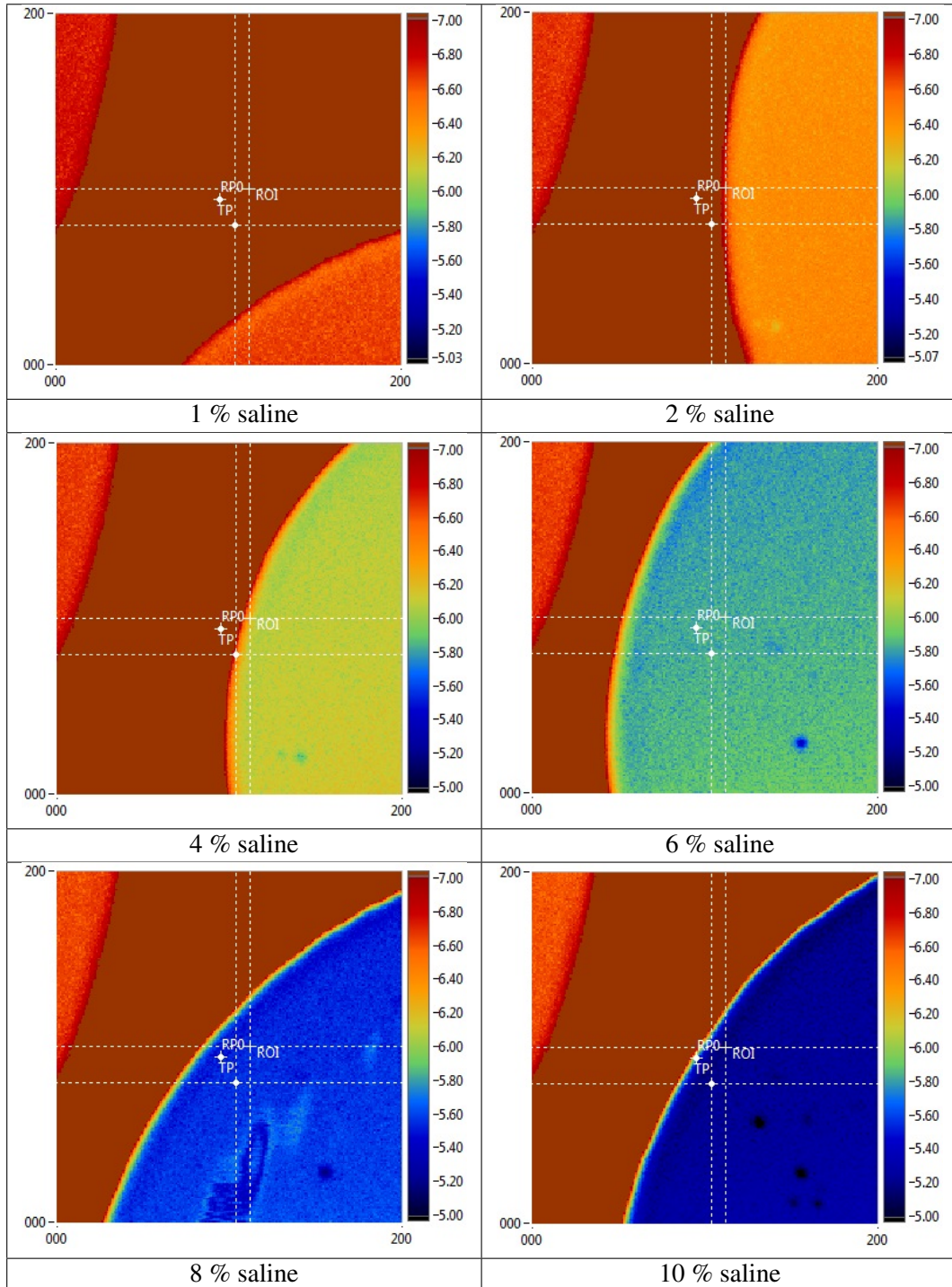|	
1 % saline	2 % saline
4 % saline	6 % saline
8 % saline	10 % saline

Table A.2: Acoustic intensity of several saline solution (% w) were investigated under acoustic microscope.
The left top side: reflection intensity from pure water.
Either right and bottom right side: reflection intensity from saline solutions.
The rest area: reflection intensity from the air.

Appendix B

Appendix. Polystyrene Attenuation

In the system, ultrasound is propagated through sapphire lens, coupling water, substrate and target. In order to obtain attenuation of sound inside polystyrene and sapphire, we utilize the graphs as shown in Fig. B.1 and B.2. Both figure show y-axis as attenuation and x-axis as frequency (MHz).
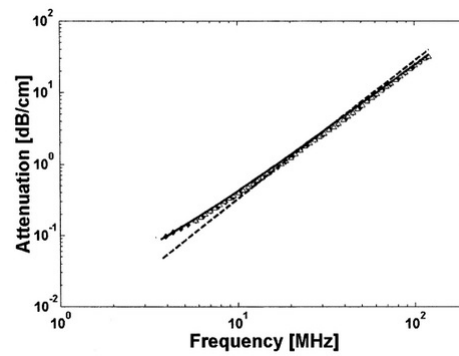

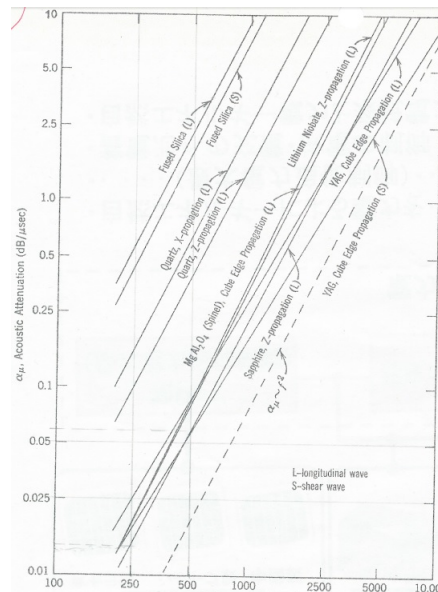Figure B.1: The graph of polystyrene attenuation [9]

Figure B.2: The graph of sapphire attenuation [10].

Bibliography

[1] Ferlay J, Shin HR, Bray F, Forman D, Mathers C, and Parkin DM. Cancer incidence and mortality worldwide: Iarc. Technical report, International Agency for Research on Cancer, Lyon, France, 2010.

[2] *Fundamentals and Applications of Ultrasonic Waves*. CRC Press, 2002.

[3] N. Hozumi, A. Nakano, S. Terauchi, M. Nagao, S. Yoshida, K. Kobayashi, S. Yamamoto, and Y. Saijo. Development of biological acoustic impedance microscope and its error estimation. *Modern Physics Letters B*, 22(11), 2008.

[4] A. I. Gunawan, N. Hozumi, T. Furuhashi, S. Yoshida, Y. Saijo, K. Kobayashi, and S. Yamamoto. Projection mode ultrasonic microscopy for cell-size observation. *UFFC, EFTF and PFM Symposium, IEEE*, 2013.

[5] MD Heather Brannon. Skin anatomy, 2015. URL `http://dermatology.about.com/cs/skinanatomy/a/anatomy.htm`.

[6] M. M. Codilla. Young skin vs. old skin, 2013. URL `http://naturalskincareinfoandtips.blogspot.jp/2013/04/young-skin-vs-old-skin.html`.

[7] Wisegeek.com. What is the dermis?, 2015. URL `http://www.wisegeek.com/what-is-the-dermis.htm#comments`.

[8] EnviroDerm. Cutometer-mpa580, 2015. URL `http://www.enviroderm.co.uk/Cutometer-MPA580`.

[9] L. P. Adjadj, G. Storti, and M. Morbidelli. Ultrasound attenuation in polystyrene latexes. *Langmuir*, 19, 2003.

[10] *Acoustic Fileds and Waves in Solids*. Robert E. Krieger, Pub. Company, 1990.

[11] *Ultrasound for Characterizing Colloids*. Elsevier, 2002.

[12] Y. Saijo, M. Tanaka, H. Okawai, and F. Dunn. The ultrasonic properties of gastric cancer tissues obtained with a scanning acoustic microscope system. *Elsevier, Ultrasound in Med and Biol*, 17(7), 1991.

[13] WHO. Are the number of cancer cases increasing or decreasing in the world?, 2008. URL `http://www.who.int/features/qa/15/en/`.

[14] Cancer Research UK. Cancer tests, 2015. URL `http://www.cancerresearchuk.org/about-cancer/cancers-in-general/tests/`.

[15] N. Hozumi, A. I. Gunawan, S. Kajima, S. Yoshida, Y. Saijo, K. Kobayashi, and S. Yamamoto. Sound field analysis for biological acoustic impedance microscope for its pracise calibration. *UFFC, EFTF and PFM Symposium, IEEE*, 2013.

[16] Wikipedia. Paul langevin, 2014. URL `http://en.wikipedia.org/wiki/Paul_Langevin`.

[17] History of sound. URL `http://electricalfacts.com/Neca/Science/sound/history.shtml`.

[18] Pohlman R., Richter R., and Parow E. Uber die ausbreitung und absorption des ultraschall im menschlichen gewebe und seine therapeutische wirkung an ischias und plexusneuralgie. *Dtsch med. Wochenschr*, 65, 1939.

[19] Gohr H. and Wedekind T. Der ultraschall in der medizin. *Wien Klin Wochenschr*, 19, 1940.

[20] Dussik K. T. Uber die moglichkeit hochfrequente mechanische schwingungen als diagnostisches hilfsmittel zu verwerten. *Z Neurol Psychiat*, 174, 1942.

[21] Dussik K. T. Ultraschall diagnostik, in besondere bei gehirnerkrankungen, mittels hyperphongraphie. *Z Phys Med*, 1, 1948.

[22] Firestone F.A. Flaw detecting device and measuring instrument, 1942.

[23] Firestone F.A. The supersonic reflectoscope for interior inspection. *Metal Progress*, 48, 1945.

[24] Firestone F.A. The supersonic reflectoscope, an instrument of inspecting the interior of solid parts by means of sound waves. *J Acoust Soc Am*, 17, 1946.

[25] Firestone F.A. and Frederick J.R. Refinements in supersonic reflectoscopy. polarized sound. *J Acoust Soc Am*, 18, 1946.

[26] Ludwig G. D. and Struhthers F. W. Considerations underlying the use of ultrasound to detect gallstones and foregn bodies in tissue. Technical report, Naval Medical Research Institute, 1949.

[27] Howry D. H. The ultrasonic visualization of soft tissue structures and disease processes. *J Lab Clin Med*, 40, 1952.

[28] Howry D. H. and Bliss W. R. Ultrasonic visualization of soft tissue structures of the body. *J Lab Clin Med*, 40, 1952.

[29] Wild J. J. and Reid J. M. Application of echo-ranging techniques to the determination of structure of biological tissues. *Science*, 115, 1952.

[30] Leksell L. Echo-encephalography: detection of intracranial complications following head injury. *Acta Chir Scand*, 110, 1955.

[31] Mundt G.H. and Hughes W.F. Ultrasonics in ocular diagnosis. *Am J Ophthalmol*, 41(3), 1956.

[32] Baum G. and Greenwood I. The application of ultrasonic locating techniques to ophthalmology. *Arch Ophthalmol*, 60(2), 1958.

[33] Baum G. and Greenwood I. The application of ultrasonic locating techniques to ophthalmology: theoretical considerations and acoustic properties of ocular media. *Arch Ophthalmol*, 46, 1958.

[34] M. von Ardenne and M. Millner. The u.s. focoscan method. *IRE Trans Biomed Electron*, 9, 1962.

[35] K. U. Schentke and F. Renger. Uber die diagnostische verwertbarkeit des ultraschallhepatograms. *Z. Ges Inn Med*, 21, 1964.

[36] F. L. Thurstone, N. I. Kjosnes, and W. M. McKinney. Ultrasonic scanning of biologic tissue by a new technique. *Science*, 149, 1965.

[37] Olympus. Introduction flaw detection, 2015. URL `http://www.olympus-ims.com/en/applications-and-solutions/introductory-ultrasonics/introduction-flaw-detection/`.

[38] R. Jones and I. Facaoaru. Recommendations for testing concrete by the ultrasonic pulse method. *Materiaux et Construction, JUILLET–AOUT*, 2(4), 1969.

[39] H. Irie, Y. Yoshida, Y. Sakurada, and T. Ito. Non-destructive-testing methods for concrete structures. *NTT Technical Review Letter*, 6(5), 2008.

[40] F. Chemat, Z. Huma, and M. K. Khan. Applications of ultrasound in food technology: Processing, preservation and extraction. *Ultrasonics Sonochemistry*, 18(4), 2011.

[41] *Acoustic Microscopy Fundamental and Application*. Wiley-VCH Verlag GmbH and Co. KGaA, 2008.

[42] R. A. Lemons and C. F. Quate. Acoustic microscope scanning version. *Appl. Phys. Lett.*, 24, 1974.

[43] J. Bereiter-Hahn, C. H. Fox, and B. Thorell. Quantitative reflection contrast microscopy of living cells. *J. Cell Biol.*, 82(3), 1979.

[44] N. Chubachi, T. Sannomiya, J. Kushibiki, K. Horii, H. Maehara, and H. Okazaki. Scanning acoustic microscope with transducer swing along beam axis. *Proc. IEEE Ultrasonic Symp*, 1982.

[45] J. A. Hildebrand, D. Rugar, R. N. Johnston, and C. F. Quate. Acoustic microscopy of living cells. *Proc. Natl. Acad. Sci. USA*, 78(3), 1981.

[46] J. Ophir and T. Lin. A calibration-free method for measurement of sound speed in biological tissue samples. *IEEE. Transc. UFFC*, 35(5), 1988.

[47] Y. Saijo, M. Tanaka, H. Okawai, H. Sasaki, S. Nitta, and F. Dunn. Ultrasonic tissue characterization of infarcted myocardium by scanning acoustic microscopy. *Elsevier, Ultrasound in Med and Biol*, 23 (1), 1997.

[48] Y. Saijo, A. Tanaka, H. Sasaki, T. Iwamoto, E. S. Filho, M. Yoshizawa, and T. Yambe. Basic ultrasonic characteristics of atherosclerosis measured by intravascular ultrasound and acoustic microscopy. *Elsevier, International Congress Series 1274*, 2004.

[49] R. M. Lemor, E. C. Weiss, G. Pilarczyk, and P. V. Zinin. Mechanical properties of single cells; measurement possibilities using time resolved scanning acoustic microscope. *Ultrasonic Symposium*, 2004.

[50] Y. Saijo, N. Hozumi, K. Kobayashi, N. Okada, C.K Lee, H. Sasaki, T. Yambe, and M. Tanaka. Development of ultrasonic nano-imaging system for visualization of cells. *World Congress on Medical Physics and Biomedical Engineering, IFMB Proceeding*, 14, 2007.

[51] Y. Saijo, E. S. Filho, H Sasaki, T. Yambe, M. Tanaka, N. Hozumi, K. Kobayashi, and N. Okada. Ultrasonic tissue characterization of atherosclerosis by a speed-of-sound microscanning system. *UFFC-IEEE*, 54(8), 2007.

[52] Y. Hagiwara, Y. Saijo, A. Ando, E Chimoto, H. Suda, Y Onoda, and E Itoi. Ultrasonic intensity microscopy for imaging of living cells. *Elsevier, Ultrasonic Journal*, 49, 2009.

[53] E. Maeva, F. Severin, C. Miyasaka, B.R. Tittmann, and R.G. Maev. Acoustic imaging of thick biological tissue. *IEEE Transc. on UFFC*, 56(7), 2009.

[54] E. M. Strohm, G. J. Czarnota, and M. C. Kolios. Quantitative measurements of apoptotic cell properties using acoustic microscopy. *IEEE Transc. on UFFC*, 57, 2010.

[55] N. Hozumi, R. Yamashita, C. K. Lee, M. Nagao, K. Kobayashi, Y. Saijo, M. Tanaka, and S. Ohtsuki. Time frequency analysis for pulsen driven ultrasonic microscopy for biological tissue characterization. *Elsevier, Ultrasonics*, 42, 2004.

[56] N. Hozumi, A. Kimura, S. Terauchi, M. Nagao, S. Yoshida, K. Kobayashi, and Y. Saijo. Acoustic impedance micro-imaging for biological tissue using a focused acoustic pulse with a frequency range up to 100 mhz. *IEEE, Ultrasonic Symposium*, 2005.

[57] A. Kimura, S. Terauchi, M. Nagao, S. Yoshida, K. Kobayashi, Y. Saijo, and N. Hozumi. Development of cerebella tissue of rat characterized by acoustic impedance microscope. *IEEE, Ultrasonic Symposium*, 2006.

[58] Y. Saijo, N. Hozumi, K. Kobayashi, N. Okada, T. Ishiguro, Y. Hagiwara, E. S. Filho, and T. Yambe. Ultrasound speed and impedance microscopy for in vivo imaging. *IEEE EMBS*, 2007.

[59] *Acoustic Wave, Device, Imaging and Analog Signal Processing*. Prentice-Hall, 1987.

[60] Wikipedia. Acoustic impedance, 2015. URL `http://en.wikipedia.org/wiki/Acoustic_impedance`.

[61] *Basic of Biomedical Ultrasound for Engineers*. A John Wiley and Sons, Inc., 2010.

[62] *Fluid Mechanics*. Pergamon Press, 1987.

[63] *Physical Properties of Polymers Handbook*. Springer, 2007.

[64] L. P. Adjadj, A. K. Hipp, G. Storti, and M. Morbidelli. Characterization of dispersions by ultrasound spectroscopy. *IUSD*, 5, 2006.

[65] Q. Zhou, S. Lau, D. Wu, and K. K. Shung. Piezoelectric films for high frequency ultrasonic transducers in biomedical applications. *Progress in Material Science*, 56, 2011.

[66] *HD80 Manual Book*, .

[67] *UPF-5A Manual Book*, .

[68] Solution for cell culture growth and analysis.

[69] F. Peters and F. Petit. A broad band spectroscopy method for ultrasound wave velocity and attenuation measurement in dispersive media. *Ultrasonics*, 41, 2003.

[70] Kaye and Laby. National physical laboratory (npl), 2015. URL `http://www.kayelaby.npl.co.uk/chemistry/3_11/3_11_1.html`.

[71] *Physical Properties of Polymers Handbook*. Springer, 2007.

[72] Onda Corporation. Acoustic properties of plastics, 2002. URL `http://www.ondacorp.com/images/Plastics.pdf`.

[73] K. Kobayashi, S. Yoshida, Y. Saijo, and N. Hozumi. Acoustic impedance microscopy for biological tissue characterization. *Elsevier, Ultrasonic Journal*, 54, 2014.

[74] NPL UK. Technical guides speed of sound in sea water, 2015. URL `http://resource.npl.co.uk/acoustics/techguides/soundseawater/content.html#UNESCO`.

[75] S. Ueba, M. Matsukawa, and T. Otani. Ultrasonic wave propagation in particle compounded gels. *Jpn. J. Appl. Phys.*, 38, 1999.

[76] Y. Yamada, S. Maeda, T. Tsuchiya, and N. Endoh. Analysis of sound field of aerial ultrasonic sensor by three-dimensional finite-difference time-domain methode using parallel computing. *Jpn. J. Appl. Phys.*, 43(5B), 2004.

[77] T. Aoyagi, M. Nakazawa, K. Nakamura, and S. Ueha. Numerical analysis of ultrasonic beam of variable-line-focus-beam film transducer. *Jpn. J. Appl. Phys.*, 46(7B), 2007.

[78] D. Belgroune, J. F. de Belleval, and H. Djelouah. Modelling of the ultrasonic field by the angular spectrum method in presence of interface. *Elsevier, Ultrasonic Journal*, 40, 2002.

[79] D. Belgroune, J. F. de Belleval, and H. Djelouah. A theoritical study of ultrasonic wave transmission through a fluid-solid interface. *Elsevier, Ultrasonic Journal*, 48, 2008.

[80] Y. Du and J. A. Jensen. Fast simulation of non-linear pulsed ultrasound fields using an angular spectrum approach. *Elsevier, Ultrasonic Journal*, 53, 2013.

[81] Y. Du, H. Jensen, and J. A. Jensen. Investigation of an angular spectrum approach for pulsed ultrasound fields. *Elsevier, Ultrasonic Journal*, 53, 2013.

[82] S. Saito. Finite amplitude method for measuring the nonlinearity parameter b/a in small-volume samples using focused ultrasound. *J. Acoustic Soc. Am.*, 127(1), 2010.

[83] *Acoustic Microscopy and High Resolution Imaging*. Wiley-VCH Verlag GmbH and Co. KGaA, 2013.

[84] Molbiol. Density of salt solution, 2015. URL `http://molbiol.ru/eng/protocol/01_22.html`.

[85] A. M. G. Borgers, L. O. Benetoli, M. A. Licinio, V. C. Zoldan, M. C. Santos-Silva, J. Assreuy, A. A. Pasa, N. A. Debacher, and V. Soldi. Polymer films with surfaces unmodified and modified by non-thermal plasma as new substrates for cell adhesion. *Elsevier, Material Science and Engineering C*, 33(3), 2013.

[86] M. Lekka ans P. Laidler, D. Gil, J. LEkki, Z. Stachura, and A. Z. Hrynkiewicz. Elasticity of normal and cancerous human bladder cells studied by scanning force microscopy. *Eur Biophys J.*, 28, 1999.

[87] S. E. Cross, Y. S. Jin, J. Rao, and J. K. Gimzewski. Nanomechanical analysis of cells from cancer patients. *Nat. Nanotechnol*, 2, 2007.

[88] O. Jonas, C. T. Mierke, and Josef A. Ks. Invasive cancer cell lines exhibit biomechanical properties that are distinct from their noninvasive counterparts. *Soft Matter*, 7, 2011.

[89] T. Kundu, J. Bereiter-Hahn, and K. Hillmann. Measuring elastis properties of cells by evaluation of scanning acoustic microscopy v(z) values using simplex algorithm. *Biophyiscal Journal*, 59, 1991.

[90] E.C. Weiss, P. Anastasiadis, G. Pilarczyk, R.M. Lemor, and P.V. Zinin. Mechanical properties of single cells by high frequency time resolved acoustic microscopy. *IEEE Transc. On UFFC*, 54(11), 2007.

[91] E.M. Strohm and M C. Kolios. Measuring the mechanical properties of cells using acoustic microscopy. *IEEE – EMBS*, 2009.

[92] E.M. Strohm and M C. Kolios. Quantifying the ultrasonic properties of cells during apoptosis using time resolved acoustic microscopy. *IEEE – International Ultrasonics Symposium*, 2009.

[93] J. Litniewski and J. Bereiter-Hahn. Measurements of cells in culture by scanning acoustic microscopy. *J. Microsc.*, 158, 1990.

[94] M. von Buttlar, E.A. Mohamed, and W. Grill. Signal processing for time-lapse cell imaging with vector-contrast scanning acoustic microscopy. *Acoustical Imaging*, 30, 2011.

[95] B. Zhang, Q. Cheng, M. Chen, W. Yao, M. Qian, and B. Hu. Imaging and analyzing the elasticity of vascular smooth muscel cells by atomic force acoustic microscope. *Ultrasound in Medicine and Biology*, 38(8), 2012.

[96] A.I. Gunawan, N. Hozumi, S. Yoshida, Y. Saijo, K. Kobayashi, and S. Yamamoto. Numerical analysis of ultrasound propagation and reflection intensity for biological acoustic impedance microscope. *Ultrasonics*, In Press, 2015.

[97] A. Nakano, T. Uemura, N. Hozumi, M. Nagao, S. Yoshida, K. Kobayashi, S. Yamamoto, and Y. Saijo. Non-contact observation of cultured cells by acoustic impedance microscope. *IEEE-Ultrasonics Symposium*, 2008.

[98] H. Asou, S. Hirano, and E. G. Brunngraber. Preparation of astrocyte-deficient cultures containing neurons and oligodendroglia from embryonic rat cerebral hemispheres. *Neurosci Res.*, 3(4), 1986.

[99] K. Raum, K.V. Jenderka, A. Klemenz, and J. Brandt. Multilayer analysis: Quantitative scanning acoustic microscopy for tissue characterization at a microscopic scale. *IEEE Transc. On UFFC*, 50, 2003.

[100] S. Brand, E.C. Weiss, R.M. Lemor, and M.C. Kolios. High frequency ultrasound tissue characterization and acoustic microscopy of intracellular changes. *Ultrasound in Medicine and Biology*, 34, 2008.

[101] B.R. Tittmann, C. Miyasaka, A.M. Mastro, and R.R. Mercer. Study of cellular adhesion with scanning acoustic microscopy. *IEEE Transc. On UFFC*, 54, 2007.

[102] A.S.G. Curtis. The mechanism of adhesion of cells to glass, a study by interference reflection microscopy. *The Journal of Cell Biology*, 20, 1964.

[103] C.S. Izzard and L. R. Lochner. Cell to substrate contacts in living fibroblasts: An interference reflection study with an evaluation of the technique. *Journal of Cell Science*, 21, 1976.

[104] K.F. Giebel, C. Bechinger, H. Herminghaus, M. Riedel, P. Leiderer, U. Weiland, and M. Bastmeyer. Imaging of cell/substrate contants of living cells with surface plasmon resonance microscopy. *Biophysical Journal*, 76, 1999.

[105] T. Kundu, J. Bereiter-Hahn, and I. Karl. Cell property determination from the acoustic microscope generated voltage versus frequency curves. *Biophysical Journal*, 78, 2000.

[106] K. Luby-Phelps. Cytoarchitecture and physical properties of cytoplasm: volume, viscosity, diffusion, intracellular surface area. *International Review of Cytology*, 192, 2000.

[107] A.S. Verkman. Solute and macromolecule diffusion in cellular aqueous compartments. *Trends Biochem. Sci.*, 27(1), 2002.

[108] T.J. Mitchison and L.P. Cramer. Actin-based cell motility and cell locomotion. *Cell*, 84(3), 1996.

[109] D.A. Lauffenburger and A.F. Horwitz. Cell migration: a physically integrated molecular process. *Cell*, 84(3), 1996.

[110] M. Raftopoulou and A. Hall. Cell migration: Rho gtpases lead the way. *Dev. Biol.*, 265(1), 2004.

[111] D.C. Lovelady, J. Friedman, S. Patel, D.A. Rabson, and C.M. Lo. Detecting effects of low levels of cytochalasin b in 3t3 fibroblast cultures by analysis of electrical noise obtained from cellular micromotion. *Biosensors and Bioelectronics*, 24, 2009.

[112] N. Banville, J. Fallon, K. McLoughlin, and K. Kavanagh. Disruption of haemocyte function by exposure to cytochalasin-b or nocodazole increases the susceptibility of galleria mellonella larvae to infection. *Microbes and Infection*, 13, 2011.

[113] J.A. Cooper. Effects of cytochalasin and phalloidin on actin. *The journal of Cell Biology*, 105, 1987.

[114] E. Urbanik and R.R. Ware. Actin filament capping and cleaving activity of cytochalasins b, d, e, and h. *Arch Biochem Biophys.*, 269(1), 1989.

[115] M.A. Tsai, R.S. Frank, and R.E. Waugh. Passive mechanical behavior of human neutrophils: effect of cytochalasin b. *Biophysical Journal*, 66, 1994.

[116] nobelprize. Press release, 2012. URL `http://www.nobelprize.org/nobel_prizes/medicine/laureates/2012/press.html`.

Acknowledgments

- My deepest thanks and appreciation go to my wife, Anita Oktavia and my son, Mohammad Pujangga Gunawan for their support, understanding, patience and encouragement for completion of this program.

- The last but not least, Mom and Dad, I thank you.

 I wish God will guide and bless you all.

List of Publications

Journals

[1]   A. I. Gunawan, N. Hozumi, S. Yoshida, Y. Saijo, K. Kobayashi and S. Yamamoto. "Numerical Analysis of Ultrasound Propagation and Reflection Intensity for Biological Acoustic Impedance Microscope". Elsevier, Ultrasonics Journal,vol. 61, pp. 79-87, April 2015.

[2]   A. I. Gunawan, N. Hozumi, K. Takahashi, S. Yoshida, Y. Saijo, K. Kobayashi and S. Yamamoto. "Numerical Analysis of Acoustic Impedance Microscope Utilizing Acoustic Lens Transducer to Examine Cultured Cells ". Elsevier, Ultrasonics Journal,vol. 63, pp. 102-110, June 2015.

Conferences

[1]   K. K. Isa, S. Kajima, A. I. Gunawan, A. A. Manaf and N. Hozumi. "A Mockup of Ultrasonic Transmission Microscope for Medical and Biological Use". IEE Japan, p. 141, Nagoya Japan, 20th - 22nd March 2013.

[2]   S. Kajima, A. I. Gunawan, S. Yoshida, N. Hozumi and K. Kobayashi. "Sound Field Analysis for Biological Acoustic Impedance Microscope". IEE Japan, p. 143, Nagoya Japan, 20th - 22nd March 2013.

[3]   N. Hozumi, A. I. Gunawan, S. Kajima, S. Yoshida, Y. Saijo, K. Kobayashi and S. Yamamoto. "Sound Filed Analysis for Biological Acoustic Impedance Microscope for Its Precise Calibration". Joint UFFC, EFTF and PFM Symposium IEEE, pp. 1212-1215, Prague, Czech Republic, 21st – 25th July 2013.

[4]   A. I. Gunawan, N. Hozumi, T. Furuhashi, S. Yoshida, Y. Saijo, K. Kobayashi and S. Yamamoto. "Projection Mode Ultrasonic Microscopy for Cell-size Observation". Joint UFFC, EFTF and PFM Symposium IEEE, pp. 884-887, Prague, Czech Republic, 21st – 25th July 2013.

[5]   S. Kajima, A. I. Gunawan, Y. Nakamura, S. Yoshida and N. Hozumi. "Viscoelastic Imaging Using Acoustic Impedance Microscope and Its Application for Liver Cancer Detection". IEE Japan, p. 135, Ehime Japan, 18th – 20th March 2014.

[6]   K. Takahashi, H. Hamada, M. Betsudan, A. I. Gunawan, K. Kobayashi, S. Yamamoto, S. Yoshida and N. Hozumi. "Quantitative Observation of Cultured Glia and Gioma Using High-Resolution Acoustic Impedance Microscope". 6th Special Conference of The International Society for Neuro-Chemistry, p. 28, Tokyo Japan, 20th – 22nd September 2014.

[7]   A. I. Gunawan, K. Takahashi, N. Hozumi and S. Yoshida. "Projection Mode Acoustic Microscopy for Biological Cell Observation". International Conference of Global Network for Innovative Technology (IGNITE 2014), pp. 107-111, Penang Malaysia, 14th – 16th December 2014.

[8]   K. Takahasi, A. I. Gunawan, H. Yamada, S. Yoshida, N. Hozumi and K. Kobayashi. "Quantitative Evaluation of Cell by Using High Resolution Acoustic Impedance Microscope". IEE Japan, Tokyo Japan, 24th - 26th March 2015.